MAGNETOINDUCTIVE WAVES IN METAMATERIAL-BASED STRUCTURES

JIARUO YAN

WADHAM COLLEGE



A thesis submitted for the degree of Doctor of Philosophy

University of Oxford

Department of Engineering Science

Abstract

Magnetoinductive Waves in Metamaterial-Based Structures

Metamaterials are artificial structures that exhibit unusual properties not seen in natural materials achieved by designing the composite unit cells on the subwavelength scale. Magnetic metamaterials consist of magnetically coupled resonators. Strong magnetic interactions between the unit cells in magnetic metamaterials give rise to magnetoinductive (MI) waves, which are slow waves with wavelengths shorter than the free-space electromagnetic wavelengths.

The aim of this thesis is to present our studies on three novel applications of metamaterial-based structures for manipulating MI waves. The flexible designs of metamaterial-based structures allow one to tailor the dispersion characteristics of MI waves. Analytical models are established based on the MI wave properties, which are verified by numerical and experimental results.

We first propose an approach for signal-guiding to specified directions and realising near-field directionality via multiple channels in a MI waveguide, which is potentially useful for wireless power or data transfer. Employing two sources with a phase difference to a MI waveguide can suppress the waves travelling to one end. Analytical calculations and experimental validations are presented for both axial and planar structures operating in the microwave regime. Selective unidirectional signal propagation is also demonstrated for nanostructured metamaterial arrays, where there is purely electric coupling and electroinductive (EI) waves are supported, with analytical predictions verified by numerical calculations. Separating the sources by two unit cells leads to a split in the passband, and MI waves travel in opposite directions within the two branches. Such a system can be treated as a special case of diatomic structures with dual dispersion branches featuring both forward and backward waves. We thus propose and prove a fundamental rule that the direction of guided signals is controllable by the forward or backward nature of the supported MI or EI waves in a structure.

The sensitivity of resonant meta-atoms to the variations in local electromagnetic fields makes MI waveguides attractive for near-field remote sensing applications. We devise a 1D position sensor that supports MI waves. With single-port probing, a low-complexity algorithm (we named it as the Odd-Even algorithm) is developed for localising a metal object in close proximity. The localisation procedure relies on the unique reflection patterns of MI waves due

to the standing waves formed between the signal injection point and the defect in the array created by the presence of the metal object. Weaker interactions between the object and the defect lead to increased difficulties for localisation. It is shown that terminating the array end with a matching load can suppress the interfering reflections, and improve localisation accuracy. The accuracy of the Odd-Even algorithm tested on the measured and analytically calculated reflection patterns are presented. In this proof-of-principle study, the possibility for remote discrete localisation of a conducting object on the MI sensing waveguide using a low-complexity algorithm has been demonstrated.

We then proceed to analyse far-field properties of structures supporting MI waves. Superdirectivity refers to antenna structures with directivity higher than that of a phased array of the same size, and it can be realised by a dimer of two magnetically coupled split ring resonators (SRRs), by exciting only one of the elements and imposing MI waves. The slow-wave nature of MI waves enables rapid spatial variation in the current distribution among elements, which is essential for achieving superdirectivity. In order to enable quick characterisation of superdirective structures that can be approximated as dipoles, we introduce new 2D equivalents to the traditional 3D directivity. The theoretical maximum achievable directivity values as well as the optimum conditions, for both the 3D and planar directivities are derived. Analytical results are verified and supported by the observations based on numerical calculations. It is shown that by optimising the planar directivity in the azimuthal plane, the 3D directivity is optimised simultaneously. We also demonstrate superdirectivity experimentally by measuring the in-plane field distribution produced by a dimer antenna. It is the first time that superdirectivity is realised using a PCB dimer structure.

Three areas of potential applications of MI waves are developed in this thesis, expanding the possibilities of near- and far-field manipulations using metamaterial-based structures by imposing MI waves.

Acknowledgement

I would like to thank my supervisors, Prof. Ekaterina Shamonina and Prof. Chris Stevens, who have given me all the guidance, support, and patience. Katya has been a role model to me as a brilliant female researcher dating back to my undergraduate course when I went to her tutorials and lectures, and she's s always encouraged me in pursuing an academic career. Chris had lots of creative ideas that triggered discussions. It was amazing how Chris could quickly design an experiment, and the Lego bricks in the lab definitely made the environment more vivid.

Dr. Anna Radkovskaya has shared a lot of her precious practical skills with me. Those chats with her during the breaks of experiments enlightened me. Anya was like a parent to me. Prof. Laszlo Solymar has helped me improving the scientific writing of papers and formed the papers into better shapes. Contributions and fruitful discussions from other collaborators and colleagues from OxiMeta are greatly appreciated.

Chris and Katya also introduced me to Metaboards, where I gratefully received funding for my course and joined the R&D team. Dr. Irina Khromova was my mentor at the company. Discussions with Irina were always inspiring, and more importantly, her love for life and the great work-life balance were motivating. I enjoyed my time working with colleagues at Metaboards, and I loved those game nights after work.

Dr. Son Chu has been a great senior and a good friend to me. Shan shared a lot of experience with me and gave me helpful tips, and I'm really excited to be able to work with him again after finishing the course. Lianbo and Andrea, who were also members of our research group when I joined, made me feel very welcome and gave me lots of great advices.

Taking a DPhil course wasn't an easy decision to make, and I had wholehearted support from my family. My mother was always there for me, telling me that I can do anything and be anywhere I want to. My grandpa wasn't talkative, but he did write about how he's been so proud of me in the family stories he gave me. I only met Kailun at the start of my course but I wish that happened earlier. He really had his ways when I got overly anxious about anything. I couldn't have gone so far without his support.

List of Publications

Papers

[1] J. Yan, A. Radkovskaya, S. Kiriushechkina, I. Khromova, C. Stevens, L. Solymar, E. Shamonina, 'A method for optimising superdirectivity of coupled meta-atoms via planar directivity evaluation,' *IEEE Open J. Antennas Propag.,* **1**, 300 (2020).

[2] J. Yan, C. J. Stevens, E. Shamonina, 'A metamaterial position sensor based on magnetoinductive waves,' *IEEE Open J. Antennas Propag.,* **2**, 259 (2021).

- included into a Special Selection of 27 articles published in 2021 by the journal, *Spotlight on Women's Research in Antennas and Propagation*.

[3] S. Chu, M. S. Luloff, J. Yan, P. Petrov, C. J. Stevens, E. Shamonina, 'Magnetoinductive waves in attenuating media,' *Sci. Rep.*, **11**, 7679 (2021).

[4] J. Yan, A. Radkovskaya, L. Solymar, C. J. Stevens, E. Shamonina, 'Switchable unidirectional magnetoinductive waveguide,' *IEEE Open J. Antennas Propag.*, (Submitted, 2022).

Conferences

[1] J. Yan, A. Radkovskaya, A. Vallecchi, C. J. Stevens, E. Shamonina, 'Demonstration of superdirectivity for PCB split ring dimers,' *12th Eur. Conf. Antennas Propag. (EuCAP)*, London, UK, 2018.

[2] J. Yan, E. Shamonina, C. J. Stevens, 'Planar directivity of a dipole array,' *12th Int. Congr. Artif. Mater. Nov. Wave Phenom. (Metamaterials),* London, UK, 2018.

[3] S. Chu, M. N. Hasan, J. Yan, C. C. Chu, 'A planar super wideband annular ring monopole antenna with time domain characterization,' *Asia-Pacific Microwave Conference (APMC),* Kyoto, Japan, 2018.

[4] C. J. Stevens, J. Yan, E. Shamonina, 'A metamaterial position sensor based on magnetoinductive waves,' *13th Int. Congr. Artif. Mater. Nov. Wave Phenom. (Metamaterials),* Rome, Italy, 2019.

[5] D. Dhayaa, A. Radkovskaya, J. Yan, G. Dima, E. O'Hara, L. Solymar, E. Shamonina, 'Metamaterials for sensing conductive objects using time-domain reflectometry of magnetoinductive waves,' *16th Int. Congr. Artif. Mater. Nov. Wave Phenom. (Metamaterials),* Siena, Italy, 2022 (*submitted*).

Patent

[1] C. J. Stevens, J. Yan, E. Shamonina, 'Metamaterials for 1D location,' [applied, under process].

Contents

1 Thesis Outline **1**

2 Introduction **3**

2.1 Metamaterials 3

2.2 Magnetic and Electric Coupling 7

2.3 Magnetoinductive Waves 12

2.3.1 Background 12

2.3.2 Analytical Models 18

2.3.3 Near-Field Applications 25

2.3.4 Far-Field Applications 29

3 Controllable Unidirectional Waveguide **36**

3.1 Theory for Unidirectional Propagation 36

3.2 Adjacent Excitations 40

3.2.1 MHz Arrays 40

3.2.2 THz Arrays 51

3.3 Non-adjacent Excitations 60

3.3.1 Results Based on MHz Arrays 60

3.3.2 Monoatomic and Diatomic Structures 63

3.4 Summary 69

4 Near-Field Position Sensor **71**

4.1 Structure 72

4.1.1 MI Waveguide 72

4.1.2 Defect Element 73

4.2 Reflections of MI Waves 75

4.2.1 Theoretical Model 75

4.2.2 Experimental Verification 79

4.2.3 Resolvability 80

4.3 Method for Location Identification 83

4.3.1 Algorithm Based on Standing Waves 83

4.3.2 Odd-Even Algorithm 84
4.4 Summary 90

5 Far-Field Superdirective Dimer Antenna **92**
5.1 Optimisation of Superdirectivity via Planar Directivity Evaluation 92
5.1.1 Optimisation of Directivity 93
5.1.2 Superdirectivity Conditions for Coupled Meta-Atoms 97
5.1.3 Numerical Calculations 100
5.2 Summary 105

6 Conclusions and Future Work **106**

7 Appendices **111**
7.1 Higher-Order Coupling Effects 111
7.2 Visualisation of Magnetic Fields 112
7.3 Numerical Calculation Setup in CST 115
7.4 Demonstration of Superdirectivity 117

References **137**

1 Thesis Outline

In this thesis, we develop three areas of potential applications of magnetoinductive (MI) waves, which expand the capabilities of MI structures both for the near-field and far-field wave manipulations. The work concerns the dispersion characteristics of MI waves supported by metamaterial-based structures composed of magnetically coupled resonators.

Chapter 2 begins with an introduction of metamaterials. Foundations of such artificial materials are laid, introducing reported methods of tailoring the effective electromagnetic properties by designs of the composite meta-atoms and electromagnetic interactions between them. An overview of MI waves and methods of manipulating MI wave propagation is presented. Diatomic structures that have more degrees of freedom in the designs are discussed. Analytical approaches we used to study the MI wave properties are introduced. Principles of tailoring the MI wave properties in metamaterial-based structures are explained. We summarise applications of MI waves in both the near-field and far-field ranges, setting the context for the novel applications we propose in this thesis.

Chapter 3 proposes a novel method for realising selective propagation direction of MI waves confined in a 1D waveguide. An analytical model is developed for realising signal-guiding functions of a MI waveguide based on the principle of near-field interference. Experimental verification obtained for structures operating in the MHz frequency range is presented. The same approach is verified based on analytical and numerical calculations for nanostructures which operate in the THz range and support electroinductive waves. By increasing the separation between the sources, multiple branches, with selective unidirectional propagations of MI waves, can be created within the passband of the MI waveguide. This can be explained by treating the structure as a special case of the diatomic structures, with identical meta-atoms within each unit cell. Such a diatomic structure supports forward and backward waves in different frequency ranges within the passband. The corresponding analytical models verified by experimental results are presented. The fundamental phenomenon of selective unidirectional signal propagation due to the forward or backward nature of the waves is explained and demonstrated.

Chapter 4 presents a novel near-field metamaterial position sensor based on MI waves. The interactions between a conductive object in close proximity and the MI array are quantised in the form of the changes in the resonant characteristics of the affected meta-atom, which

acts as a defect. The reflections of the injected signals are calculated analytically and verified experimentally. The latter part of the chapter introduces the Odd-Even algorithm for discrete localisation of the metal object on the waveguide. We have shown that the accuracy of the algorithm may be improved by introducing terminations which reduce reflections from the end of the array.

Extending from the near-field to the far-field interactions between the MI waves and the electromagnetic environment, superdirective dimer antennas are studied in Chapter 5. The idea of realising superdirectivity by imposing MI waves on coupled antenna array structures is introduced. The concept of planar equivalents to the 3D directivity is introduced, and optimum superdirectivity conditions are derived for both the planar and 3D directivities by developing a novel method which enables rapid optimisation of superdirective antennas modelled as dipoles. Numerical results verifying the analytical conditions are provided, demonstrating an increase of directivity for a dimer to 5.2, close to the theoretical maximum. Based on numerical and experimental results of the field distribution in the azimuthal horizontal plane, we demonstrate superdirective dimer antenna for the first time on PCB, validating theoretical predictions, and thus proving the possibility of rapid prototyping for superdirective structures.

Chapter 6 provides a summary of the applications of MI waves proposed and analysed in this thesis. Potential research directions in the future are discussed.

Details of analytical derivations and numerical techniques are presented in the appendices forming Chapter 7.

2 Introduction

2.1 Metamaterials

Metamaterials are engineered materials formed by elements called meta-atoms which can be designed and tailored individually to realize extraordinary properties not found in natural materials [1, 2], for example to achieve negative permittivity (ε) and negative permeability (μ) simultaneously at the same frequency. Examples of metamaterial-based structures are shown in Fig. 2.1 and Fig. 2.2. Figure 2.1 is a photo of a structure studied by our research group, which is a one-dimensional (1D) metamaterial-based structure made using the printed circuit board (PCB) technique. Figure 2.2 is a photograph [3] of a metamaterial structure with negative index of refraction. For metamaterials, the size of the composite unit cells is less than one-tenth of the operational electromagnetic wavelength. This size limit discriminates metamaterials from photonic bandgap materials [4] - another type of engineered periodic structure with the lattice period comparable to the wavelength of operation, and the structure can be designed to tailor the spectral properties of the band gaps [5, 6].



Figure 2.1: Photo taken for a 1D PCB metamaterial-based waveguide structure by our group. The meta-atoms are square split ring resonators of 10 mm side-length, with mounted capacitors soldered between the gaps to tune the resonance to the MHz frequency range. The centre-to-centre distance between adjacent meta-atoms are 10.5 mm.

Research directions of metamaterials are diverse. In acoustic metamaterials the first demonstration of artificial materials in [7] used rubber-coated spheres to create localised resonant structures, and disordered composite formed from such engineered structures exhibit negative effective elastic constants within certain frequency ranges. Other applications of acoustic metamaterials include acoustic cloaking [8] and far-field imaging below the diffraction limit [9, 10]. Metamaterials can also be designed to realise exceptional mechanical functionalities such as being flexible or programmable [11, 12], or exhibiting negative Poisson's ratio [13, 14]. Extensive optical and electromagnetic metamaterial structures have been reported [15, 16]. In this thesis, we focus on the possibilities of manipulating the electromagnetic waves supported by metamaterial-based structures.

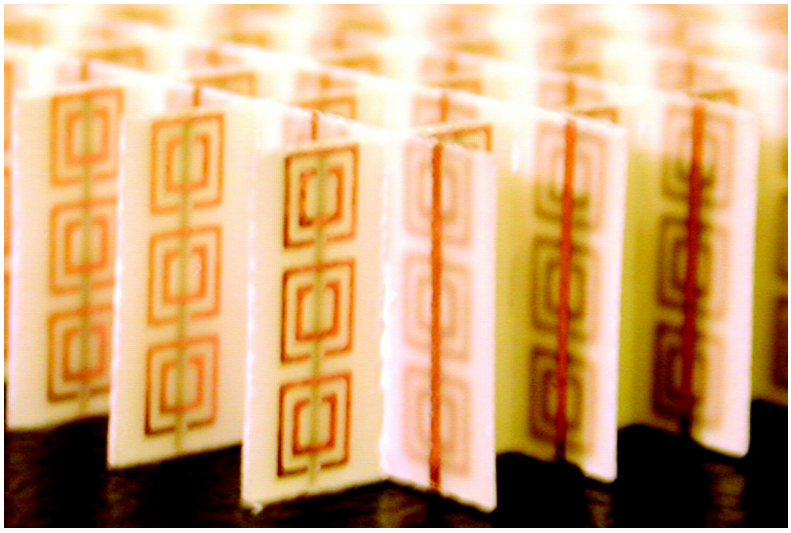


Figure 2.2: Photo of the sample under study in [3] with negative ε, μ and therefore negative refraction index. The sample is made of copper square split ring resonators and wire strips printed on fiber glass circuit boards.

As electromagnetic waves travel through a medium, when the wavelengths are much larger than the particle size, the interactions of the waves with individual particles can be averaged, so that the medium can be considered as continuous instead of being discrete. In such cases, the effective-medium approximation is valid, and the electromagnetic properties of a material can be represented by its permittivity ε and permeability μ. Natural substances can have negative ε or negative μ at certain frequencies, but not both negative values simultaneously. Metals have negative ε below their corresponding plasma frequency [17], ω_p, and the effective ε follows the Drude model. Rotman [18] showed that artificial structures such as a periodic lattice of metallic rods can also have $\varepsilon < 0$ and the corresponding plasma frequencies are tunable. Thompson [19] showed that ferrites exhibit negative permeability, and later Pendry [20] demonstrated that negative effective permeability can be achieved by an array of split ring resonators (SRRs) within a certain operational frequency range which can be tuned by the properties of the composite elements.

What is so fascinating about achieving negative permeability and permittivity simultaneously is that negative refraction can be realised. Backward waves were discussed in 1904 by Schuster [21], who showed that negative refraction would occur at the boundary of two hypothetical media, one supporting forward waves and the other supporting backward waves, with the similar idea discussed again in 1945 by Mandelshtam [22]. The definitions of forward and backward waves based on the directions of energy transfer and wave propagation will be dis-

cussed in Section 2.3.1. Veselago [23] proposed in 1967 that a flat lens with negative refractive index, realised by having both negative permeability and permittivity, could bring a diverging beam into a converging one. It was not until 2000 when Smith et al. [24] designed an artificial material exhibiting both $\varepsilon < 0$ and $\mu < 0$ within the same frequency band, that Veselago's postulate was demonstrated experimentally. The metamaterial structure was made by superimposing the two kinds of resonant elements discussed previously, the metal rods (giving $\varepsilon = -1$) and the SRRs (giving $\mu = -1$). By creating alternate periodic structures of split ring resonators and metallic rods, negative refractive index was achieved. Another set of experimental results on a similar negative-index material structure with each unit cell containing one SRR and two rods was presented by Li et al. in [25].

Due to the unusual properties of metamaterials, there has been a lot of published work on related applications. Pendry [26] discussed the possibility of overcoming the diffraction limit and realising 'perfect lens' using metamaterial structures designed to have negative refraction index. Evanescent waves can be enhanced when travelling through a slab with negative refractive index, recovering the high spatial frequency components of the electromagnetic field and therefore greatly improving the resolution of imaging subwavelength objects - a technique generally called the subwavelength imaging [27–33]. The meaning of 'subwavelength' is that the object size is much smaller than the operational wavelength. The direction of the electromagnetic waves penetrating the metamaterials can be controlled if the structures are designed to have desired spatial distributions of effective ε and μ [34]. The ability of metamaterials in guiding electromagnetic waves lead to the realisation of invisibility cloaking [35–37]. Visible light or other electromagnetic waves can be deflected around objects surrounded by a metamaterial cloak, making the object appear almost undetectable to devices working within certain frequency ranges covered by the operational bandwidth of the cloaking devices. Tunable transmission lines with both negative permeability and negative permittivity, made of varactor-loaded SRRs magnetically coupled to coplanar waveguides, were discussed in [38]. Stop band filters made from coplanar waveguides magnetically coupled to SRRs were discussed in [39], and it was shown that by tuning the SRRs properly, the stop band can be widened and tailored. In [40], a tunable notch filter was demonstrated by incorporating the varactor-loaded SRRs to the design.

The losses in metamaterial structures impede practical device applications, and there are

several strategies to mitigate losses [41]. It was discussed in [42] that reducing the surface roughness of silver in the fabrication process reduced the intrinsic ohmic losses of meta-atoms made using such a technique. Instead of metallic structures, dielectric [43] and semiconductor [44] metamaterials have been developed, exhibiting comparatively low losses at the optical frequency range. Another method to reduce losses is to use active metamaterials [45], such as to incorporate gain materials created from optically pumped dye molecules.

The ability of metamaterials to deflect and guide the electromagnetic fields that they are exposed to, as well as the tailorability of the structures, make them attractive for applications in both the near-field and far-field ranges. An extended survey of applications of magnetic materials supporting magnetoinductive waves, which propagate relying on magnetic inter-element coupling, will be provided in Section 2.3.1.

Generally the metamaterial structures that we are interested in are formed by resonating unit cells. Electromagnetic properties of a metamaterial structure depend on the properties of the individual elements (meta-atoms, which can be designed individually), as well as on the interactions between neighbouring meta-atoms forming the structure.

A large variety of different types of meta-atoms were proposed in the past. Hardy and Whitehead [46] introduced the SRR for magnetic resonance applications in the microwave frequency range. Despite their simple structure design, SRRs can have high quality factor and the size of the element is much smaller relative to the operational wavelength. Many variants of the SRR have been developed, including SRRs with different numbers of splits [47, 48], complementary split rings [49, 50], open version of SRRs [51], varactor-loaded SRRs [40], 'Swiss roll' resonator [20], planar spiral resonators [52], three-dimensional helix resonators [53], and capacitively-loaded SRRs with the addition of capacitor in its gap to tune the resonant frequency [54]. Some of these different variations are illustrated in Fig. 2.3.

Designs of different geometries for the meta-atoms enable tailoring of the resonant characteristics for individual elements. In order to manipulate the waves supported by the metamaterial-based structures, another approach is to tailor the mutual coupling between the elements. The magnetoinductive waves, to be discussed in Section 2.3, travel in structures relying on magnetic coupling. Metamaterials formed from a variety of meta-atoms, including those listed above, support propagation of such waves, as long as there are magnetic interactions between the composite cells. In this thesis, we focus on a simple form of singly split resonator with

the schematic shown in Fig. 2.4, which can be modelled as an LCR resonator circuit. Adding an external capacitor into the gap of the SRR allows for tuning of the resonant frequency and forms the capacitively-loaded SRR.

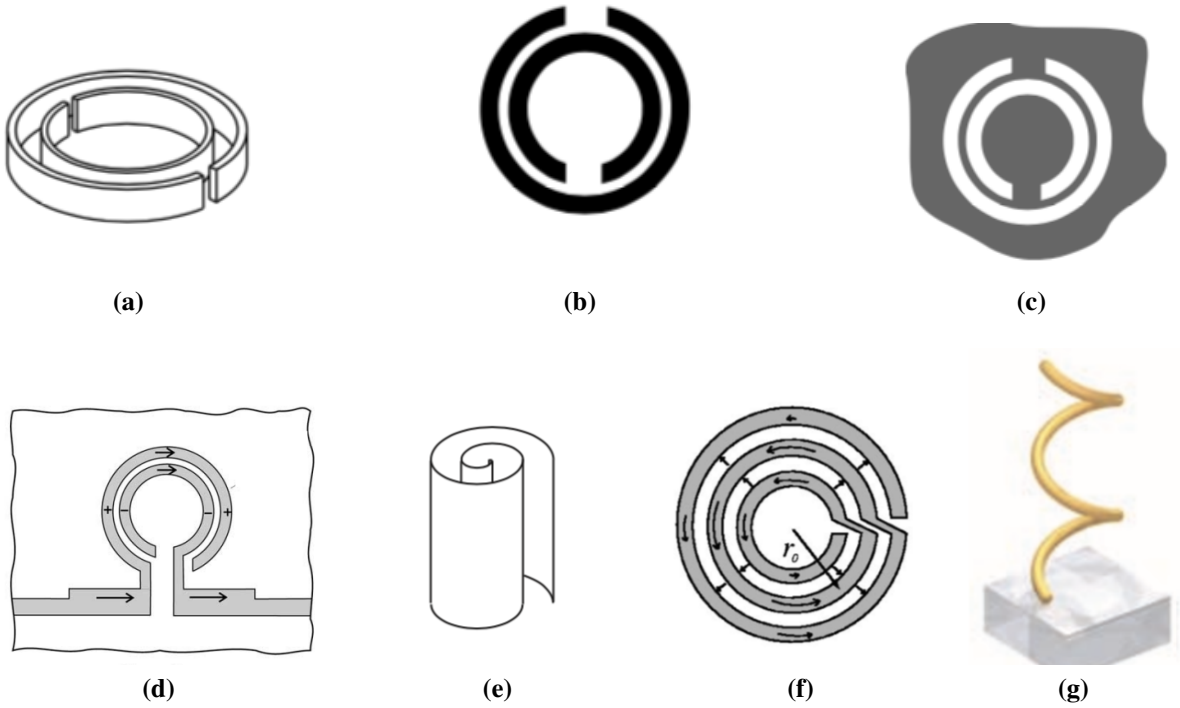


Figure 2.3: Split ring resonator varieties of different shapes, taken from the corresponding references. (a) Split pipe [2], (b) double split ring [2], (c) complementary split ring [2], (d) open version of SRR [51], (e) 'Swiss roll' [2], (f) planar spiral resonator [52], (g) gold helix resonator [53].

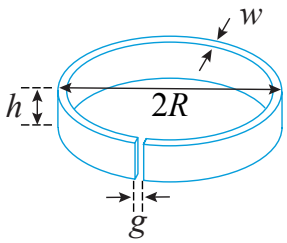


Figure 2.4: Illustration of a single SRR with height h, width w, radius R and gap size g.

2.2 Magnetic and Electric Coupling

When a single SRR shown in Fig. 2.4 is excited, say, by a voltage source, the current induced in the SRR can be characterised by the self-inductance L. The self-capacitance C for a resonator represents the relationship between the accumulated charges and the induced voltage, and for

an unloaded SRR, the effects from both charges accumulating on the gap of the SRR and those residing on the surface of it are taken into account by [55]

$$C = C_{\text{gap}} + C_{\text{surf}} \ , \tag{1}$$

where C_{gap} is the gap capacitance which is inversely proportional to the size of the gap, and C_{surf} is the surface capacitance. It was shown in [55] that even if the gap g is small relative to the radius R (for example $g/R < 0.03$) of the SRR, the surface capacitance cannot be neglected. For a capacitively-loaded SRR that forms most of the metamaterial-based structures discussed in this thesis, the self-capacitance C is dominated by the external capacitance C_{ext}. The values of the added capacitors were selected so that the resonant frequency ω_0 of the individual element is tuned to the desired value

$$\omega_0 = \frac{1}{\sqrt{L\,C}} \ . \tag{2}$$

When two resonators are placed in close proximity, there are electric and magnetic field interactions between them. It was shown in [56] that the coupling mechanism for two coupled unloaded SRRs may have both electric and magnetic contributions, depending on the relative orientations of the SRRs.

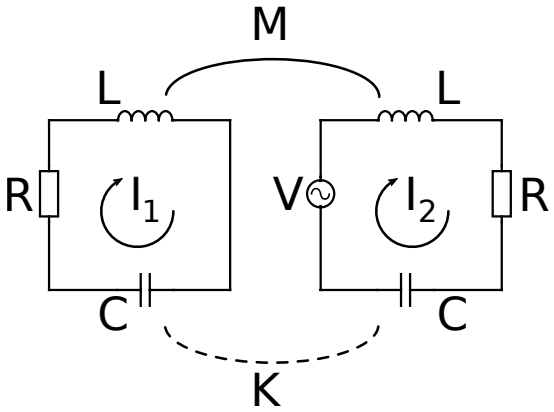


Figure 2.5: Equivalent circuit of two coupled resonators as LCR circuits, with both electric coupling (mutual capacitance K, dashed curve) and magnetic coupling (mutual inductance M, solid curve).

The circuit model for a coupled system is shown in Fig. 2.5. We define the electric coupling coefficient as

$$\kappa_{\text{E}} = \frac{2\,C}{K} \ , \tag{3}$$

where K is the mutual capacitance, and the magnetic coupling coefficient as

$$\kappa_{\mathrm{H}} = \frac{2M}{L} \ , \tag{4}$$

with M being the mutual inductance. The signs of κ_{E}, κ_{H} depend on the relative positions of the SRRs. The electric coupling coefficient κ_{E} is positive if the electric field produced by the equivalent electric dipole, positioned approximately between the gap of one of the SRRs, is pointing in the same direction as the electric field originating from the electric dipole in the other element. The sign of κ_{H} is positive if the magnetic field produced by one element does not change its direction when threading the other element, for example if they are axially aligned, to which we refer as the axial configuration. κ_{H} becomes negative if the SRRs are placed in the same plane, which is called the planar configuration in this thesis.

Element 2 in Fig. 2.5 is excited with a voltage source of frequency ω while no excitations are applied to element 1, which is a passive element coupled to element 2. The relationship between the currents in the two resonators, I_1 and I_2, can be expressed based on Kirchhoff's law,

$$\begin{cases} Z_0\, I_1 + j\omega M I_2 + \dfrac{I_2}{j\omega K} = 0 \\ \\ Z_0\, I_2 + j\omega M I_1 + \dfrac{I_1}{j\omega K} = V \end{cases} \ , \tag{5}$$

where

$$Z_0 = R + j\omega L + \frac{1}{j\omega C} \tag{6}$$

is the self-impedance of the resonating individual element. Solving the first equation in the simultaneous set of Eqn (5), the ratio between the currents can be written in the form

$$\frac{I_2}{I_1} = \frac{2}{\nu^2 \kappa_{\mathrm{E}} - \kappa_{\mathrm{H}}} \left(1 - \nu^2 - j\frac{\nu}{Q} \right) \ , \tag{7}$$

where

$$Q = \frac{\omega_0 L}{R} \tag{8}$$

is the quality factor, and the inverse of the normalised frequency by the resonant frequency is introduced as

$$\nu = \frac{\omega_0}{\omega} \ . \tag{9}$$

The total coupling coefficient can be defined as

$$\kappa_{\text{total}} = \kappa_{\text{H}} - \nu^2 \kappa_{\text{E}} \ , \tag{10}$$

then Eqn (7) takes the form

$$\frac{I_2}{I_1} = -\frac{2}{\kappa_{\text{total}}} \left(1 - \nu^2 - j\frac{\nu}{Q}\right) \ . \tag{11}$$

As mentioned previously, the metamaterial-based structures discussed in this thesis are generally formed from capacitively-loaded SRRs. The external capacitors soldered into the gaps confine the electric fields and therefore suppress the electric interactions between the SRRs. In this case, electric coupling effects can generally be neglected, and we are interested in the cases where magnetic coupling becomes the dominant coupling mechanism. Equation (5) simplifies to

$$\begin{cases} Z_0\, I_1 + j\omega M I_2 = 0 \\ Z_0\, I_2 + j\omega M I_1 = V \end{cases} \ , \tag{12}$$

giving a current ratio

$$\frac{I_2}{I_1} = -\frac{2}{\kappa} \left(1 - \nu^2 - j\frac{\nu}{Q}\right) \ , \tag{13}$$

where $\kappa = \kappa_{\text{H}}$ is the total coupling coefficient κ_{total} by setting $\kappa_{\text{E}} = 0$ as follows from Eqn (10). If lossless approximations are made for low-loss systems, Eqn (13) can be further simplified - i.e. when the quality factor Q is high, the current ratio becomes

$$\frac{I_2}{I_1} \approx -\frac{2}{\kappa}(1 - \nu^2) \ . \tag{14}$$

The mutual coupling between two SRRs can be tailored via two ways. One approach is to change the relative position of the resonators in the 3D space. The anisotropy of magnetic coupling was discussed in [57] by shifting one SRR in two directions simultaneously (both in the plane of the other element and in the direction normal to the element). As the relative position between the two SRRs varies, the system of two coupled elements undergoes transition from the axial configuration, with positive κ, to the planar configuration with negative κ, and at a point with a certain amount of overlap between the two resonators, the condition of zero

coupling $\kappa = 0$ can be realised. Another method to tailor the coupling mechanism is to change the relative orientation between two SRRs. The variation in the electric and magnetic contributions to the total coupling mode with the relative orientation between two unloaded SRRs was analysed in [58].

The coupling coefficient is purely real if we neglect the retardation effects. Retardation represents the delay in the induction of currents in the resonators of a metamaterial-based structure, due to the finite propagation speed of the electromagnetic radiation. This effect can be neglected if the size of the resonator is much smaller than the operational wavelength λ, for example for the capacitively-loaded SRRs. In such cases, the coupling between two loaded circular SRRs is practically independent of their relative orientations (characterised by the direction in which their gaps are facing), and it can be considered purely magnetic, with the coupling coefficient being a purely real quantity.

We model the resonators carrying currents as filament current elements. When the circumference of the SRR is small compared to λ, the current in the SRR is treated as spatially independent and homogeneous across the filament. On the other hand, as the size of the SRR or the separation between the elements becomes larger compared to the wavelength, retardation should be taken into account for coupling coefficient calculations [58–60], which results in complex coupling coefficients. In addition, the current distribution in the filament model of the resonators becomes spatially dependent in this case. Taking a circular SRR resonating in the infrared spectral range as an example [61], the current density reaches maximum at the middle of the circumference, opposite to the gap, and is zero at the edges of the gap. In such cases, the relative orientation of the SRRs affects the resultant coupling coefficient and hence also the properties of waves supported by the formed structures.

As we scale down the size of an SRR to the nanometer range, the resonant frequency f_0 of the SRR increases to enter the THz range, but further reduction of the size will lead to a saturation in f_0 [62] due to the rise in kinetic inductance L_{kin} of the element, which represents the inertia of electrons in metal structures. As frequency increases, kinetic inductance starts to dominate the self-inductance L of an SRR, rather than the magnetic inductance L_{mag}. The self-inductance for an SRR is

$$L = L_{\text{mag}} + L_{\text{kin}} \ , \tag{15}$$

and for the magnetic coupling coefficient, we can write

$$\kappa_{\mathrm{H}} = \frac{2\,M}{L_{\mathrm{mag}} + L_{\mathrm{kin}}}\ . \tag{16}$$

The effect of increased L_{kin} on the suppression of magnetic coupling effect indicated by Eqn (16) for SRRs operating in the THz frequency range is discussed in [58], and it is pointed out that the electric coupling may even become the dominant coupling mechanism in nanostructured metamaterials.

2.3 Magnetoinductive Waves

2.3.1 Background

Introduced in 2002 [54], MI waves were shown to propagate in a metamaterial array by virtue of the magnetic coupling between resonating elements. MI waves have wavelengths much shorter than the free space electromagnetic waves of the same frequency. Theoretical analysis of 2D and 3D structures supporting MI waves were presented in [63]. Experimental demonstration of metamaterial-based structures hosting MI waves were described in [64], and arrays of coupled 'Swiss rolls' were shown to support MI waves in [65]. Waves that propagate based on magnetic coupling were also studied for nanostructured metamaterials [66, 67].

A theoretical study regarding potential applications of MI waveguides was provided in [68], including discussions of power transfer from one waveguide to another and application of MI waveguides for directional coupler structures. A comparison between traditional transmission lines and MI waveguides was also provided. It was further demonstrated theoretically in [69] that, by changing the layout of composite capacitively-loaded SRRs, the supported MI waves in metamaterial-based structures can be manipulated, and different devices with analogies to some traditional optical and microwave components can be realised. In [70], there is an analysis of transmission and refraction of MI waves travelling across two periodic 2D structures. Medium 1 was a planar-axial 2D structure with positive coupling coefficient in the x direction and negative coupling coefficient in the y direction, while medium 2 was a rotated version of medium 1, with the signs of the coupling coefficient in both the x and y directions reversed relative to those in medium 1, and the possibility of realising negative refraction was discussed. The method of analysing periodically loaded transmission lines was applied to model the inter-

actions between MI waves and electromagnetic waves in [71], where MI waves are shown to be similar to another kind of eigenmodes of a solid, i.e. the surface plasmon polaritons (SPPs).

In order to reduce the losses of MI waves in waveguide structures, it was pointed out in [72] that higher-order coupling effects should be much weaker than the first-order coupling between nearest neighbours, based on which double-sided PCB resonators were designed to realise low-loss MI waveguides. A discussion of the effects of higher-order couplings on the wave properties of MI waves was given in [73]. Travelling MI waves in a waveguide of finite length experience reflections, leading to inefficient operation of the structure. Terminations can be added to MI waveguides to eliminate reflections by selecting a frequency dependent terminating impedance Z_{T} [54] equal to

$$Z_{\mathrm{T}} = j\omega M\, e^{-jkd} \ , \tag{17}$$

where d is the separation between the elements in the structure, and k is the wave number, or the complex propagation coefficient defined as

$$k = \beta - j\,\alpha \ , \tag{18}$$

with β being the propagation coefficient, and α being the attenuation coefficient. Z_{T} is difficult to realise in practice since it is a complex number, and it is real only at the resonant frequency. Possible mechanisms to apply resistive terminations to a number of elements near the array end is discussed in [74], and it is suggested that geometrically varying values of terminations provide good suppression of reflections over a reasonable frequency range.

MI waves are slow waves with the group velocity lower than the speed of light. Group velocity represents the speed of energy transfer of the waves, and is defined as

$$v_{\mathrm{g}} = \frac{\partial\,\omega}{\partial\,k} \ . \tag{19}$$

MI waves are analogous to other slow waves such as acoustic waves and plasma waves. Acoustic waves arise from mechanical vibrations that can be either transverse or longitudinal, for example when external forces are applied to the natural lattices, ions and atoms vibrate about their equilibrium position due to the restoring electrostatic forces. When electrons are able to

move freely in metal structures, external sources excite the plasma waves in natural materials [75]. SPPs, also being slow waves, are light waves trapped on the surface of a conducting material due to their interactions with the free electrons in the conductor. The condition for SPPs to exist at an interface of two materials is for the permittivity ε to have opposite signs on either side of the boundary [2, 76]. The component of the wave vector **k** normal to the interface is purely imaginary, being an evanescent component, therefore wave propagation in the direction normal to the surface is not allowed. What this means is that SPP can be coupled to evanescent components of electromagnetic fields. The dispersion relationship of SPP was discussed in [2], and the expression, with $\varepsilon_{\mathrm{r}} = 1$, to model the behaviour of SPPs along a metal-vacuum interface is cited here as

$$\left(\frac{\omega}{\omega_0}\right)^2 = \frac{1}{2} + \left(\frac{k}{k_{\mathrm{p}}}\right)^2 - \sqrt{\frac{1}{4} + \left(\frac{k}{k_{\mathrm{p}}}\right)^4} \ , \tag{20}$$

where ω_{p} is the plasma frequency, and k_{p} is the wave number at the plasma frequency,

$$k_{\mathrm{p}} = \frac{\omega_{\mathrm{p}}}{c} \ , \tag{21}$$

with c being the speed of light in the vacuum. The corresponding dispersion characteristics is shown in Fig. 2.6 (red), with both axis normalised to the values at the plasma frequency. The light line is the blue oblique line with

$$\frac{\omega}{k} = c \ . \tag{22}$$

At low frequencies (small ω), the dispersion curve (red) tends to coincide with the light line, whereas the upper cut-off frequency is at

$$\omega = \frac{\omega_{\mathrm{p}}}{\sqrt{1+\varepsilon_{\mathrm{r}}}} = \frac{\omega_{\mathrm{p}}}{\sqrt{2}} \ , \tag{23}$$

shown by the dashed horizontal asymptotic line. It should be noted that both v_{g} and v_{p} tend to the speed of light at low frequencies, but the dispersion curve lies always to the right of the light line, with $v_{\mathrm{g}} < c$, representing slow waves, and with $k > \omega/c$, thus representing short waves.

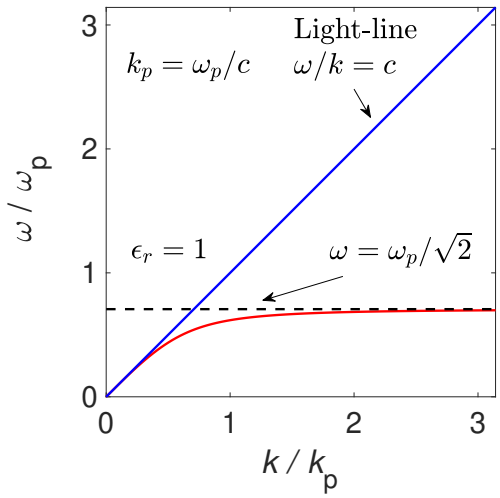


Figure 2.6: Dispersion curve (red) for SPPs at a metal-vacuum interface, with $\varepsilon_r = 1$. The light-line, with $\omega/k = c$ where $c = 3 \cdot 10^8$ m/s is the speed of light, is plotted as the blue oblique line. The dashed horizontal line marks the cut-off frequency at $\omega = \omega_\mathrm{p}/\sqrt{2}$.

Phase velocity of a wave with a single frequency is defined as

$$v_\mathrm{p} = \frac{\omega}{k} \ , \tag{24}$$

and its direction is associated with the direction of the wave vector **k**. For waves travelling within a simple 1D structure, when the group velocity and phase velocity have the same direction, the waves are termed as forward waves. On the other hand, if we have v_g and v_p in opposite directions, the waves are termed as backward waves. To generalise the classification rules of forward or backward waves for 2D and 3D structures, we recall that v_g represents the speed of energy or power transfer, which is related to the Poynting vector **S** [2] defined as the power per unit surface, and

$$\mathbf{S} = \frac{1}{2}\mathrm{Re}\{\mathbf{E} \times \mathbf{H}^*\} \ , \tag{25}$$

with **E** and **H** representing the electric and magnetic field, and the asterisk denotes the complex conjugate. The Poynting vector gives the magnitude and direction of the electromagnetic power flow evaluated at a selected point in space. To decide the forward or backward nature of the waves, we evaluate the scalar product between the Poynting vector and the wave vector **k** – if

the sign of the scalar product is positive, then the waves are forward waves, i.e.

$$\begin{cases} \mathbf{S} \cdot \mathbf{k} > 0, & \text{forward waves} \\ \mathbf{S} \cdot \mathbf{k} < 0, & \text{backward waves} \end{cases} . \tag{26}$$

Acoustic waves supported by natural materials composed of identical elements are forward waves, and yet diatomic structures formed by alternating atoms of different masses, for example sodium chloride NaCl, exhibit an optical branch [77] supporting the travelling of backward waves. A more general statement was also suggested, that the number of branches will be equal to the number of different masses (or composite units) in the structure.

There is little freedom in tailoring the dispersion characteristics of diatomic natural materials. However, analogous to the acoustic waves, MI waves travelling in metamaterial-based diatomic structures have two branches in the dispersion characteristics. It is possible to tailor their wave properties with more flexibility by careful designs of individual elements, as well as the electromagnetic interactions between them.

Metamaterial-based structures supporting MI waves can be designed to have two resonators per unit cell, so that both forward and backward waves can be allowed to propagate within the frequency passband, and there is more freedom in tailoring the wave properties. We start with a simple example of diatomic structures with two detuned elements (of different resonant frequencies) within each cell [78]. Both the planar and axial configurations were studied, with both structures shown to allow the propagation of backward waves in the upper frequency range and that of forward waves in the lower frequency range within the passband. However, for an axial array, the upper branch was shown to be an 'optical' branch, with currents in the two detuned resonators of a diatomic cell being out-of-phase, and the lower branch was an 'acoustic' branch with the currents within the cell being in phase. The nature of the two branches were reversed for a planar array, i.e. the upper branch became an acoustic branch. There was a stop band between the two branches for both arrays. The theoretical dispersion relationships for the diatomic lines were verified experimentally in [79]. Capacitors of different values were used to tune the two elements within each unit to have different resonant frequencies. The variation in the magnetic coupling between two SRRs with their relative orientations, i.e. if they are in parallel planes or normal to each other, as well as their relative shifted distances, was

shown in [57]. Studies of various configurations of two coupled lines of elements were also presented, including shifted planar lines, and coupled planar-axial lines. The anisotropy in the magnetic coupling between resonators has introduced more freedom in tailoring the dispersion characteristics of diatomic structures. A structure made from two layers of strongly coupled MI waveguides (or 2D surfaces supporting MI waves) exhibited a stop band between two branches in its passband [80], and subwavelength imaging was realised within the stop bands of the dispersion characteristics, where transverse propagations of MI waves along the arrays were suppressed. Diatomic chains with coupling coefficients of alternating signs from element to element were studied in [81]. The signs and nature of coupling coefficients were varied by changing the relative orientations between the identical resonators. It was shown that with the same magnitude of the alternating electric and magnetic coupling coefficients, the stop band between the two branches was closed up for the balanced diatomic chain. The tailorability of MI wave properties opens the possibility for various practical applications.

2.3.2 Analytical Models

In this thesis, we adopted two general approaches to analyse structures supporting MI waves. The first method is to treat each resonator in the metamaterial-based structures discretely and model the structure as a network of coupled LCR circuits such as that illustrated in Section 2.2. The impedance matrix of the system is constructed, and given the external excitations as voltage applied to the elements, which can be expressed as a vector, we are able to obtain the current distribution for the entire structure.

Considering a 1D linear array of N magnetically coupled resonators, with only the first-order coupling being significant, and only the last element N is excited with a voltage of 1 V, the simultaneous equations describing the relationship between the currents I_n (in element n, where $n = 1, 2, 3...N$) and the external applied voltages can be written in a matrix equation form, based on the Ohm's law of $\mathbf{V} = Z\,\mathbf{I}$

$$\mathbf{V} = \begin{pmatrix} 0 \\ 0 \\ 0 \\ ... \\ 1 \end{pmatrix} = \begin{pmatrix} Z_0 & j\,\omega M & 0 & 0 & 0 & ... & 0 \\ j\omega M & Z_0 & j\omega M & 0 & 0 & ... & 0 \\ 0 & j\omega M & Z_0 & j\omega M & 0 & ... & 0 \\ ... & & & & & & \\ 0 & 0 & 0 & 0 & 0 & j\omega M & Z_0 \end{pmatrix} \begin{pmatrix} I_1 \\ I_2 \\ I_3 \\ ... \\ I_N \end{pmatrix}, \tag{27}$$

so that the diagonal elements of the $N \times N$ impedance matrix Z are equal to the self-impedance Z_0 of the resonators, and the off-diagonal terms of $j\omega M$ represent nearest-neighbour magnetic interactions. Inverting the impedance matrix and evaluating

$$\mathbf{I} = Z^{-1}\,\mathbf{V} \tag{28}$$

gives us the current distributions. The vector $\mathbf{V}$ may vary if different excitation conditions are applied, for instance when a 1D array is excited near the centre, a case that will be discussed in Chapter 3. In addition, higher-order coupling modes may be taken into account by populating the non-zero mutual inductance terms into respective locations of the matrix – e.g. when there's second-order coupling, the matrix elements

$$Z_{n,\,n+2} = Z_{n+2,\,n} = j\omega M_2\ . \tag{29}$$

For a system of N resonators, there are N resonant modes, also called the eigen-modes, which can be found by evaluating the eigenvalues of the Z matrix in Eqn (27). Take two coupled elements as an example. Writing the 2×2 impedance matrix for the dimer structure following Eqn (27) as

$$Z = \begin{pmatrix} Z_0 & j\omega M \\ j\,\omega M & Z_0 \end{pmatrix} , \tag{30}$$

with the corresponding eigenvalues $\lambda_{1,2}$ being

$$\lambda_{1,2} = Z_0 \pm j\omega M \ , \tag{31}$$

and the resonant eigenmodes occur when the eigenvalues are nearly zero under lossless conditions [2]. The solution to this is then

$$\omega_{1,2} = \frac{\omega_0}{\sqrt{1 \pm \kappa/2}} \ , \tag{32}$$

recall that $\kappa = 2M/L$ is the first-order magnetic coupling coefficient. Close to $\omega_{1,2}$, the currents in the two resonators, I_2 and I_1, both are expected to exhibit resonances.

To conclude, this method that we call the 'V = ZI' calculation is of reasonable computational complexity and gives information about the current distribution among meta-atoms in a resonant structure.

The second approach is to consider the wave properties, based on the dispersion relationships, of the MI waves supported by the metamaterial based structures. The wave properties analysis enables designs of the structure for manipulating the MI waves.

For an infinite array of magnetically coupled resonators, the current in element n can be written as

$$I_n = I_0\, e^{-jnkd} \ , \tag{33}$$

where kd was defined in Eqn (18). With the assumption that there is only first-order coupling, the MI waves supported by such a structure can be modelled in element n based on the Kirchhoff's equation

$$Z_0 I_n + j\omega M \left(I_{n-1} + I_{n+1}\right) = 0 \ , \tag{34}$$

where Z_0 is the self-impedance of an LCR resonator as defined by Eqn (5), and M is the first-

order mutual inductance. Substituting the expressions of $I_{n-1},\ I_n$, and I_{n+1} from Eqn (33) into Eqn (34), we get

$$Z_0 + j\omega M(e^{-jkd} + e^{jkd}) = 0 \ , \tag{35}$$

the non-linear dispersion relationship of the waves then follows [63],

$$\frac{\omega_0^2}{\omega^2} - 1 + \frac{j}{Q'} = \kappa \cos kd \ , \tag{36}$$

where

$$Q' = \frac{\omega L}{R} = \frac{\omega}{\omega_0} Q \ , \tag{37}$$

With positive coupling $\kappa > 0$ between the meta-atoms in a MI waveguide, forward waves are supported, and negative coupling gives rise to backward waves travelling in the structures. The group velocity v_{g} defined in Eqn (19) can be obtained from the dispersion diagram (often called the $\omega - k$ diagram) by evaluating the instantaneous slope of the dispersion curve. Recall that the phase velocity v_{g} is the ratio between ω and k, and that MI waves travelling in a 1D structure are forward waves when v_{g} and v_{p} have the same sign. As an example, dispersion curves are plotted for forward and backward MI waves in Fig. 2.7 based on Eqn (80) with $\kappa = \pm 0.13$ and under lossless assumptions (neglecting the Q'-term). The red curves are for forward waves which is based on $\kappa = 0.13$, and the blue curves are for backward waves with $\kappa = -0.13$. The red curve shows positive instantaneous slopes within the passband, also representing positive group velocities, as expected for forward waves, while the blue dashed line has negative slope within the passband, confirming the backward wave nature. The vertical axis, which is the frequency, is normalised to the resonant frequency. The passband that allows MI wave propagation is clearly seen as βd varies between 0 and π. The dashed curves show the dispersion relationships taking into account up to the third-order couplings - the axial structure has $\kappa_{1,2,3} = 0.13,\ 0.02,\ 0.01$, and the planar structure has $\kappa_{1,2,3} = -0.13,\ -0.02, -0.01$. Positive higher-order coupling coefficients for the axial structure lead to the passband shifting to lower frequencies, while the passband for the planar structure shifts to higher frequencies due to the higher-order interactions – the explanations for this will be provided below.

The passband is the frequency range within which the MI waves are allowed to propagate, seen clearly in Fig. 2.7 for the lossless cases. Higher-order field interactions will be crucial

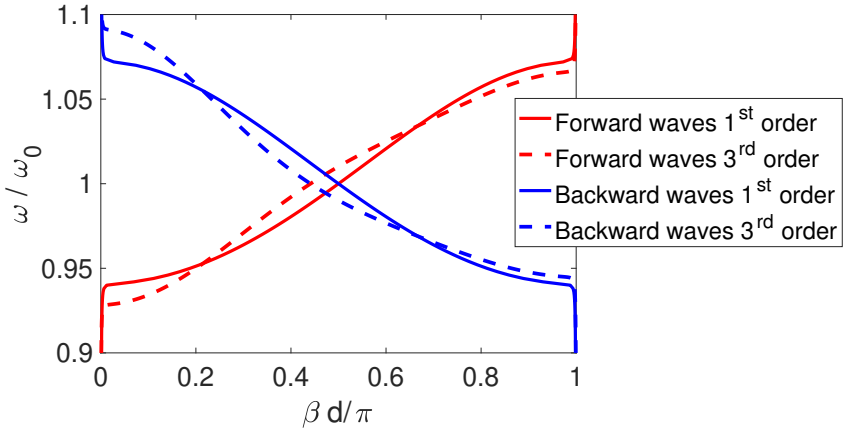


Figure 2.7: Dispersion curves showing normalised frequency ω/ω_0 over $\beta d/\pi$ under lossless conditions for both forward waves (red) and backward waves (blue). Note that the group velocity is the instantaneous slope of the curves based on Eqn (19), being positive within the passband for forward waves and negative for backward waves.

in later sections, therefore we proceed to account for up to the third-order magnetic coupling coefficients and derive the expressions for the passband frequency ranges. The second and third-order coupling coefficients are generally much weaker than the first-order coupling coefficient, but they are not negligible in some cases.

Based on Kirchhoff's law, we can write an extended form of Eqn (34) as follows

$$Z_0\, I_n + j\omega M_1\,(I_{n-1} + I_{n+1}) + j\omega M_2\,(I_{n-2} + I_{n+2}) + j\omega M_3\,(I_{n-3} + I_{n+3}) = 0\ , \tag{38}$$

where $M_{1,\,2,\,3}$ are the mutual inductances between two elements separated by one, two and three unit cell sizes, and we have

$$\kappa_{1,\,2,\,3} = \frac{2\,M_{1,\,2,\,3}}{L}\ . \tag{39}$$

From the expression of I_n in Eqn (33), we can deduce that

$$\begin{aligned} I_{n-s} + I_{n+s} &= I_0\,\left(e^{-j(n\,-\,s)kd} + e^{-j(n\,+\,s)\,kd}\right) \\ &= 2I_n\cos\left(skd\right)\ , \end{aligned} \tag{40}$$

where s is an integer. Substituting this relationship into Eqn (38) and dividing both sides by $j\omega L$, we obtain the dispersion relationship

$$\kappa_1\cos(kd) + \kappa_2\cos(2kd) + \kappa_3\cos(3kd) = -\left(1 - \frac{j}{Q}\,\frac{\omega_0}{\omega} - \frac{\omega_0^2}{\omega^2}\right)\ . \tag{41}$$

The attenuation is zero for lossless cases, and the dispersion relationship simplifies to

$$\kappa_1 \cos(\beta d) + \kappa_2 \cos(2\beta d) + \kappa_3 \cos(3\beta d) = -\left(1 - \frac{\omega_0^2}{\omega^2}\right) . \tag{42}$$

For a 1D line that we are interested in, βd is the phase difference between currents in adjacent elements, resulting in a meaningful range of $0 < \beta\, d < \pi$ representing travelling waves. When $\beta d = 0$ or π, all the elements are in phase or in anti-phase, representing evanescent waves that do not propagate along the structure, and these occur beyond the passband of the waveguide. The sharp change of the propagation coefficient with frequency at the band edge in Fig. 2.7 does not have practical meanings as lossless conditions are only ideal. The propagation coefficient is periodic with a period of $\beta d = \pi$ and the dispersion relationship we show in Fig. 2.7 is within the first Brillouin zone [77]. In order to obtain expressions for the frequencies corresponding to the edges of the passband, we equate βd to 0 or π in Eqn (42). For $\beta d = 0$, we have

$$\kappa_1 + \kappa_2 + \kappa_3 = -1 + \frac{\omega_0^2}{\omega_1^2} , \tag{43}$$

where ω_1 is the frequency at one edge of the passband, and the other frequency ω_2 can be found by setting $\beta d = \pi$,

$$-\kappa_1 + \kappa_2 - \kappa_3 = -1 + \frac{\omega_0^2}{\omega_2^2} , \tag{44}$$

and we can combine the results into

$$\omega_{1,\,2} = \frac{\omega_0}{\sqrt{1 \pm \kappa_1 + \kappa_2 \pm \kappa_3}} . \tag{45}$$

The above cut-off frequencies are evaluated under lossless assumptions and with third-order coupling effects taken into account. If only κ_1 is significant and higher order coupling effects are neglected, the results in Eqn (45) simplifies to

$$\omega_{1,\,2} = \frac{\omega_0}{\sqrt{1 \pm \kappa_1}} . \tag{46}$$

So far we have analysed the wave properties of MI wave supported by monoatomic structures with identical meta-atoms as composite unit cells of the MI waveguide. As discussed previously, diatomic lines refer to structures that have two elements per unit cells – we illustrate

a simple case in Fig. 2.8 with identical elements within each cell, but the coupling coefficient between adjacent elements varies, e.g. by varying the relative orientation or separation between them.

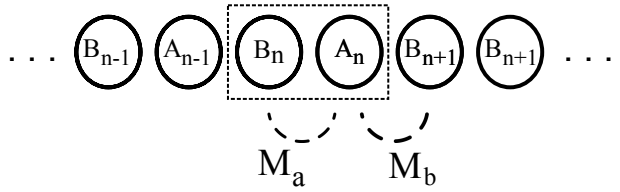


Figure 2.8: Schematic for a model of diatomic structure. The dashed rectangle shows the composite unit cell. For the diatomic configuration, M_a is the mutual magnetic coupling between the two identical resonators A_n and B_n within one unit cell, and M_b is the mutual inductance between adjacent cells, e.g. between element A_n and B_{n+1}.

The current elements A_n and B_n in Fig. 2.8 are

$$\begin{cases} A_n &= A_0\, e^{-jnkd} \\ B_n &= B_0\, e^{-jnkd} \end{cases} , \tag{47}$$

where A_0, B_0 are constants giving the current ratio between elements in the same cell. We denote the mutual inductance between A_n and B_n within the same unit cell as M_a, the mutual inductance between adjacent cells as M_b. We start with a simple case where only nearest-neighbour coupling is significant, and the Kirchhoff's equations for the currents in the array can be written as,

$$\begin{cases} j\omega M_b\, A_{n-1} + j\omega M_a\, A_n + Z_0\, B_n &= 0 \\ j\omega M_a\, B_n + j\omega M_b\, B_{n+1} + Z_0\, A_n &= 0 \end{cases} , \tag{48}$$

where Z_0 is the self-impedance of each resonator in the diatomic array, assumed to be identical for resonators A_n and B_n, giving the ratio between the currents in the same unit cell $B_n\,/\,A_n = B_0\,/A_0$ as

$$\frac{B_0}{A_0} = -\frac{Z_0}{j\omega M_a + j\omega M_b\, e^{-jkd}} , \tag{49}$$

Replacing A_0 or B_0 in Eqn (48) using Eqn (49) gives the dispersion relationship as

$$\cos(kd) = \frac{Z_0^2 + (\omega M_a)^2 + (\omega M_b)^2}{2\,(j\omega M_a)\,(j\omega M_b)} . \tag{50}$$

The dispersion relationships for different cases of M_a and M_b are shown in Fig. 2.9. We define the coupling coefficients as $\kappa_a = 2M_a/L$ and $\kappa_b = 2M_b/L$. The diatomic structure can be seen to exhibit two passbands. When the signs of M_a and M_b are the same (solid curves), the upper branch supports backward waves and the lower branch supports forward waves. However, when they have different signs (dashed curves), the forward waves are supported in the upper branch and backward waves in the lower branch. The attenuation coefficient α is not affected by the change in the sign of coupling. In Fig. 2.9 (a), the coupling strengths are not equal, with $|\kappa_a| = 0.05$ and $|\kappa_b| = 0.13$, which is termed as an unbalanced structure, and there is a stop band near the resonant frequency between the two branches. This stop band is closed up by equating the coupling strengths and creating a balanced line as in Fig. 2.9 (b).

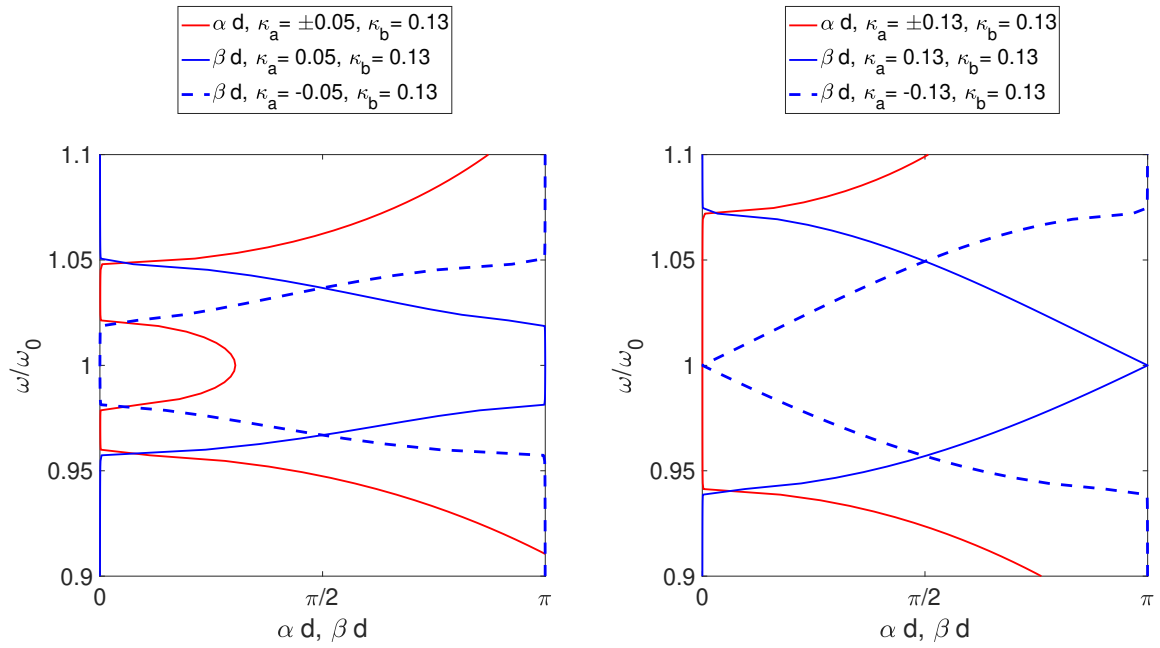


Figure 2.9: Dispersion relationships for diatomic structures based on Eqn (50), αd (attenuation coefficient) is in red, and βd (propagation coefficient) is in blue. (a) is for unbalanced structures with $|M_a| \neq |M_b|$, $|M_a| = 0.05$, $|M_b| = 0.13$. The attenuation curve αd does not change if the sign of M_a is changed. There is a stop band between the two branches shown by βd. (b) is for balanced structures with $|M_a| \neq |M_b| = 0.13$, and the stopband is closed up. When M_a and M_b have the same sign, the upper branch supports backward waves and the lower branch supports forward waves. The nature of the waves are reverted if M_a and M_b have opposite signs, as shown by the dashed blue curves in both (a) and (b).

2.3.3 Near-Field Applications

To distinguish near-field and far-field ranges in optics, diffraction of waves in the near field can be described by Fresnel diffraction [82], whereas the Fraunhofer diffraction refers to far-field diffraction [83]. Analogously, for an antenna, the space surrounding the antenna can be divided into near-field and far-field regions. The boundaries defined for these regions are not rigid as different criteria have been introduced, but some widely accepted ones were discussed in [84]. The far-field region is defined with the distance d from the antenna being [84]

$$d > \frac{2a^2}{\lambda} \ , \tag{51}$$

where a is the largest dimension of the antenna, assuming that a is comparable with the wavelength λ, as is true for most practical antennas to have reasonable radiation resistance, and therein reasonable radiation efficiencies. In the far-field region, the angular field distribution, or the radiation pattern of an antenna, is independent of the distance from the structure [84]. Near fields are defined with

$$0 < d < \frac{2a^2}{\lambda} \ . \tag{52}$$

The size of the meta-atoms, such as the capacitively-loaded SRRs forming MI waveguides, is much smaller than the operational wavelength. One method is to adopt the criterion that for an infinitesimal dipole (with dipole length $l \ll \lambda$), we would reach the near field if [84]

$$kr < 1 \ , \tag{53}$$

where r is the distance from the dipole. The resonant frequencies of the capacitively-loaded SRRs are tuned to lie within the microwave frequency range (around 100 MHz for the structures in Chapter 3 and 4, with wavelength being roughly 3 m). The applications discussed in this section and the ones proposed in Chapter 3 and 4 are based on the signal-guiding properties of the confined MI waves, as well as their interactions with objects in close proximity, therefore being well within the near-field range, which is also termed as the 'subwavelength' (recall that this refers to the dimension of the elements being much smaller than the wavelength) region in the field of metamaterials.

A significant attention in the literature is devoted to the use of MI metamaterials in magnetic

resonance imaging (MRI). Being electrically small, i.e. of much smaller sizes compared to the operational wavelength, resonators that form metamaterial-based structures incur low losses caused by eddy currents as no standing waves can be formed within the resonator. Therefore radio-frequency (RF) heating due to the field produced by the transmit coils [85] in the MRI systems is reduced, making metamaterial-based structures carrying MI waves safe to be implemented in MRI systems. A type of magnetic metamaterial made of hexagonally packed 'Swiss rolls' was studied by Wiltshire et al. [86] for guiding RF flux to MRI receiver coils, thus improving the imaging performance. MI waves travelling in a close circular path were shown to exhibit rotational resonances [87], and consequently the extractable power from a loaded loop within the structure could be raised. The increased signal gain leads to the possibility of applications in MRI systems, for example to improve the imaging quality. The nuclear spins of the imaged body parts absorb and emit RF energy, which is detected by the RF coils in the MRI system. A metamaterial lens reported in [88] manipulated the RF field detected by the receiver coils, so that the sensitivity of these coils was improved, thus improving the spatial resolution of the obtained image. In [89], active components were incorporated, so that the effective permeability of a split ring metamaterial slab could be switched between zero or positive infinity, allowing the slab to reject or confine the RF magnetic field at the operational frequency. This improved the local signal-to-ratio of the surface coils in the MRI system, which led to an improvement of the image quality. Low-loss propagation of MI waves at MRI frequencies over a 2 m-long waveguide was realised using thin-film cables [90]. Incorporating rotatable mechanical hinges between resonators, a flexible MI ring detector was proposed [91]. The first-order coupling between adjacent resonators can be designed to be invariant to relative rotations of the resonators, although variations in higher-order coupling effects can not be compensated, and thus affecting the imaging performance. A novel receiver for internal MRI, constructed from a thin-film MI waveguide mounted on a catheter, was proposed in [92,93]. The magnetically coupled resonators in the waveguide were designed to be decoupled from the applied RF magnetic and electric fields, therefore being safe from undesirable heating effects, and the performance of the structure was shown to be robust against bending effects. Frequency scaling rules are applicable to metamaterial-based structures, and the effectiveness of the catheter-based receiver was demonstrated for both 1 T and 3 T clinical MRI scanners [94]. A structure, constructed from non-magnetic endoscope components combined with a MI waveguide made on a flexible

substrate, designed for MRI purposes was proposed in [95].

Another large area of applications of MI waves is in guiding signals on a subwavelength scale. Metamaterial-based structures have been designed for signal-guiding functions, and near-field directionality can be achieved by controlling the propagation of the supported waves such as SPP or electromagnetic waves. Directional excitation of SPP waves [76] that propagate along the surface of conductors has been realised via chirped plasmonic gratings [96]. In [97], the relative phase and separation between two detuned nanomagnetic antennas were tailored that allowed the travelling SPPs to be steered in a specified direction. In [98], using arrays of metallic slits patterned into a thin gold film, a method to realise tunable directional coupling of SPP waves while preserving their polarisation was presented, where both bidirectional and unidirectional launching of SPPs were discussed. In [99] a method to achieve unidirectional excitation of guided near-field electromagnetic modes through interference of a circularly polarized dipole was discussed. The spin-orbit coupling effect, manifested in the directional scattering of lights with opposite spins using the interaction of SPP waves propagating on a metal interface with nanostructures, was analysed and experimentally demonstrated in [100].

Methods to engineer both far-field and near-field directionality from dipolar structures with phased combinations of electric and magnetic moments were discussed in [101]. Electromagnetic waves can be confined and guided along an infinitesimal interface between complementary impedance surfaces [102]. Selective excitation of the spin-polarized edge mode and therefore the possibility of sending electromagnetic waves to opposite directions along the interface was demonstrated in [103]. One way to create destructive and constructive interference in opposite directions in a two-hole directional coupler waveguide is to launch two signals that are separated by a quarter wavelength in a waveguide.

In Chapter 3, a method to realise controllable unidirectional signal-guiding using a new method based on the near-field interference of propagating MI waves in a 1D waveguide will be demonstrated. We suppressed the MI waves to one end of the line but not the other by exciting two elements with a phase difference applied between them, and the direction of allowed wave propagation depends on the nature of the MI waves, i.e. whether they are forward waves or backward waves. Exciting non-adjacent elements in the MI waveguide created multiple branches within the passband, allowing the travelling of MI waves to alternating directions.

Meta-atoms forming the structures that support MI waves are sensitive to the electromag-

netic fields they are exposed to, and applications based on near-field interactions have been proposed. A 1D contactless data transfer device based on MI waves was reported in [104], where the data capacity was studied both analytically, by modelling using the circuit theory, and experimentally. Extending the 1D analysis to 2D, a surface for wireless data transfer was reported in [105]. MI waveguide structures can be applied for wireless power transfer as well, and the effects of reflections and standing waves, and proper receiver loads for efficient power transfer were discussed in [106].

Practical applications of MI waves, such as microwave filters and delay lines, were suggested by Freire et al. [107] based on a planar 1D array of square split resonators placed between a pair of microstrip lines. The structure supports MI waves and it has the advantage of eliminating the needs for bulky magnets and fragile ferrites as for conventional magnetostatic wave transducers. Compact chipless tags based on similar MI wave delay lines were studied in [108].

Metamaterial-based structures have also been extensively used as sensing devices. As shown in [109], when the slits of the SRRs (symmetric about the gaps) are shifted or rotated relative to symmetry plane of a coplanar waveguide, there is a notch in the the signal transmission S_{21} at the resonant frequency, making the structure useful as alignment or angle sensors. An extended version of the device, with the addition of two resonators, designed for 2D linear displacement sensing was reported in [110, 111]. Microstrip line [112] and coplanar waveguide [113] structures loaded with split resonators were developed as angular displacement and velocity sensors. The principle of operation for these displacement (linear or angular) sensors is that once an SRR is magnetically coupled to the waveguide structure, its excitation is in return affecting the waveguide, thus creating a notch in the transmission coefficient spectrum. The high sensitivity of SRRs to mechanical deformations makes them useful for detecting changes in surface strain of materials [114], with wireless sensors based on a double-SRR structure [115] and on a multiple nested SRR architecture as proposed in [116]. A flexible tape-based substrate was shown to further improve the sensitivity and linearity between the input and output [117] of the sensing devices. The localised electric field near the gap of an SRR makes the resonator sensitive to changes in the dielectric properties of external objects in proximity - its resonant characteristics such as the quality factor Q and resonant frequency f_0 vary. A wireless sensor for monitoring intake of medications based on MI waveguide struc-

tures was reported in [118], and a similar MI sensing module was developed later for detecting the motion of an implanted magnet in the tongue [119], which was developed for people with severe disabilities to have access to utilities through a computer interface.

In [120, 121], the concept of using SRR-based structures for characterisation of chemical and biochemical analytes was discussed. Microfluidic sensors working in the differential mode, based on the variation in the frequency splitting of two SRRs coupled to a transmission line were presented in [122]. Moving to the higher frequency range, microfluidic sensors with THz operational frequencies for trapping and characterising microparticles were discussed in [123]. The sensitivity of the meta-atoms' resonant characteristics makes them useful in other types of sensing functions as well. For instance, local perturbation of the conductivity in a resonator can be sensed in a 1D metamaterial-based structures carrying MI waves [124], and a non-invasive MI waveguide sensor for detecting voids in fiber-reinforced plastics was proposed in [125].

We will present in Chapter 4 a novel possibility to realise position sensing of a conductive object based on measurements of the reflectance from a MI waveguide [126]. The element in the array that is nearest to the object experience a variation in its self-impedance, thus creating a defect in the MI array. The standing waves are formed between the point where we launch the MI waves and the defect, and the resultant reflection spectrum is unique for each defect position. Utilising our knowledge of the MI wave properties, we are able to analytically predict the reflectance and the supported eigenmodes. A localisation algorithm with low computational complexity, for identifying the defect position, is introduced.

2.3.4 Far-Field Applications

As introduced in Section 2.3.1, MI waves have wavelengths much shorter than free space electromagnetic waves of the same frequency. The consequence of this is that a rapid spatial variation in phases of the current distribution can be imposed in metamaterial-based structures that support MI waves. This opens the possibility of creating directive antennas from metamaterial-based structures.

Directivity D is defined as the ratio of the radiation intensity in the direction of maximum radiation from the antenna to the intensity averaged over all directions in the three-dimensional space. Oseen [127] proposed the concept of superdirectivity by referring to the 'Einsteinean needle radiation' which implied that an arbitrarily sharp radiation pattern can be produced an

antenna system of finite size. It was proved by Uzkov [128] that, for an array of N isotropic radiators, the endfire directivity tends to N^2 if the inter-element separation tends to zero. A closed-form expression of the maximum achievable directivity for general linear antenna arrays was derived by Bloch et al. [129]. Following these theoretical studies, the limitations of superdirectivity were addressed by Uzsoky and Solymar [130] who introduced tolerance sensitivity T, quality factor Q, and formulated the maximum directivity with these two factors taken into consideration. Using spherical harmonics, Chu [131], Harrington [132], and Pozar [133] explored superdirectivity. In order to optimise the directivity of superdirective antenna arrays, further theoretical research were conducted in [134–139]. Bacon and Medhurst [140], and Newman and Schrote [141], provided experimental demonstrations of superdirectivity using four-element arrays with one element excited. More recent practical realisations includes arrays comprising two or three electrically small radiators [142–144]. In studying near-field subwavelength imaging, superdirectivity was explored by Ludwig in [145]. There are also related studies on the utilisation of metamaterial-inspired structures to increase the directivity of antennas [146–148]. Our research group has published work on realising superdirecitivity, both analytically and experimentally, by metamaterial-based dimer structures made of two strongly coupled split ring resonators (SRRs) [149–152]

In this thesis, we refer to superdirective structures as radiating structures with directivity D higher than that of a traditional phased array [153] of the same array size. In a phased array composed of N isotropic elements, the elements are excited with controlled phase differences, such that the fields produced by each element add up in phase, resulting in constructive interference in the desired direction of radiation. To excite a linear phased array and to ensure maximum radiation in the endfire direction (along the array axis), with elements spaced equidistantly at a distance d, the neighbouring currents should be excited with a phase shift of kd, with $k = \omega/c$ being the wave number of the electromagnetic radiation.

In contrast to the working principles of phased arrays, superdirectivity relies on destructive interference of the fields from all elements, but least so in the desired direction of radiation. When the distance between elements tends to zero, in order to realise superdirectivity, the required excitations should ensure that the adjacent elements in the array are practically in antiphase [134, 154, 155]. As will be shown by the analytical derivations of maximum achievable directivity below, a superdirective antenna array achieves maximum D when the separation

between two radiators tends to zero, whereas D for a phased array reaches its maximum when the separation is around $0.3\,\lambda$. Therefore, we would effectively realise miniaturisation of the antenna structure while achieving high directivity.

Analytical calculations of the directivity values for an array of two antennas are carried out following the method in [156]. We compare the difference in directivity for a phased array and for a superdirective array. We model an array as two dipoles. A dimer of two dipoles oriented along the z axis, and array axis parallel to the x axis, is the structure under consideration, as illustrated in Fig. 2.10.

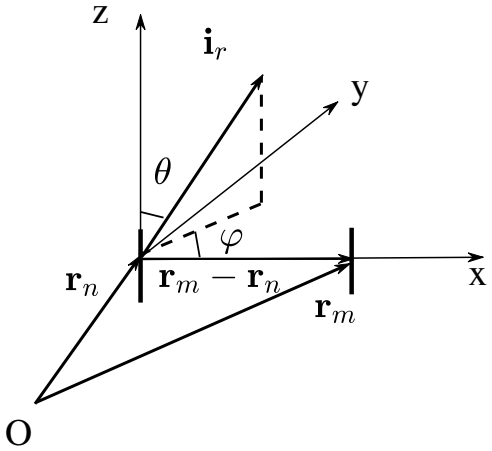


Figure 2.10: The coordinate system for evaluating the radiation pattern from two coupled dipoles oriented in the z direction, and the vector connecting them is $\mathbf{r}_m - \mathbf{r}_n$ which is also the array axis in the x direction. The angle between the radial direction $\mathbf{i}_r$ and the z axis is θ, and φ is between the projection of $\mathbf{i}_r$ onto the yz plane and the x axis.

To characterise the radial direction $\mathbf{i}_r$ in which we determine the radiated power intensity by the dimer, the coordinate system relative to the positions of the two dipoles is shown in Fig. 2.10. The elevation angle θ is the angle between the z axis and $\mathbf{i}_r$, and azimuthal angle φ is the angle between the projection of $\mathbf{i}_r$ onto the xy plane and the y axis. The expression for $\mathbf{i}_r$ is then

$$\mathbf{i}_r = \begin{pmatrix} \sin\theta\cos\varphi \\ \sin\theta\sin\varphi \\ \cos\theta \end{pmatrix} . \tag{54}$$

The inner product of two vectors is defined as

$$\mathbf{ab} = \sum_{n=1}^{2} a_n b_n^* \ . \tag{55}$$

The outer product $\mathbf{a} \circ \mathbf{b}$ generates a matrix c with the components being

$$c_{mn} = a_m b_n^* \ . \tag{56}$$

The resultant vector of the inner product between a matrix c and a vector $\mathbf{b}$ has components

$$a_m = c_{mn} b_n^* \ . \tag{57}$$

Based on these definitions, the far-field electric field strength $\mathbf{E}$ from a dimer of two identical resonators at a separation d along the x axis can be expressed as the inner product of vectors

$$\mathbf{E} = C\,\mathbf{F}\mathbf{I} \ , \tag{58}$$

with a proportionality constant C, with

$$\mathbf{I} = [I_1 \ \ I_2] \tag{59}$$

being the vector of the currents in both element. We also perform the derivation for two isotropic radiators positioned along the x axis separated by d. The following results for the cases with two isotropic radiators and for two dipoles are obtained,

$$\begin{cases} \mathbf{F} = \left[1, \ \ e^{ju\sin\theta\cos\varphi}\right] & \text{(isotropic radiators)} \\ \mathbf{F} = \sin\theta\,\left[1, \ \ e^{ju\sin\theta\cos\varphi}\right] & \text{(dipoles)} \end{cases} , \tag{60}$$

where $u = 2\pi d/\lambda = kd$, gives information about the nature of the resonators - both elements in the dimer are isotropic radiators or dipoles. The power intensity can be written as

$$P_{\mathrm{d}} = \frac{|E|^2}{2Z_0} = \frac{C^2}{2Z_0}\mathbf{I}B\mathbf{I} \ , \tag{61}$$

where matrix B is a result of outer product operation

$$B = \mathbf{F} \circ \mathbf{F} \ . \tag{62}$$

The average power intensity is then

$$\langle P \rangle = \frac{C^2}{2Z_0} \mathbf{I} A \mathbf{I} \ , \tag{63}$$

where the averaging is over the solid angle 4π in 3D space

$$A = \frac{1}{4\pi} \int_0^{2\pi} \int_0^{\pi} B \sin\theta \, d\theta \, d\varphi \ . \tag{64}$$

The results for the integration are summarised below in Eqn (65), with $a = A_{11} = A_{22}$ and $b = A_{12} = A_{21}$ being the components of the matrix A.

$$\begin{cases} a = 1, \ b = \dfrac{\sin u}{u} & \text{(isotropic radiators)} \\ a = \dfrac{2}{3}, \ b = \dfrac{\sin u}{u} + \dfrac{\cos u}{u} - \dfrac{\sin u}{u^3} & \text{(dipoles)} \end{cases} \ , \tag{65}$$

The directivity, defined as the maximum radiation intensity over the average radiated power intensity, is then

$$D = \frac{\mathbf{I} B \mathbf{I}}{\mathbf{I} A \mathbf{I}} \ , \tag{66}$$

where the matrix B is calculated in the $\theta = \pi/2$, $\varphi = 0$ direction, the direction of maximum radiation. The corresponding optimum current distribution is [130]

$$\mathbf{I}_{\text{opt}} = A^{-1} \mathbf{F} \ . \tag{67}$$

The optimum ratio between the currents of the two elements then follows

$$\left(\frac{I_2}{I_1} \right)_{\text{opt}} = \frac{a \, e^{\, ju} - b}{a - b \, e^{\, ju}} \ . \tag{68}$$

The maximum directivity is then

$$D_{\text{opt}} = \mathbf{F} A^{-1} \mathbf{F} \ , \tag{69}$$

and based on Eqn (68), the maximum achievable D for the specified superdirective dimer is

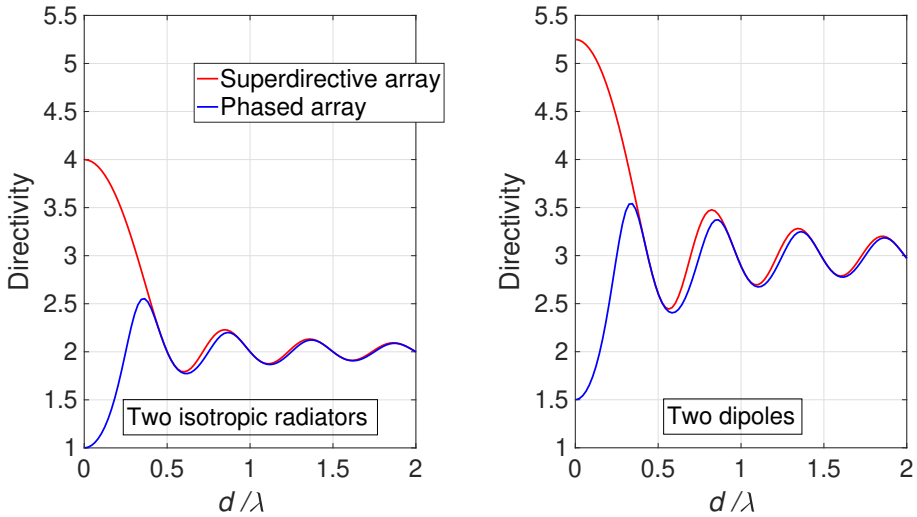


Figure 2.11: Directivity plotted over d/λ where d is the separation between the two elements and λ is the free-space wavelength, for superdirective (red) and phased array (blue) of two coupled isotropic radiators (a) and of two dipoles (b).

$$D_{\text{opt}} = 2\,\frac{a - b\cos u}{a^2 - b^2}\ , \tag{70}$$

with a and b as expressed in Eqn (65).

Based on Eqn (70), the analytical values of the maximum achievable directivity for isotropic and dipole arrays respectively, under superdirective conditions, are plotted (red curves) in Fig. 2.11.

For a phased array of two identical elements, the individually-fed currents in the elements can be written as

$$\mathbf{I} = [1,\ -e^{ju}]\ . \tag{71}$$

The required phase difference between the two currents is dependent on the separation d. Following Eqn (66), without changing the matrices A and B for the specified dimer structures (dipoles or isotropic radiators) and substituting the expression for the current distribution, we obtain the maximum achievable D of a phased array,

$$D = \frac{4}{2\,a + 2\,b\,\cos\,u}\ , \tag{72}$$

where the expressions for a, b follows those in Eqn (65) for the isotropic and dipole arrays respectively. The analytical maximum achievable D of the phased arrays are plotted in blue

for the isotropic case in Fig. 2.11 (a) and for the dipole array in Fig. 2.11 (b). At $d/\lambda \approx 0.3$, corresponding to $u \approx 2$, we obtain the maximum value for a two-element phased array (for both the isotropic and dipole cases). The superdirective array, on the other hand, has its optimum point when $u \to 0$, with the optimum D approaching an ideal value of 4 (isotropic) and 5.25 (dipole). When the relative separation increases and d/λ being above around 0.3, the difference in directivity D becomes very small for a phased array and a superdirective array.

In Chapter 5, dimer structures of two strongly magnetically coupled SRRs that can exhibit superdirectivity are studied. The analytical optimum conditions for superdirectivity are derived for such antenna structures that can be modelled as two coupled magnetic dipoles. In order to avoid lengthy measurements in practical realisations of superdirective dimer antennas, we propose new planar equivalents to the traditional directivity value. The corresponding relationship with the 3D directivity are presented. It is shown that we could optimise the planar directivity defined in the azimuthal plane and the 3D directivity of such superdirective structures simultaneously. This forms a rapid approach to characterise directive antennas that can be modelled as dipoles

3 Controllable Unidirectional Waveguide

As discussed in Section 2.3.1, the propagation of MI waves relies on the magnetic coupling between elements of the structure. By using multiple feeding sources, destructive and constructive interference of MI waves can be created that results in suppression of the waves travelling in a required direction.

In this chapter, we derive universal rules for controllable unidirectional propagation for two closely positioned sources that yield near-field interference of MI waves [157]. Analytical predictions for MI waveguides operating in the microwave frequency range are verified by experimental results. We propose a fundamental rule that the selective signal-guiding phenomenon is determined by the forward or backward nature of the waves supported. The same effect of direction selectivity is demonstrated, based on analytical and numerical calculations, for nanostructured arrays with purely electric coupling between the elements where electroinductive (EI) waves are supported. We then continue to the cases where the sources are separated by two cells. There is a split in the passband, with MI waves travelling in opposite directions for the two bands. We treat this system as a degenerate case of diatomic structures with dual dispersion branches featuring both forward and backward waves. Analytical and experimental demonstrations for this case are presented.

3.1 Theory for Unidirectional Propagation

In some cases, it may be preferable to direct signals in a MI waveguide to only one direction, addressing one of two possible receiver positions. It is possible to suppress the wave propagation to one end but not the other by applying two excitations near the centre of the array.

In a linear array of N identical elements, numbered from left to right, elements p and $p+n$ near the centre are excited, with sources of the same amplitude (amplitude $= 1$) but with a phase difference (φ, the excitation at p is $V_p = \mathrm{e}^{j\varphi}$ and that at $p+n$ is $V_{p+1} = 1$). If we consider the currents in two elements s and t that are on opposite sides of the excited elements, i.e. $s < p$ and $t > p+n$, the expressions for the currents I_s, I_t can be found based on superposition of

the waves launched from p and $p+n$, neglecting any reflections from the array ends,

$$\begin{cases} I_s = e^{j\varphi}\, e^{-j(p-s)kd} + e^{-j(p+n-s)kd} \\ I_t = e^{j\varphi}\, e^{-j(t-p)kd} + e^{-j(t-p-n)kd} \end{cases}, \tag{73}$$

or in the form

$$\begin{cases} I_s = e^{-j(p-s)kd}\left(e^{j\varphi} + e^{-jnkd}\right) \\ I_t = e^{-j(t-p)kd}\left(e^{j\varphi} + e^{jnkd}\right) \end{cases}, \tag{74}$$

where $k = \beta - j\alpha$ is the complex wave number of the MI wave as discussed in Chapter 2, and d is the lattice period of the array. It is assumed that reflections from the ends are neglected. The ratio between the power to the left and the power to the right is

$$\begin{aligned} \frac{P_s}{P_t} &= \frac{|I_s|^2}{|I_t|^2} \\ &= \frac{|e^{j\varphi} + e^{-jnkd}|^2}{|e^{j\varphi} + e^{jnkd}|^2}\, e^{2(s+t-2p)\alpha d}. \end{aligned} \tag{75}$$

Under lossless assumptions, $\alpha \approx 0$, and Eqn (75) becomes

$$\begin{aligned} \frac{P_s}{P_t} &\approx \frac{|e^{j\varphi} + e^{-jn\beta d}|^2}{|e^{j\varphi} + e^{jn\beta d}|^2} \\ &= \frac{|\cos\varphi + j\,\sin\varphi + \cos(n\beta d) - j\sin(n\beta d)|^2}{|\cos\varphi + j\,\sin\varphi + \cos(n\beta d) + j\sin(n\beta d)|^2} \\ &= \frac{2 + 2\,\cos\varphi\,\cos(n\beta d) - 2\,\sin\varphi\,\sin(n\beta d)}{2 + 2\,\cos\varphi\,\cos(n\beta d) + 2\,\sin\varphi\,\sin(n\beta d)} \\ &= \frac{1 + \cos(\varphi + n\,\beta\,d)}{1 + \cos(\varphi - n\,\beta\,d)}. \end{aligned} \tag{76}$$

It can be easily deduced that the power ratio is frequency dependent, based on the dispersion relationship $\omega - \beta$ from Eqn (80) under lossless assumptions. Taking $n = 1$, the dependence of the power ratio over the phase angle between sources φ and the frequency ω is plotted for both forward and backward waves, by setting $\kappa = \pm 0.13$. The logarithmic quantity $\log_{10}(P_s\,/\,P_t)$ is plotted as the contour maps in Fig. 3.1.

Figure 3.1 (a) and (b) are based on Eqn (76), under lossless conditions. Figure 3.1 (a) is

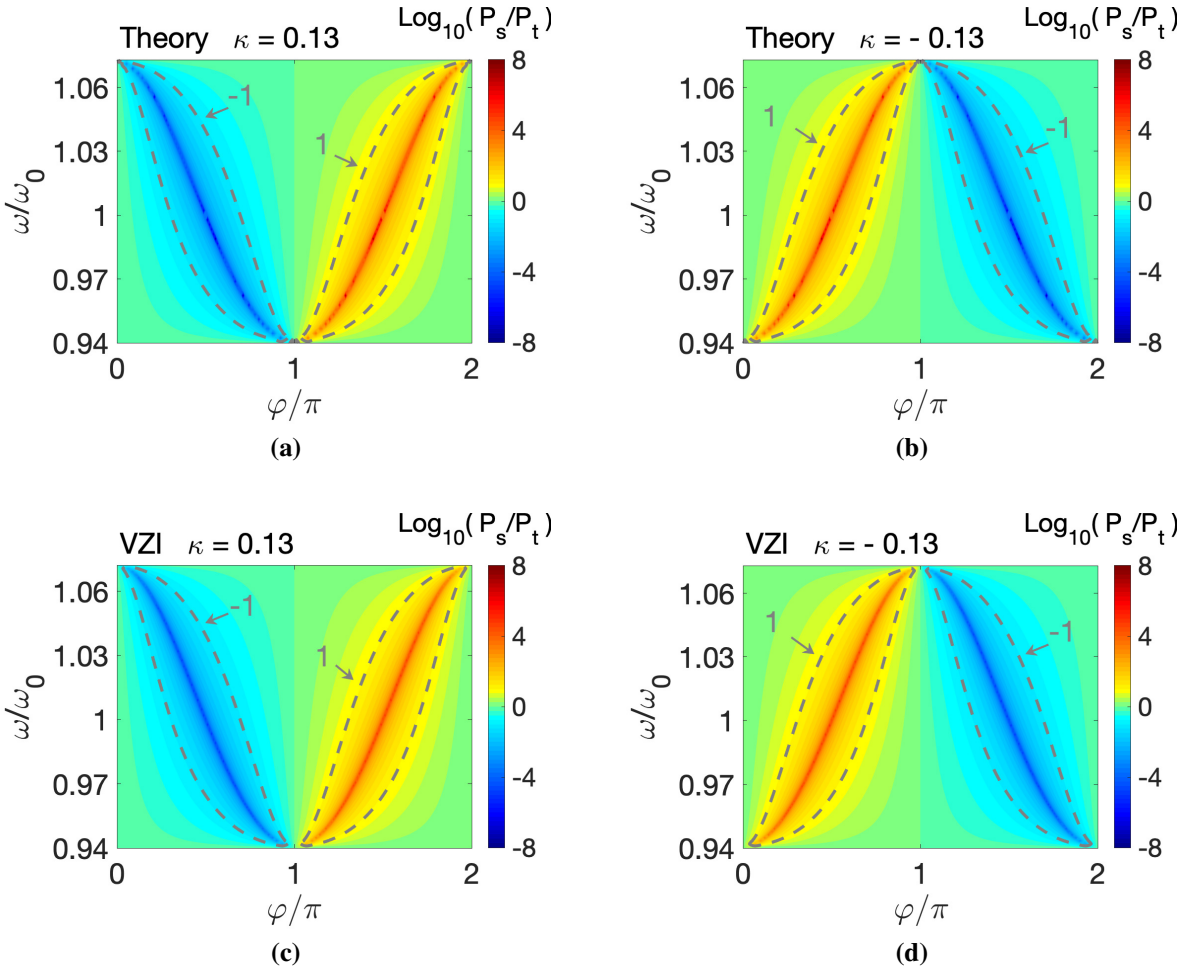


Figure 3.1: Analytically calculated ratio between the power evaluated at element s (to the left of the sources) and that at element t (to the right of the sources), $P_s\,/\,P_t$. The $\log_{10}\left(P_s\,/\,P_t\right)$ is plotted as a contour plot, the horizontal axis is the phase difference φ between the two adjacent sources divided by π, and the vertical axis is the frequency ω. (a) and (b) are based on Eqn (76) with lossless conditions, taking $n = 1$. The dispersion relationship $\omega\,(\beta)$ follows Eqn (36) in Section 2.3.2. In (a) $\kappa = 0.13$ is used, and (b) $\kappa = -0.13$. (c) and (d) are from the 'V = ZI' calculation (discussed in Section 2.3.2) for 26-element arrays, with elements 13 and 14 at the center being excited, the source applied to element 13 leads that applied to element 14 by φ. The power ratio is obtained for $s = 1$, $t = 26$. Ideal matching terminations of $Z_{\mathrm{T}} = j\omega M\, e^{-jkd}$ are applied to both ends of the modelled arrays to remove reflections. The loss is set to be very low, with $R = 0.01\,\Omega$, to approximate the lossless assumption in Eqn (76). (c) is for $\kappa = 0.13$ and (d) is for $\kappa = -0.13$.

for a structure supporting forward waves with $\kappa = 0.13$ and Fig. 3.1 (b) is for one supporting backward waves with $\kappa = -0.13$. Only first-order coupling effects were considered as demonstrations, but higher-order couplings will be taken into account in the next section for analysing the waveguide we used. The passband shown for both cases agrees with what we predicted in Eqn (46), with ω/ω_0 in the range of 0.94 to 1.07.

Figure 3.1 (c) and (d) are from the 'V = ZI' impedance matrix calculation, an analytical

modelling method discussed in Section 2.3.1, with very low loss, $R = 0.01\,\Omega$, set for each of the 26 elements in the arrays. Elements 13 and 14 at the centre are excited with the external signal applied to element 13 leading that in element 14 by φ. Matching terminating loads Z_{T} from Eqn (17) are applied to both ends of the modelled arrays to remove the reflections that would otherwise be strong for such low-loss short arrays. The power ratio is calculated based on the currents in element 1 and 26,

$$\frac{P_s}{P_t} = \frac{|I_1|^2}{|I_{26}|^2} \tag{77}$$

for both $\kappa = 0.13$ [Fig. 3.1 (c)] and $\kappa = -0.13$ [Fig. 3.1 (d)]. For both cases, the results from 'V = ZI' calculations are nearly identical to those from Eqn (76), justifying the closed-form expression of Eqn (76).

It should be noted that under the lossless assumptions in Figs. 3.1 (a) and (b) at $\omega = \omega_0$, we have obtained singularity points with $P_s/P_t = 0$ or ∞ at $\varphi = \pi/2$ or $3\pi/2$, with the corresponding value of power ratio determined by the sign of the coupling coefficient. (For example, Fig. 3.1 (a) with $\kappa = 0.13$ has $P_s/P_t = 0$ at $\varphi = \pi/2$.) These points represent complete suppression of signals either to the left or to the right. At these points, taking the logarithmic values gave us $\pm\infty$, and these singularity points were smoothed out in the colormaps by setting the limits of the colormap range to $\pm 10^8$. However, these singularity points did not concern us since lossless conditions can not be realised in practice, and such discontinuities disappeared for the low-loss cases we modelled in the 'V = ZI' analytical calculations of Figs. 3.1 (c) and (d).

The negative values shown by the blue (cold) colors in the colormaps indicates that the power to the left is lower than that transferred to the right, i.e. the signal propagation to the left is suppressed, and the red (warm) colors correspond to the case in which the signal propagation to the right is suppressed. Figures 3.1 (a) and (c) show that $0 < \varphi < \pi$ results in signal suppression to the left for the forward waves, and when $\pi < \varphi < 2\,\pi$ the signal to the opposite direction is suppressed. It can be seen from Figs. 3.1 (b) and (d) that the directions of wave propagation are reversed for the structure supporting backward MI waves for the entire range of the phase shift values. Therefore, we would expect a change in the sign of κ to result in a reverted direction of the allowed signals in a MI waveguide. In other words, our model leads to an important conclusion - the nature of the MI waves, being forward or backward waves,

determines the direction of signal propagation.

The dashed contour lines in Fig. 3.1 mark the values of the power ratio corresponding to $P_s/P_t = 1/10$ or 10. Based on the range of ω enclosed by the contour lines for each φ value, the frequency bandwidth, within which the signal suppression to either direction works well, is the widest at $\varphi = \pi/2$ or $\varphi = 3\pi/2$, both for forward and backward waves.

Our approach is to set $\varphi = \pi/2$, i.e. the source at element p leads the other source at $p + n$ by $\pi/2$. Generally we evaluate the ratio between the power at elements that are separated by the same distance from the excited elements, therefore $s + t = 2p + n$. Substituting the value of $\varphi = \pi/2$ in Eqn (76), we obtain

$$\frac{P_s}{P_t} \approx \frac{1 - \sin(n\beta d)}{1 + \sin(n\beta d)} \quad . \tag{78}$$

To excite adjacent elements, we set $n = 1$. In this simple case, when $\sin(\beta d) > 0$, which is true for forward waves supported by MI waveguides with positive coupling between adjacent cells, the power transmitted to the left is less than the power transmitted to the right within the entire passband. For backward waves supported by the MI arrays, with negative coupling between cells, the waves travelling to the right are suppressed within the entire passband.

There are two general observations based on Eqn (78). The first one is that when the distance between the excited elements is n lattice periods, the passband of the structure is divided into n frequency ranges, in which signals could travel in opposite directions as we move from one frequency range to another. Furthermore, changing the sign of the coupling coefficient only changes the wave propagation direction if n is an odd number. This will be discussed further in Section 3.2 and Section 3.3.

3.2 Adjacent Excitations

3.2.1 MHz Arrays

The analytical model of the waveguide structure is based on the circuit theory, where the elements are modelled as coupled LCR circuits, and the sources used to inject signals are approximated as point sources. In the microwave regime, small loop antennas act as source loops that can induce signals at specified locations when placed next to elements in the MI waveguides,

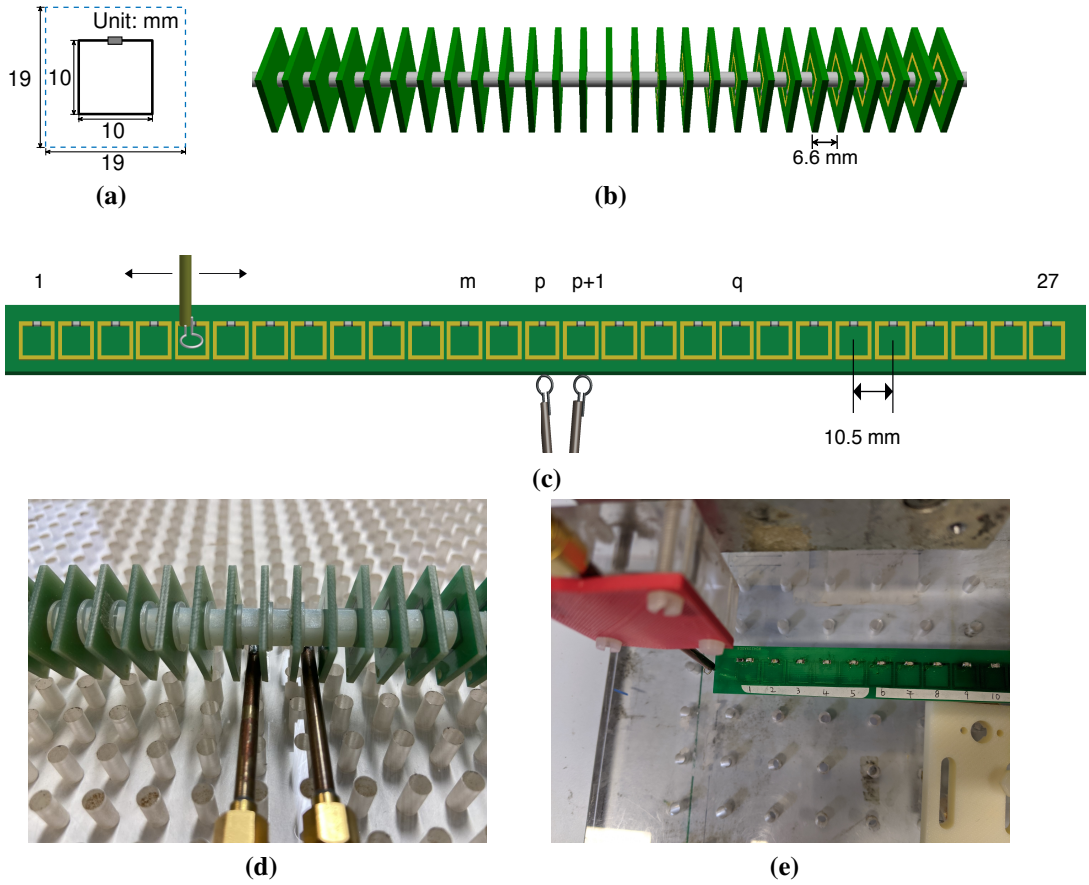


Figure 3.2: (a) The composite meta-atom of the MI waveguide is a PCB square split resonator, and its dimensions are shown. The side-length is 10 mm, and the FR4 substrate size (only for the axial configuration) is 19×19 mm. (b) is an axial array, with a period of 6.6 mm. (c) is a planar array, with the period being 10.5 mm. It is shown schematically that, with 27 elements in the array (element 1 on the left, and element 27 on the right), there are magnetic loop antennas under element 14 and 15 to excite the array in the experiments, and the receiving antenna is moved across the structure. (d) is a photo of the axial array used in the experiments, with two magnetic loop antennas placed in close proximity to the elements, demonstrating how we excited the elements. (e) is a photograph of the planar structure, showing also the receiving loop antenna moved above the array.

and therefore the approximation for the point-source excitation is valid. Consequently, experimental validation of our proposed method for controlling wave propagation is carried out in the MHz frequency range.

Two types of arrays containing 27 strongly coupled resonators were studied, both made up of identical elements. Each unit cell, as shown in Fig. 3.2 (a), is a PCB-based square resonator of 10 mm sidelength, 1 mm track width, made of 1 oz copper, and has a 100 pF capacitor soldered into a 1 mm gap to tune the resonant frequency to $f_0 = 116.6$ MHz. The substrate is 1.6 mm FR4 TG130. The substrate size for the unit cells in the axial array is 19 mm $\times$ 19 mm, and the measured quality factor for a single element is $Q \approx 80$.

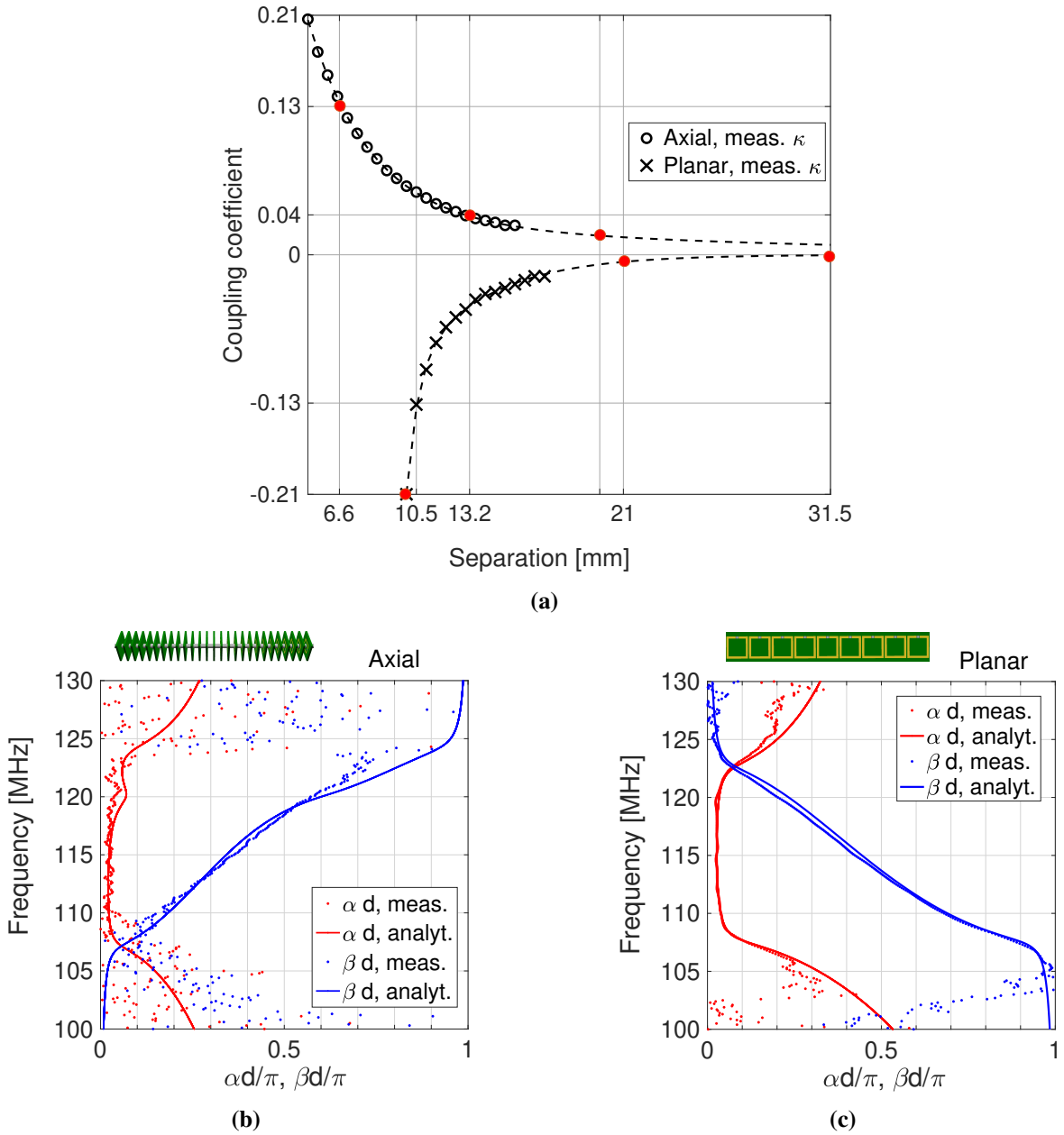


Figure 3.3: (a) Measured coupling coefficients $\kappa = 2M/L$ between two coupled square SRRs versus the separation between them. The circles and crosses are the measured κ for the axial and planar pairs respectively. The dashed curves are the fitted values. The lattice period in our axial array is 6.6 mm. The nearest neighbour coupling is $\kappa_1 = 0.13$, the second-order coupling is $\kappa_2 = 0.034$, and the third-order coupling is $\kappa_3 = 0.017$, marked by the red dots. For the planar array we studied, the lattice period is taken as 10.5 mm, with $\kappa_1 = -0.13$, $\kappa_2 = -0.0062$ and $\kappa_3 = -4.3 \cdot 10^{-4}$ from the fitting. (b) and (c) are the dispersion curves for the axial and planar arrays. The frequency dependences of αd (red dots) and βd (blue dots) are extracted from experimental current distributions among the elements in the structures. The solid curves are the dispersion relationships from analytical calculations based on Eqn (80), using corresponding experimental values of coupling coefficients from (a). The fitted resonant frequencies used for analytical calculations are 116.6 MHz (axial array), and 114.1 MHz (planar array).

Two configurations (the axial and the planar ones) were studied, as illustrated in Fig. 3.2. For the axial array of Fig. 3.2 (b), the axially aligned elements are orthogonal to the array axis,

and for the planar array of Fig. 3.2 (c), the elements lie in the same plane. The photos taken for the structures that we used in experiments are shown in Fig. 3.2 (d) (axial array) and Fig. 3.2 (e) (planar array). The strength of the mutual coupling between adjacent unit cells depends on the separation between them. As explained in Section 2.2, magnetic coupling is the dominant coupling mechanism for capacitively-loaded SRRs, and the expression for the magnetic coupling coefficient from Eqn (4) is restated here

$$\kappa = \frac{2M}{L} \ . \tag{79}$$

The measured variations in the coupling coefficient κ with the separation between elements, for both axial and planar cases, are shown in Fig. 3.3 (a). The dashed curves are fitted values to the measured data. The method to obtain experimental values of the coupling coefficients was described in [57].

The lattice periods for both configurations were chosen so that the nearest-neighbour coupling coefficients are equal in magnitude in both arrays. The lattice period d for the axial array is 6.6 mm, with the nearest-neighbour coupling coefficient $\kappa_1 = 0.13$, second-order coupling coefficient $\kappa_2 = 0.034$, and third-order coupling coefficient $\kappa_3 = 0.017$. As for the planar array, $d = 10.5$ mm, giving $\kappa_1 = -0.13$, $\kappa_2 = -0.0062$, and $\kappa_3 = -4.3 \cdot 10^{-4}$.

The axial array supports forward MI waves as confirmed by the dispersion curves are shown in Fig. 3.3 (b). The analytical dispersion relationship taking up to the third-order coupling into account given by Eqn (41) can be written in the following form [63]:

$$\sum_{n=1}^{3} \kappa_n \cos(nkd) = \frac{\omega_0^2}{\omega^2} - 1 + \frac{j}{Q}\frac{\omega_0}{\omega} \ . \tag{80}$$

An odd number of coupling coefficients should be taken into account, as explained in the Appendix (Section 7.1). Using Chebyshev polynomials we rewrite the dispersion as a polynomial of the third-order. The solution to the dispersion relationships gives us three modes. As shown in Appendix 7.1, one of these modes is the dominant mode, with the other two being highly attenuated complex modes. The analytical dispersion for the dominant mode is shown in Figs. 3.3 (b) and (c). As far as the experimental dispersion is concerned, we have extracted it using a technique developed in [2] which assumed a single-wave propagation, based on the

currents in three adjacent elements,

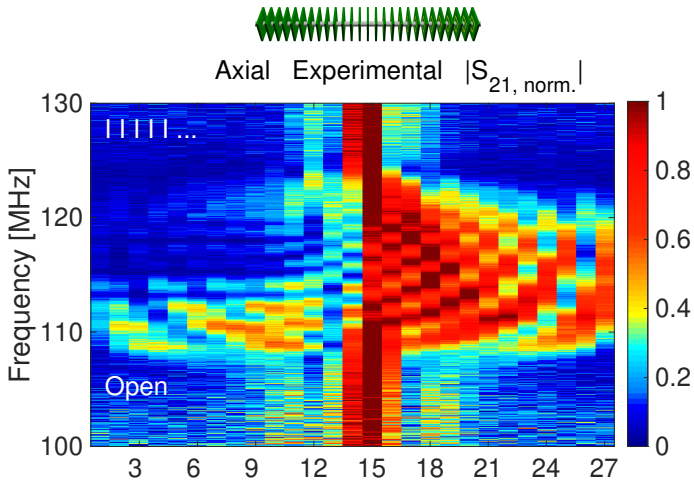
$$kd = \cos^{-1}\left(\frac{I_{n-1} + I_{n+1}}{2\,I_n}\right) \ . \tag{81}$$

For the axial array the method is slightly less reliable towards the upper edge of the passband, namely in the range of frequencies where the attenuation of the dominant mode increases so much that the secondary modes come into play. Within the main part of the passband, this extraction method provides us with results that can be seen to agree with analytical predictions. In the planar array, where secondary coupling effect is very weak altogether, the single-mode assumption is justified as can be seen in Fig. 3.3 (c) – there is remarkable agreement between the analytical and experimental results.

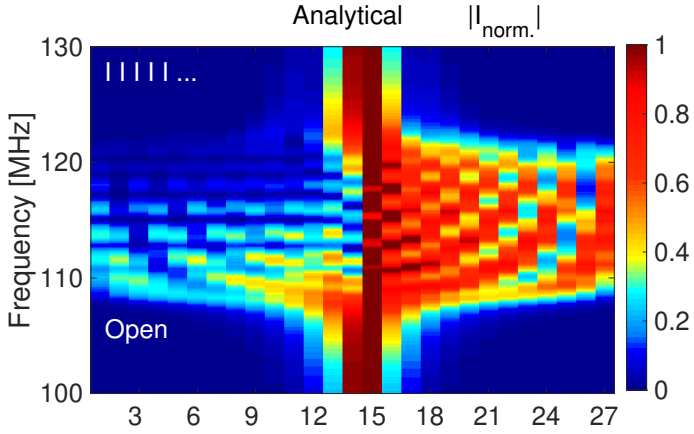
The non-negligible third-order couplings leads to a turning point in the attenuation curve at around 120 MHz, as seen from the experimental results. The higher-order couplings also result in a shifted passband for the axial array. With only κ_1 taken into account, the cut-off frequencies of the waveguide (with $f_0 = 116.6\,$MHz for the elements) would be around 109.7 and 125 MHz, from Eqn (46). Taking into account $\kappa_{1,\,2,\,3}$, the cut-off frequencies became 107.3 and 123.8 MHz from Eqn (45), which can also be deduced from the dispersion relationship in Fig. 3.3 (b). Positive higher-order coupling coefficients $\kappa_{2,\,3}$ of the axial structure lead to a shift in the pass-band to lower frequencies. Another effect of the higher-order coupling coefficients is that the attenuation (α) becomes less symmetrical about f_0 – it is slightly higher at higher frequencies within the pass-band [63].

The resonant frequency of the square SRR in the planar array is $f_0 = 114.1\,$MHz, lower than $f_0 = 116.6\,$MHz of the single element in the axial array, due to the presence of adjacent metal elements and the difference in the size of the substrate. The dispersion curves for the planar array shown in Fig. 3.3 (c) are more straightforward since the higher-order coupling coefficients are relatively weak compared to those of the axial array. The structure supports backward waves as expected, and the bandwidth is well predicted by the analytical expression.

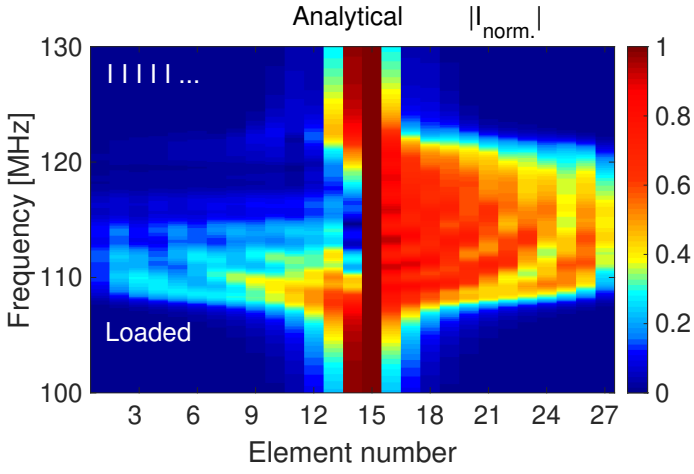
Exciting just a single central element of a symmetrical waveguide structure would obviously result in a symmetrical signal propagation to both ends. Following Eqn (76), we can control the direction of wave propagation by applying voltages with a $\pi/2$ phase difference, two adjacent elements near the centre of a 27-cell array. Structures that support forward and backward waves



(a)



(b)



(c)

Figure 3.4: The current distribution in the 27 elements of the MI waveguides over frequency for an axial array. For (a) and (b), both ends of the array are open, i.e. unloaded. In each plot, the magnitudes of the current are normalised to the maximum value at each frequency. (a) is the experimental S_{21} with the receiving loop antenna moved parallel to the array axis, the signal is picked up at 6 mm from the side of each element. (b) is the analytically calculated normalised current over frequency in each resonator. (c) is the analytical current distribution assuming that both ends of the array are loaded with resistors of 1 Ω.

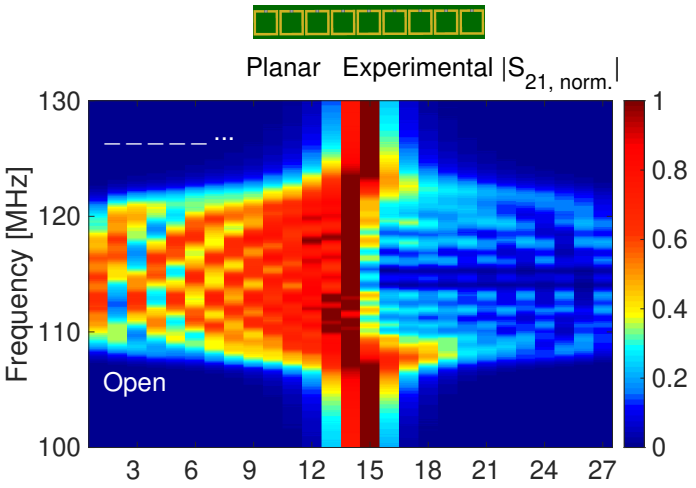


Figure 3.5: The current distribution in the 27 elements of the MI waveguides over frequency for a planar array. In each plot, the magnitudes of the signal are normalised to the maximum value at each frequency. In (a) and (b), both ends of the arrays are open. (a) is the experimental S_{21} with the receiving loop antenna moved parallel to the array axis, the signal is picked up at 2 mm from the surface of each element. (b) is the analytical current over frequency in each resonator. (c) is the analytically calculated current distribution assuming that both ends of the array are loaded with resistors of 0.9 Ω.

give opposite unidirectional propagation under the same excitation conditions as discussed in the previous section. To verify the proposed method of controlling the wave propagation, we carried out the following experiments.

Two source loop antennas (of 4 mm diameter) were connected to the two outputs of a hybrid $\pi/2$ power splitter (Mini-Circuits, ZMSCQ-2-120+), which was then connected to a Vector Network Analyser (VNA). Element 14 and 15 were excited by placing the source loops next to the elements, and the signal in element 14 lead that in element 15 by $\pi/2$. An identical receiving antenna connected to the VNA was moved along the array to detect the magnetic flux generated by each element, by measuring the scattering parameter S_{21} of the system. The magnitude of S_{21}, normalised to its maximum value among all the elements at each frequency, is shown in Fig. 3.4 (a) and Fig. 3.5 (a), for the axial and planar structure, respectively. The measured S_{21} with the receiving antenna next to the cell centres, at an unchanged distance, is proportional to the normal component of the generated magnetic field, and is therefore assumed to be proportional to the current in each element [57]. In order to compare the measured and the analytical distributions, the analytical normalised current distributions, using the measured array parameters listed, are shown in Fig. 3.4 (b) and Fig. 3.5 (b) for the axial and planar arrays.

As follows from Fig. 3.4 and Fig. 3.5, the switchable directional propagation was demonstrated and the experimental data agree well with the analytical results. For the axial structure, the signals at frequencies near the upper cut-off frequency are more attenuated, while some power is leaking to the left of the axial array at lower frequencies, both seen in the measured and analytical results. This can be attributed to the non-negligible higher-order coupling effects in the structure. The signal for the planar configuration is more symmetrical about the middle of the passband. Within around two-thirds of the passband, centred around the mid-frequency, the power flow to one end is five times higher than the power flow to the opposite end for both the axial and planar configurations.

Reflections from the ends of the array are indicated by the standing wave patterns seen as ripples in contour plots of Fig. 3.4 (a) and Fig. 3.5 (a). One way to reduce reflections would be to add matching impedances to both ends. For a MI waveguide with non-negligible higher-order

couplings, the matching terminating impedance Z_{T} is

$$Z_{\mathrm{T}} = \sum_{n=1}^{3} j\omega M_n \, e^{-jnkd} \ , \tag{82}$$

where M_n is the mutual inductance between two elements separated by n unit cells. Away from the resonant frequency, the matching impedance Z_{T} is a complex number and is frequency dependent [158]. At the resonant frequency, Z_{T} is nearly a real number and could be added as a resistor in practice. For the planar array we studied, $Z_{\mathrm{T}} = 0.9\,\Omega$, and for the axial array it is $1\,\Omega$. The aim of the study in this chapter is to demonstrate the possibility of controllable signal-guiding in MI waveguides, therefore results with the terminating impedances are based on analytical calculations only.

Figure 3.4 (c) and Fig. 3.5 (c) are the analytical current distributions over frequency if the ends of the arrays are loaded with resistors of the calculated values above. For both cases, the standing waves arising from reflections become much weaker when the array ends are loaded, but they are not eliminated since the terminating resistance is only a matching value at the resonant frequency.

The suppression of travelling waves to one end works well over a wide frequency band, and we defined a frequency of optimum suppression based on the ratio between the currents in element s and element t, on opposite sides of the excited elements 14 and 15. We chose $s = 12$ and $t = 17$ so that the two elements were of equal distance (two lattice periods) to the sources. The defined optimum frequencies based on the analytical calculations, along with some other quantities of interest, are summarised in Table 1.

MHz Arrays	Axial [MHz]	Planar [MHz]
Resonant frequency, f_0	116.6	114.1
Frequency of $\beta\, d = \pi/2$, f_{fit}	119.0	113.6
Optimum frequency for an open array, $f_{\text{opt, open}}$	119.1	113.1
Optimum frequency for a loaded array, $f_{\text{opt, loaded}}$	119.8	113.8

Table 1: Key frequencies based on analytical results for the MHz axial and planar waveguides.

We analytically calculated the component of the magnetic field normal to the elements, and the results are shown in Fig. 3.6. The analytical model for field calculation is based on filament

current approximations to the resonators, and is described in Appendix (Section 7.2). The distance between the plane of evaluation and the waveguide is different for the axial array (6 mm) and the planar array (2 mm). These values are taken to match the experimental conditions of measurements. We show the field patterns at the corresponding optimum frequencies of the structures. These optimum frequencies are different for the open-end arrays and the loaded arrays, since the matching loads added to the ends of the arrays would result in reduced MI wave reflections and therefore weaker standing wave patterns.

For the axial array, the analytical field distribution at $f_{\text{opt, open}} = 119.1\,\text{MHz}$ is shown in Fig. 3.6 (a). The optimum frequency of the axial array with open ends is higher than the f_0 due to the higher-order coupling effects, and it is very close to the $f_{\text{fit}} \approx 119\,\text{MHz}$ (corresponding to $\beta\, d = \pi/2$ from Fig. 3.3 (b), at which frequency one might expect the suppression to work best). To the left of the excited elements, the analytically calculated magnetic field is close to zero. Standing waves are formed on the right hand side due to reflections from the end. $|H_x|$ reaches local minima next to the track of each element, and local minima occur near the middle of two adjacent elements. If $1\,\Omega$ resistors are added to both ends of the array, the reflections are significantly reduced. The optimum frequency is $f_{\text{opt, loaded}} = 119.8\,\text{MHz}$ for this terminated array. Figure 3.6 (b) is the calculated field distribution in the same plane of evaluation at $f_{\text{opt, loaded}}$ for the terminated axial array. The calculated local minima of $|H_x|$ next to each element decreases monotonically moving away from the excited element 15.

Similar conclusions were drawn by analysing the magnetic field produced by a planar array. The plane of field evaluation was 2 mm from the surface of the array. The optimum frequency is $f_{\text{opt, loaded}} = 113.1\,\text{MHz}$ for the planar array with no terminations. The $f_{\text{opt, open}}$ is slightly lower than the f_0 of 114.1 MHz which can be attributed to the standing wave modes formed. At $f_{\text{opt, loaded}}$, the signals propagating to the left are cancelled to the maximum extent, as shown in Fig. 3.6 (c). The calculated magnetic field reaches local minima between adjacent elements. The distribution of the field above the element centres demonstrates the standing waves patterns. If $0.9\,\Omega$ resistors are added to the ends of the array, the calculated optimum frequency $f_{\text{opt, loaded}}$ is even closer to the f_0, as expected from Eqn (76). The resultant field distribution for a terminated planar array at $f_{\text{opt, loaded}} = 113.8\,\text{MHz}$ is shown in Fig. 3.6 (d).

As predicted analytically and verified by experimental results, controlled unidirectional propagation was achieved for both the axial and planar MHz structures using our proposed

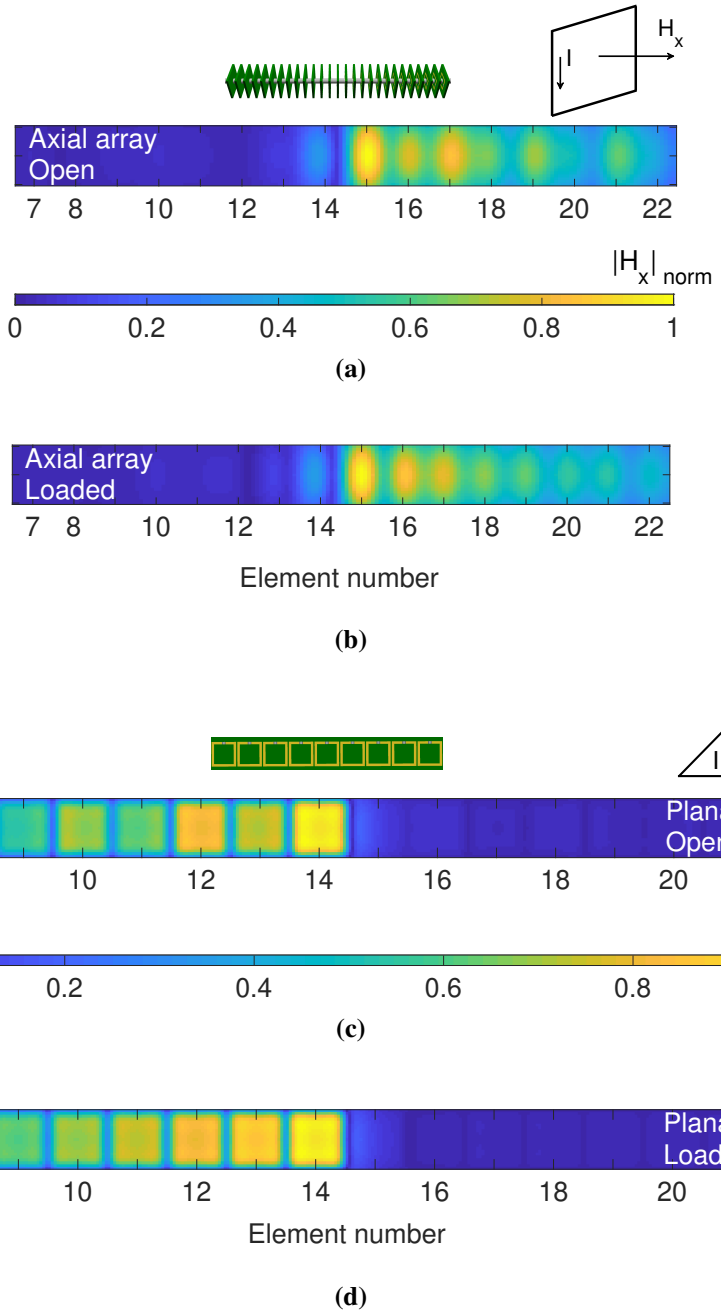
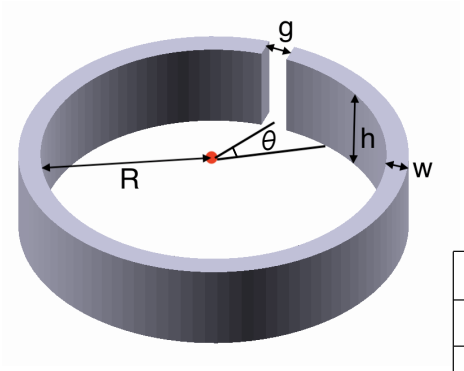


Figure 3.6: Analytical magnetic field distribution based on analytically calculated current distributions. The magnetic field component normal to the resonators is shown. For the 27-element arrays, elements 14 and 15 are excited with a phase difference of $\pi/2$. (a) and (b) are for an axial array. The $|H_x|$ produced by an axial array is plotted in a plane 6 mm from the side of each resonator. (a) is for an open array with no terminations, at the optimum frequency of $f_{\text{opt, open}} = 119.1\,\text{MHz}$. Standing waves are formed, and the waves travelling to the left are almost completely suppressed. (b) is for an axial array loaded with $1\,\Omega$ resistors at both ends, at the calculated $f_{\text{opt, load}} = 119.8\,\text{MHz}$. There is less reflection and less standing waves formed compared to that shown in (a). (c) and (d) are the calculated $|H_z|$ in a plane 2 mm above a planar array. (c) is for an open array, at $f_{\text{opt, open}} = 113.1\,\text{MHz}$. (d) is for an array loaded with $0.9\,\Omega$ resistors at both ends. The field is evaluated at the $f_{\text{opt, loaded}} = 113.8\,\text{MHz}$.

method of exciting two elements with signals of a $\pi/2$ phase difference. Analytical calculations predicted that reflections can be reduced if terminating resistors are added to the ends

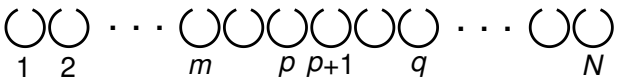
of the waveguides, which may be implemented for future experimental studies. The sign of the coupling coefficient between adjacent unit cells determines the nature of the supported MI waves travelling in the waveguide, which then determines the direction of allowed propagation of MI waves in the arrays if the excitation conditions are kept the same.

3.2.2 THz Arrays

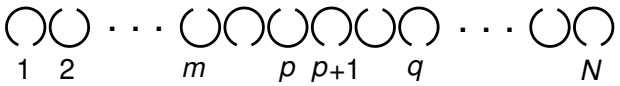


R	80 nm
g	12 nm
h	40 nm
w	8 nm

(a)



(b)



(c)

Figure 3.7: Schematic for (a) a single SRR element with inner radius R, width w, height h, and gap g, θ is the azimuthal angle used for current and charge distribution calculations. (b) a linear 'uu' array, which has positive coupling between adjacent elements and (c) a 'un' array which has negative first-order coupling.

Due to the scalability of MI waveguides, we expect our proposed method of controlling the wave propagations to work in higher frequency ranges as well. Numerical calculations on arrays with operating frequencies in the THz regime were carried out. For practical realisation, one could use fluorescent molecules and nanoparticles to approximate point sources at 100

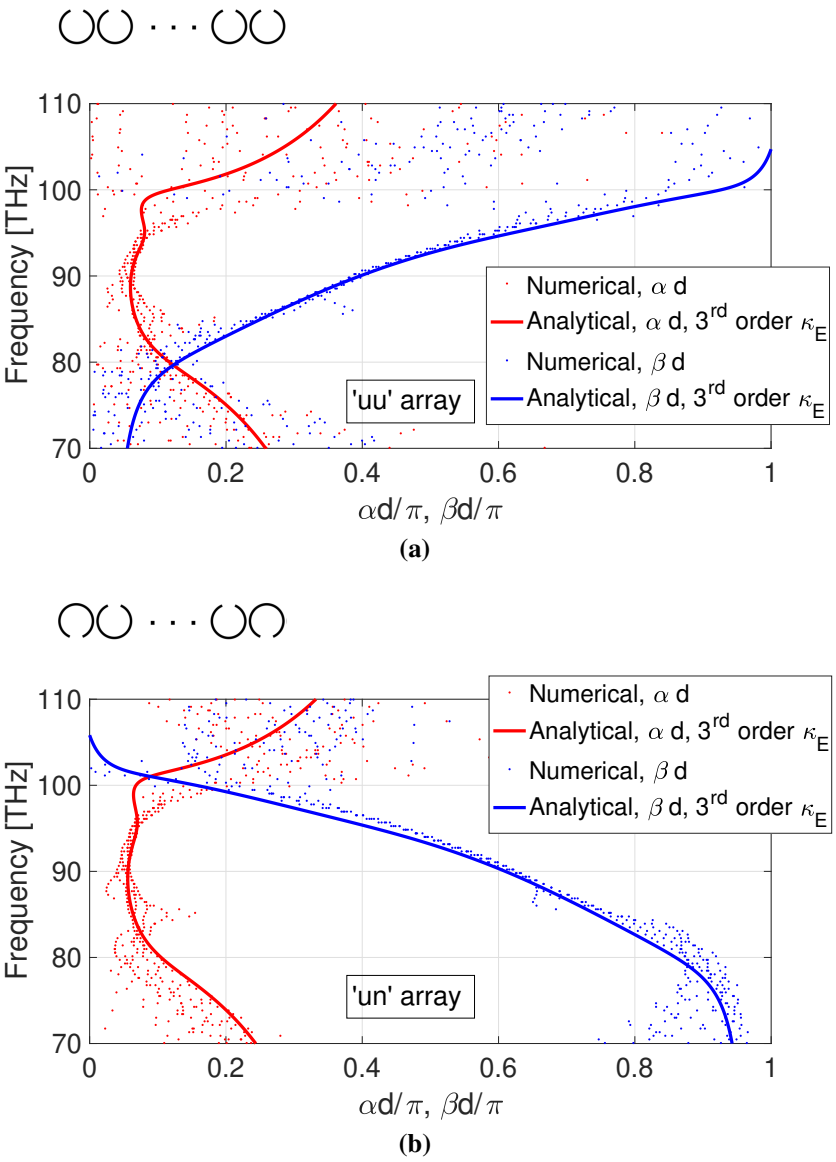


Figure 3.8: Dispersion curves for our (a) 'uu' and (b) 'un' configuration. The red and blue lines are the αd and βd from analytical calculation respectively. In (a) the input parameters for analytical calculations are $f_{0,\text{fit}} = 91.5\,\text{THz}$, $Q = 25$, $\kappa_{E\,1,2,3} = -0.2,\ -0.025,\ -0.015$ (with $\kappa = -\omega_0^2/\omega^2\kappa_\text{E}$, total coupling is positive here) for the 'uu' array. In (b) the parameters are $f_{0,\,\text{fit}} = 92\,\text{THz}$, $Q = 25$, $\kappa_{E\,1,2,3} = 0.22,\ -0.025,\ 0.016$ for the 'un' array. The magnetic coupling is assumed to be negligible in both cases. The red and blue dots are frequency variations of the αd and βd values extracted from the numerical current distributions for sets of three adjacent elements. The numerically modelled array has 14 elements, and element 14 was excited.

THz, although careful designs need to be made in order to have two coherent sources and to control the phase of each source. Alternatively, a narrow beam with a circular polarisation could be used.

The unit cell we used was a silver SRR as shown in Fig. 3.7 (a). Its dimensions are the same as those adopted in [58] – inner radius $R = 80\,\text{nm}$, width $w = 8\,\text{nm}$, height $h = 0.5R = 40\,\text{nm}$, and the split gap $g = 0.15R = 12\,\text{nm}$. The frequency dependence of the permittivity of silver

was taken into account by the Drude model with the plasma frequency, $\omega_p = 1.35 \cdot 10^{16}$ rad / s, and the collision frequency, $\gamma = 33$ THz as in [58]. Properties of the individual SRR and coupled pairs of SRRs were simulated using CST Microwave Studio. The simulated resonant frequency of an individual resonator is $f_0 = 93.5$ THz, and its quality factor is $Q \approx 25$.

With the gaps of the SRRs facing in the same direction, perpendicular to the array axis as illustrated in Fig. 3.7 (b), the coupling between adjacent elements is positive [58]. We refer to this case as the 'uu' configuration. Negative mutual coupling is obtained when the gaps of the adjacent resonators face opposite directions as illustrated in Fig. 3.7 (c). We refer to this case as the 'un' configuration.

Following Eqn (16) and the discussion in Section 2.2, the increased L_{kin} in the THz frequency range leads to suppressed magnetic coupling coefficient, and electric coupling dominates the total coupling effect for THz resonators. Therefore, we assumed that $\kappa_{\text{H}} = 0$ and the total coupling becomes

$$\kappa = -\frac{\omega_0^2}{\omega^2}\,\kappa_{\text{E}} \tag{83}$$

for the analytical calculations in this chapter. We determined the coupling coefficients first based on analytical calculations of the coupling coefficients using the filament current model described in [58]. As discussed in [58], although the trend of the coupling coefficients with variations in the separation between THz SRRs can be determined, there was only qualitative agreement with numerical values. Therefore we adopted a fitting procedure based on the numerical dispersion relationships. The values of the coupling coefficients, with up to the third-order coupling coefficients taken into consideration, were varied to enable good matching between the passband from analytical predictions and that of the numerical results.

Another assumption was made regarding the retardation effect. The retardation is related to the phase changes in the signals as waves travel from one element to the next one, and the resultant coupling coefficients becomes complex numbers as the unit cell size is non-negligible compared to the wavelength of electromagnetic radiation. The analytical model from [58] predicted a real coupling coefficient $|\kappa_{\text{E}}|$ if retardation is neglected. The phase accumulation between the currents in adjacent elements is

$$\varphi = \frac{d}{\lambda}\,\frac{180}{\pi}\ , \tag{84}$$

and with $d \approx 200\,\text{nm}$ between adjacent elements, resonant frequency of around 100 THz, we assumed that the retardation leads to a 5° phase in the complex nearest-neighbour coupling coefficient, i.e. the coupling coefficient is

$$\kappa_{\text{E}1} = |\kappa_{\text{E}1}|\, e^{j5\pi/180} \ , \tag{85}$$

and that the retardation is proportional to the separation between elements.

We studied arrays of 27 identical elements, with lattice period $d = 192\,\text{nm}$. The dispersion relationships of the arrays obtained from numerical calculations in CST (dots) and from analytical calculations (solid curves) are shown in Fig. 3.8. To evaluate the dispersion relationships from numerical current distributions, a 14-element array with a single excitation source applied to the element at one end was simulated. Sets of three adjacent elements were needed for obtaining the dispersion relationship from the numerical current distributions, using Eqn (81). We used five sets of currents with $n = 3, 5, 7, 9, 11$, and the resultant numerical dispersion relationships are plotted as the dots (red for α, blue for β) in Fig. 3.8. It is clearly seen in Fig. 3.8, the 'uu' array, with positive total coupling between adjacent elements, supports forward propagating waves, whereas the 'un' array, with negative coupling, supports backward waves.

For the considered case of pure electric coupling, the dispersion relationship with up to third order coupling taken into account, was derived as,

$$\frac{\omega^2}{\omega_0^2} - 1 - \frac{\mathrm{j}}{Q}\frac{\omega}{\omega_0} = \sum_{n=1}^{3} \kappa_{\text{E}n}\, \cos(nkd) \ , \tag{86}$$

where $\kappa_{\text{E}\,n}$ is the n^{th} order electric coupling. The analytical calculations were based on the fitted parameters, for the 'uu' array: $\kappa_{E,\,1,\,2,\,3} = -0.2,\ -0.025,\ -0.015$. From the numerical calculation of a single SRR, the quality factor $Q = 25$. However, instead of the $f_0 = 93.5\,\text{THz}$, $f_{0,\,\text{fit}} = 91.5\,\text{THz}$ was used as the value for the resonant frequency to generate the analytical dispersion (solid curves) in Fig. 3.8 (a) to enable a reasonable match between numerical and analytical results. It should be noted that the total coupling has the opposite sign to the electric coupling, and the 'uu' array has positive total coupling. The parameters used to obtain the analytical dispersion relationships for the 'un' array are $f_{0,\,\text{fit}} = 92\,\text{THz}$, $Q = 25$,

$\kappa_{E,1,2,3} = 0.22,\ -0.025,\ 0.016$. The fitted resonant frequencies are close to but lower than the value of 93.5 THz from simulating an individual element. Magnetically coupled resonators in close proximity affects the inductance of each individual element, therefore by simulating an individual SRR, we clearly are overestimating its resonant frequency.

The numerical and analytical $\alpha d,\ \beta d$ values have close values within the passband, from 83 to 96 THz, beyond which the numerically calculated values became noisy. This, however, is of no concern as we are not interested in the stop bands.

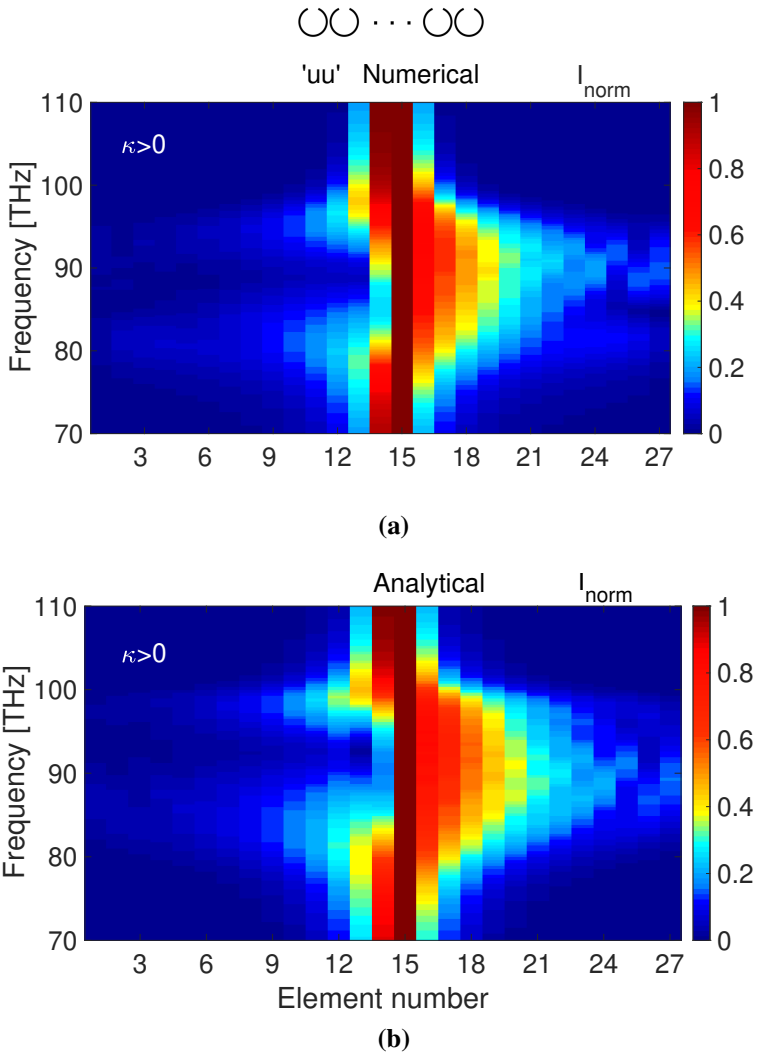


Figure 3.9: Normalised frequency variation of currents in each element, for 27-element arrays as shown in Fig. 3.7, elements 14 and 15 are excited for the 'uu' configuration. (a) numerical calculation, and (b) analytical calculation, with input parameters $f_{0,\,\mathrm{fit}} = 91.5\,\mathrm{THz}$, $Q = 25$, $\kappa_{E,1,2,3} = -0.2,\ -0.025,\ -0.015$ with negligible magnetic coupling.

In order to control the direction of wave propagation in the arrays, element 14 at the middle of the arrays, and the adjacent element 15 were excited as for the MHz structures in the previous

section. The sources applied to elements 14 and 15 have the same magnitude, but the one at element 14 leads that at element 15 by $\pi/2$. The numerical current distributions over frequency among the 27 elements are shown for both configurations in Fig. 3.9 and Fig. 3.10. For each frequency, the magnitude of the currents are normalised to the maximum value. Fig. 3.9 (a) is for the 'uu' configuration, and Fig. 3.10 (a) is for the 'un' array. It is immediately apparent that when the two elements near the centre of the array are excited with sources of a $\pi/2$ phase difference, the injected waves only propagate to one direction but not to the other, and that changing the sign of the coupling coefficient results in opposite directions of propagation, as in full analogy to the results already presented in Section 3.2.1 for the MHz structures in axial and planar configurations.

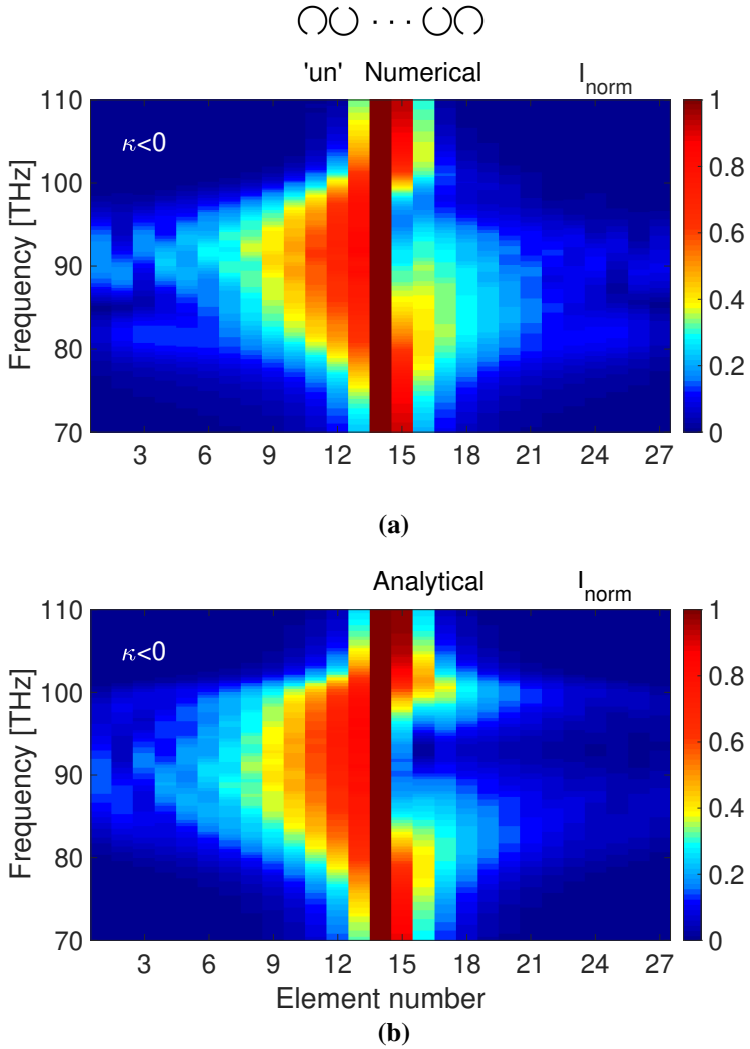


Figure 3.10: Normalised frequency variation of currents in each element, for 27-element arrays as shown in Fig. 3.7, elements 14 and 15 are excited for the 'un' configuration. (a) numerical calculation, and (b) analytical calculation, with input parameters $f_{0,\,\mathrm{fit}} = 92\,\mathrm{THz}$, $Q = 25$, $\kappa_{E,\,1,\,2,\,3} = 0.22,\ -0.025,\ 0.016$ with negligible magnetic coupling.

THz arrays	'uu' [THz]	'un' [THz]
Resonant frequency, $f_{0,\,\mathrm{fit}}$	91.5	92
Optimum frequency, numerical simulations $f_{\mathrm{opt,\,n}}$	88.8	97.6
Optimum frequency, analytical calculations $f_{\mathrm{opt,\,a}}$	92	92.5

Table 2: Key frequencies for the THz arrays.

We analytically calculated the current distributions by evaluating the impedance matrix based on the circuit theory, using the parameters (Q, κ_{H}, κ_{E} and $f_{0,\,\mathrm{fit}}$) evaluated through the fitting of the numerical data. The numerical current distributions in Fig. 3.9 (a) and 3.10 (a) are to be compared with the analytical results in Fig. 3.9 (b) and 3.10 (b), respectively. It can be clearly seen that the simulated and analytical results have the same salient features, with the waves only propagating in one direction and suppressed in the other within similar passbands.

The losses in the SRRs are relatively high, as could be expected for such a low quality factor Q, the signals decay fast as the MI waves travel away from the sources, and the transmitted signals are weak in elements more than 7 cells away from the sources, i.e. beyond element 22 for the 'uu' array and element 7 for the 'un' array as shown in Fig. 3.9 and Fig. 3.10. As a result, there are hardly any standing waves formed.

Based on the numerical current distributions, the optimum frequency, where the wave suppression method works the best and based on the currents in element 12 and 16, is $f_{\mathrm{opt,\,n}} = 88.8\,\mathrm{THz}$ for the 'uu' array. It is close to but slightly lower than the resonant frequency $f_{0,\,\mathrm{fit}} = 91.5\,\mathrm{THz}$. The optimum frequency found for the 'un' array from the numerical current distribution is $f_{\mathrm{opt,\,n}} = 97.6\,\mathrm{THz}$, higher than $f_{0,\,\mathrm{fit}}$, as waves 'leak' to the undesired direction at lower frequencies within the passband, shown in Fig. 3.10 (a), and the suppression of waves works better at higher frequencies. Analytical calculation for the current distribution gives optimum frequencies of $f_{\mathrm{opt,\,a}} = 92\,\mathrm{THz}$ and $f_{\mathrm{opt,\,a}} = 92.5\,\mathrm{THz}$ for the 'uu' and 'un' arrays, which are very close to the $f_{0,\,\mathrm{fit}}$ of the resonator in the corresponding linear arrays. The key frequencies for the THz arrays are summarised in Table 2.

The magnetic fields generated by the 'uu' and 'un' arrays were numerically evaluated at the corresponding optimum frequencies using the h-field monitor in CST Microwave Studio. The arrays were positioned in the xy plane, and the z component of the field in a horizontal plane 5 nm above the top surface of the arrays are shown in Fig. 3.11 (a) and (c). The numerical result for the 'uu' array at $f_{\mathrm{opt,\,n}} = 88.8\,\mathrm{THz}$ is plotted in Fig. 3.11 (a), and for the 'un' array at

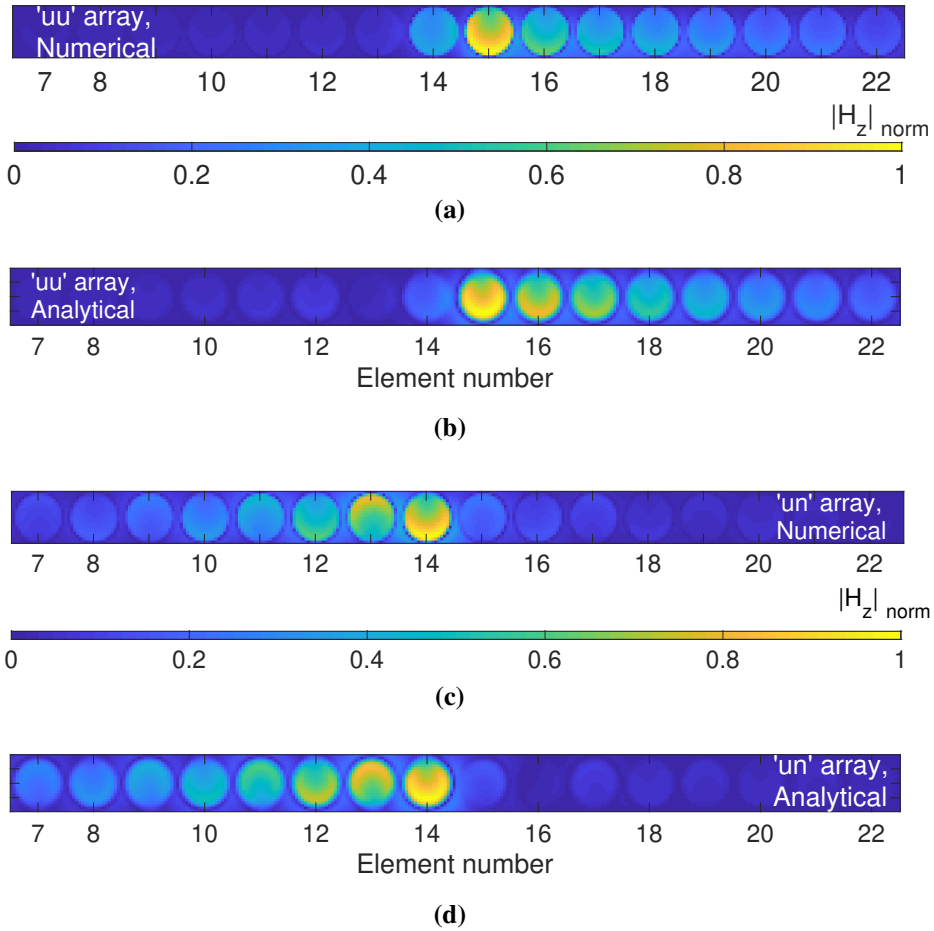


Figure 3.11: The magnetic field $|H_z|$ generated by 27-element arrays with $d = 192\,\text{nm}$, excitations with a phase difference of $\pi/2$ were applied to elements 14 and 15. Only the field above and between elements 7 and 22 is shown. All the field distributions are normalised to the maximum value within the plane of evaluation, which is 5 nm above the top surfaces of the elements (in analytical calculations this is equivalently 25 nm above the filament models). For the 'uu' array, (a) is the numerical field at $f_{\text{opt, n}} = 88.8\,\text{THz}$, and (b) is the analytical field with $f_{\text{opt, a}} = 92\,\text{THz}$. For the 'un' array, (c) is the numerical field at $f_{\text{opt, n}} = 97.6\,\text{THz}$, and (d) is the analytical field at $f_{\text{opt, a}} = 92.5\,\text{THz}$.

$f_{\text{opt, n}} = 97.6\,\text{THz}$ is shown in Fig. 3.11 (c). We focused on the magnetic field above a section with elements not too far away from the centre, i.e. from element 7 to element 22, as the signals beyond these elements are relatively weak.

To compare with the numerical field distribution at the optimum frequency, we analytically calculated the normal component of the magnetic field based on the filament current model of SRR in [61], with the detailed method discussed in the Appendix (Chapter 7.2). The analytical current distribution, from 'V = ZI' calculation, among the 27 elements in the array was used. In each resonator the current is non-uniform and the spatial dependence follows [61]

$$I = \text{C} \ln\left(\frac{g}{4R_{\text{m}}\sin(\theta/2)}\right) , \tag{87}$$

where C is a constant that takes into account the geometrical parameters and the magnitude of the excitation signal, but the value of C is disregarded here since only the normalised field distribution is of interest. g is the size of the gap in each SRR, and

$$R_{\mathrm{m}} = R + w/2 \tag{88}$$

is the average of the inner and the outer radius. θ is the azimuthal angle defined as in Fig. 3.7 (a) [61]. The current in each resonator is the maximum opposite to the gap, at $\theta = 180^{\circ}$ based on the filament model. We assumed that the filament loop is positioned at the centre of the SRR, i.e. 20 nm from both the top and bottom surface of each resonator. Therefore, the plane 5 nm from the top surface of the array in the simulation is equivalently 25 nm from the filament in the model. The z component of the magnetic fields were calculated analytically, normalised to the maximum value within the evaluation plane, at the corresponding $f_{\mathrm{opt,\,a}} = 92\,\mathrm{THz}$ for the 'uu' array, and $f_{\mathrm{opt,\,a}} = 92.5\,\mathrm{THz}$ for the 'un' array. These analytical results are shown in Figs. 3.11 (b) and (d).

Comparing Figs. 3.11 (a) and (b), we can confirm that the numerical and analytical field distributions at the corresponding optimum frequencies are very similar, both showing signals only propagating to the right, with almost no reflections due to the relatively high attenuation. The field distributions also show the orientation of each SRR. Above each element, the normal component of the magnetic field is minimum above the gap, and reaches the maximum above the section of the ring opposite to the gap, as expected from Eqn (87). The main difference between the analytical and numerical result is that the field above the driven element 14 is higher in numerical calculations, probably due to the fact that the excitation sources in the simulations were not taken into account in the calculations. In addition, the attenuation of the signals is slightly higher in numerical calculations as shown by Fig. 3.11 (a), which could be caused by the extra losses of the elements in an array structure, such as the radiation losses, accounted for by simulations but not included in the analytical model.

The analytically calculated field at $f_{\mathrm{opt,\,a}} = 92.5\,\mathrm{THz}$ in Fig. 3.11 (d) is to be compared with the numerical field distribution in Fig. 3.11 (c). In both the numerical and analytical calculations, the waves travelling to the right are almost completely suppressed at the corresponding optimum frequencies, and the reflections from the left end of the 'un' array are very low. The

magnetic field above each element reaches local minima above the gap, showing the alternating orientations of the resonators in the array.

Controllable direction of signal-guiding has been demonstrated using arrays operating in the THz frequency range, using the method of applying multiple sources that we proposed. Changing the sign of the coupling through varying the relative orientation of neighbouring SRRs resulted in a changed in the nature of the supported waves by the waveguides, from forward to backward waves, which then determined the direction of the allowed wave propagation. Qualitative agreement between analytical and numerical results are shown, with salient features present in both cases.

3.3 Non-adjacent Excitations

3.3.1 Results Based on MHz Arrays

When the excited elements are separated by n unit cell sizes, there will be n branches in the passband. Within each branch, the waves are suppressed in one direction but not the other. However, moving from one branch to the adjacent one, the direction of wave suppression switches.

As an example, we focus on the case with $n = 2$ in this chapter, by exciting element 13 and 15 with a phase difference of ψ in our 27-element arrays. For $n = 2$ and $\psi = \pi/2$, the power ratio in Eqn (76) becomes

$$\frac{P_s}{P_t} = \frac{1 - \sin(2\beta d)}{1 + \sin(2\beta d)} \ , \tag{89}$$

where element s is to the left of element 13, and element t to the right of element 15, with the same distances to these two excited elements $13 - s = t - 15$. Based on the dispersion relationships, waveguide structures with positive coupling supporting forward waves have postive propagation coefficient β such as that shown in Fig. 3.3 (b). In order to achieve

$$\frac{P_s}{P_t} > 1 \ , \tag{90}$$

so that the MI waves propagate mostly to the left and are suppressed towards the right end of the array,

$$\beta d > \pi/2 \tag{91}$$

is required, which can be obtained using the axial array for frequencies above around 118 MHz. For the planar array that supports backward waves, we have negative β based on the Brillouin zone, and we need

$$-\pi/2 < \beta d < 0 \tag{92}$$

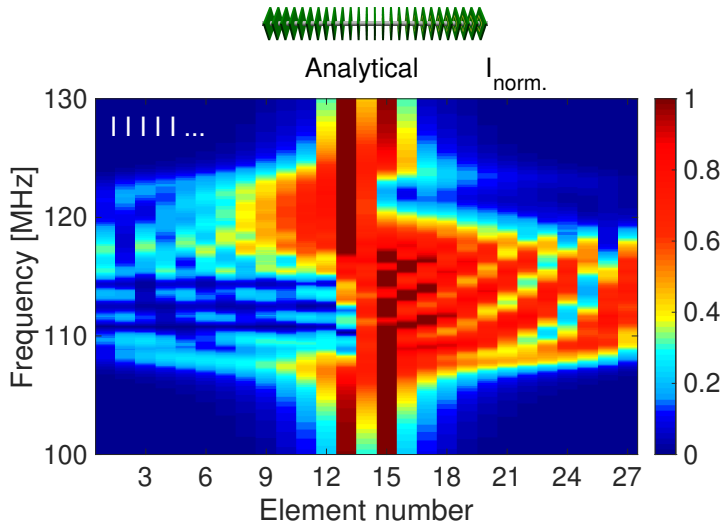
to realise the same propagation direction of MI waves to the left, which is obtained also within the upper half of the passband above around 114 MHz (close to the resonant frequency f_0). For both positive and negative coupling cases, the passband splits into two branches around the resonant frequency, MI waves are only allowed to propagate to the left within the upper branch, and to the right in the lower branch.

The above predictions are justified by the analytical and experimental results of the current distributions within the MHz axial and planar arrays.

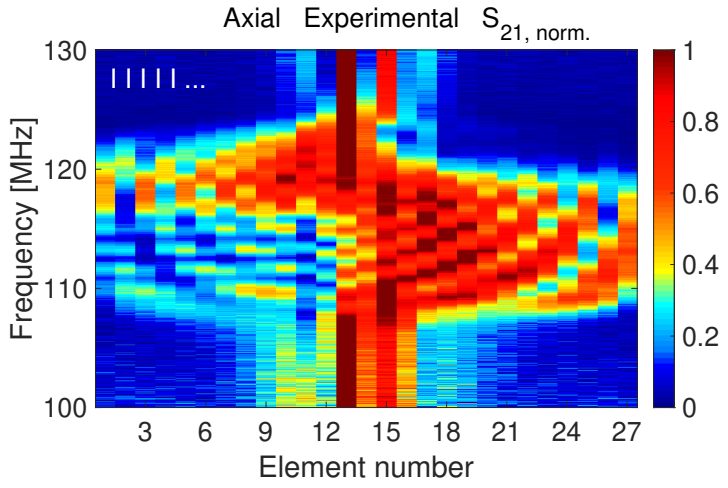
Elements 13 and 15 of the MHz 27-element arrays were excited with sources of the same magnitude, but the current in element 13 lead that in element 15 by $\pi/2$. The analytically calculated current distribution in the elements were compared with the measured results, and the plotted normalised currents are shown in Fig. 3.12 (axial array) and Fig. 3.13 (planar array). The analytical distribution was calculated using the 'V = ZI' impedance matrix method introduced in Section 2.3.2, and the currents were normalised by the maximum value among all the elements for each frequency. The experimental setup was the same as described previously, except for the source antennas that were separated by a distance equal to two unit cell sizes so that the next nearest-neighbour cells were excited.

For both the axial and planar configurations, the passband from approximately 107 to 122 MHz was split into two bands near the resonant frequency under the chosen excitation conditions. The analytical normalised distributions agree well with the experimental results. In both cases, the waves only propagate to the left within the upper frequency band and only to the right for the lower frequency range, as predicted in the last section. The direction of the waves supported in each band did not change as the sign of the coupling coefficient changed. The standing wave patterns are clearly seen in all plots.

For the axial array, the split of the passband occurs at around 117 MHz, very close to the resonant frequency $f_0 = 116.6$ MHz of the resonators in the array. This frequency was not at the middle of the passband, which is due to the significant higher-order coupling effects. In



(a)

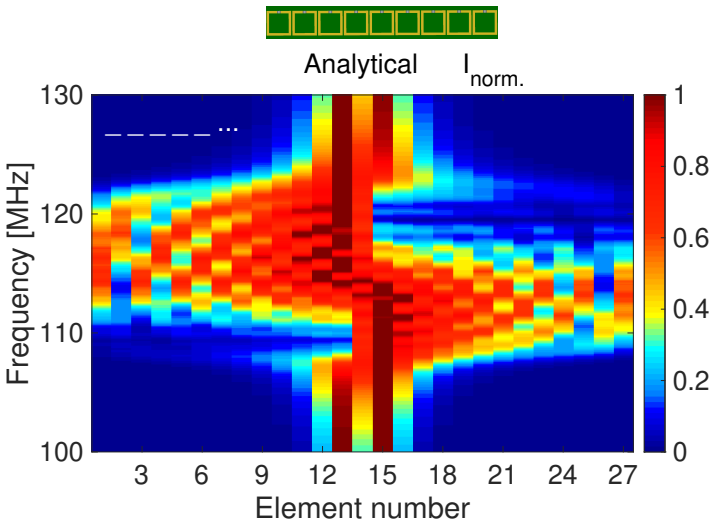


(b)

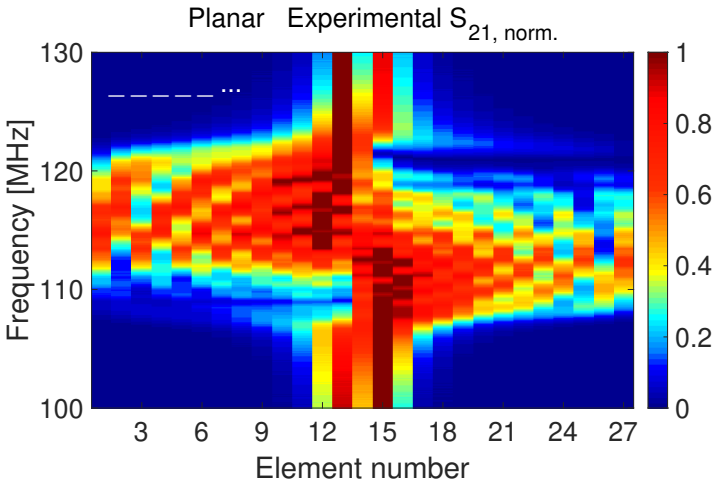
Figure 3.12: The current distribution in an array of 27 coupled resonators in the axial configuration, exciting elements 13 and 15. The source at element 13 leads that at 15 by $\pi/2$, with the same signal magnitude, (a) is the analytically calculated normalised current I_{norm}, normalised to the maximum current at each frequency. The parameters $\kappa_1 = 0.13, \kappa_2 = 0.034$, $\kappa_3 = 0.017$, $f_0 = 116.6$ MHz are used in the calculation. (b) is the experimental scattering parameter $S_{21,\,\text{norm.}}$, normalised to the maximum S_{21} at each frequency.

addition, the strong higher-order couplings lead to the leakage of waves to the left for lower frequencies within the passband. The waves supported by the planar array switched direction also at a frequency very close to the resonant frequency of around 114 MHz. The higher-order couplings are not as strong as those of the axial array, therefore we observe a more evenly distributed widths of the two sub-bands, and the wave suppression works better, giving less leakage of signals in the undesired direction.

Overall the results for the MHz structures confirm our predictions regarding second-nearest



(a)



(b)

Figure 3.13: The current distribution in an array of 27 coupled resonators in the planar configuration, exciting elements 13 and 15. The source at element 13 leads that at 15 by $\pi/2$, with the same signal magnitude, (a) is the analytical normalised current I_{norm}, normalised to the maximum current at each frequency. The parameters used are $\kappa_1 = -0.13$, $\kappa_2 = -0.0062$, $\kappa_3 = -4.3 \cdot 10^{-4}$, $f_0 = 114\,\text{MHz}$. (b) is the experimental scattering parameter S_{21}, normalised to the maximum value at each frequency.

neighbour excitations with a $\pi/2$ phase difference. It should be highlighted that changing the sign of the coupling in this case does not change the direction of allowed wave propagation in both sub-bands.

3.3.2 Monoatomic and Diatomic Structures

As discussed in Section 3.2, when two adjacent elements are excited near the centre of the array with a fixed phase difference, the direction of MI wave propagation is dictated by the nature of

the supported waves, which is opposite for forward and backward waves.

On the other hand, if the two sources are separated by one element, two branches in the passband are formed, with power flow in opposite directions for the two branches. The selective directions of signal propagation do not change if the coupling between elements is switched from positive to negative, as predicted by our analytical expressions of the power ratio in Eqn (78). A more general statement based on the analytical closed form expression is that the sign of the coupling affects the direction of the wave propagations if n is even, but not for an odd number of elements between the excited cells in an array.

Here we offer another explanation of this phenomena based on wave properties. When we excite two elements in a MI waveguide, with a elements between two excited cells, we can treat the unit cell (composite unit of the array) to be composed of $a + 1$ identical elements. For instance, when we excite two adjacent elements near the centre of the 27-element array, we treat the structure as a monoatomic array. However, when element no. 13 and 15 are excited with a phase difference of $\pi/2$, we can treat the MI waveguide as a diatomic structure - each unit cell consists of two strongly coupled elements, and there is also coupling between adjacent diatomic cells. Exciting two elements that are second-order neighbours is equivalent to exciting two adjacent unit cells in a diatomic array, with its general form illustrated in Fig. 3.14. M_a is the mutual inductance between the two resonators in a diatomic cell, and M_b is the mutual inductance between adjacent cells. We note that the arrays we considered correspond to a degenerate case with $M_a = M_b = M$. The dispersion we expect will still feature two passbands, with the lower one being a forward-wave branch and the upper one being a backward-wave branch, but due to the degeneracy of $M_a = M_b$, there will be no stop band separating the two passbands.

The dispersion relationships for mono-atomic structures were discussed in detail and shown in Figs. 3.3 (b) and (c) for the axial and planar array. Treating the structures as a special case for a diatomic array, there are two coupled identical resonators in each unit cell. There are two branches within the passband, one supporting forward waves and the other supporting backward waves. The dispersion relationships for a diatomic structure were derived in Eqn (50), assuming that the resonators all have the same self impedance Z_0. It was shown that with $|M_a|$, $|M_b|$ unchanged, by changing the sign of $M_a \cdot M_b$ affects the dispersion properties, i.e. changing the sign of only one of the two coupling coefficient. Changing the signs of M_a and M_b in Fig. 3.14

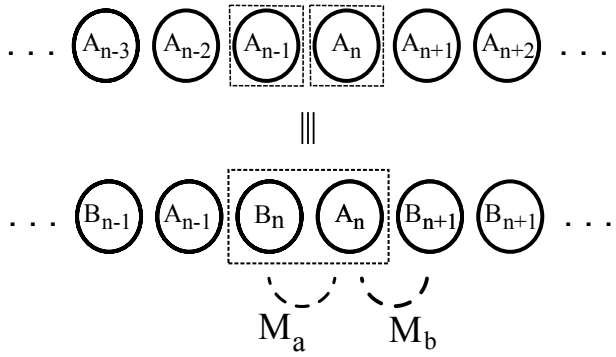


Figure 3.14: Monoatomic (upper) structures can also be treated as diatomic (lower) structures, with different numbering schemes. The dashed rectangles show the composite unit cell in the two configurations. For the diatomic configuration, the mutual magnetic coupling between the two identical resonators A_n and B_n within one unit cell is denoted as M_a, and M_b is the mutual inductance between adjacent cells, e.g. between element A_n and B_{n+1}.

simultaneously does not change the nature of the supported waves in each branch.

MHz structures

The uniform arrays we were interested in fall into a special category with

$$M_a = M_b = M_1 \ . \tag{93}$$

This explains qualitatively why the propagation direction in both dispersion branches remain the same for both the planar ($\kappa < 0$) and the axial ($\kappa > 0$) cases if there is one element between the two excited elements.

For the axial and planar arrays operating in the MHz frequency range, we take into account up to the third order coupling in the analytical model. The Kirchhoff's equations for the currents are, similar to Eqn (48),

$$\begin{cases} j\omega M_b A_{n-1} + j\omega M_a A_n + Z_0 B_n + j\omega M_{b2}(B_{n-1} + B_{n+1}) + j\omega M_{b3}(A_{n-2} + A_{n+1}) & = 0 \\ \\ j\omega M_a B_n + j\omega M_b B_{n+1} + Z_0 A_n + j\omega M_{a2}(A_{n-1} + A_{n+1}) + j\omega M_{a3}(B_{n-1} + B_{n+2}) & = 0 \end{cases} , \tag{94}$$

where M_{a2} and M_{b2} are the mutual inductances between second-order pairs, e.g. M_{a2} is the coupling between element A_n and A_{n-1}, and M_{b2} is between element B_n and B_{n-1} in Fig. 3.14.

M_{a3} and M_{b3} are the corresponding third-order coupling coefficients, and

$$\begin{cases} M_a = M_b & = M_1 \\ M_{a2} = M_{b2} & = M_2 \\ M_{a3} = M_{b3} & = M_3 \end{cases} \tag{95}$$

for both the planar and axial structures. The n^{th} order coupling coefficient is $\kappa_n = 2M_n/L$, with $n = 1,\ 2,$ or 3. Solving Eqn (94), we arrive at the dispersion relationship for the diatomic structure taking into account up to the third-order couplings,

$$p\cos^3(k\,d) + q\cos^2(k\,d) + r\cos(k\,d) + s = 0\ , \tag{96}$$

where

$$\begin{cases} p = -2\,\kappa_3^2 \\ \\ q = \kappa_2^2 - 2\,\kappa_1\kappa_3 \\ \\ r = 2\kappa_2\,\dfrac{Z_0}{j\omega L} - \dfrac{\kappa_1^2}{2} - \kappa_1\kappa_3 + \dfrac{3}{2}\kappa_3^2 \\ \\ s = \left(\dfrac{Z_0}{j\omega L}\right)^2 - \dfrac{1}{2}\left(\kappa_3 - \kappa_1\right)^2 \end{cases} . \tag{97}$$

Recalling that the axial array we studied has $\kappa_1 = 0.13,\ \kappa_2 = 0.034, \kappa_3 = 0.017$, and the planar array has $\kappa_1 = -0.13,\ \kappa_2 = -0.0062,\ \kappa_3 = -4.35 \cdot 10^{-4}$, the dispersion curves from Eqn (96) are plotted in Fig. 3.15 (a). The analytical dispersion curves are compared with the dispersion extracted from experimental data. The measured dispersions were extracted from three resonators that are second-order neighbours, so that the $I_{n-1},\ I_n,\ I_{n+1}$ in Eqn (81) are replaced by either a set of $A_{n-1},\ A_n,\ A_{n+1}$ or by $B_{n-1},\ B_n,\ B_{n+1}$ (as in Fig. 3.14 for the diatomic structures).

For both the axial and planar configurations, the analytical and measured dispersion curves agree remarkably well in the passband. There is a turning point at 120 MHz in the analytical attenuation coefficient (solid red) of the axial array in Fig. 3.15 (a), which is less obvious from the measured data (dotted red) due to the noises. This turning point is due to the relatively strong second-order coupling in the axial structure. At a frequency around 118.7 MHz, there

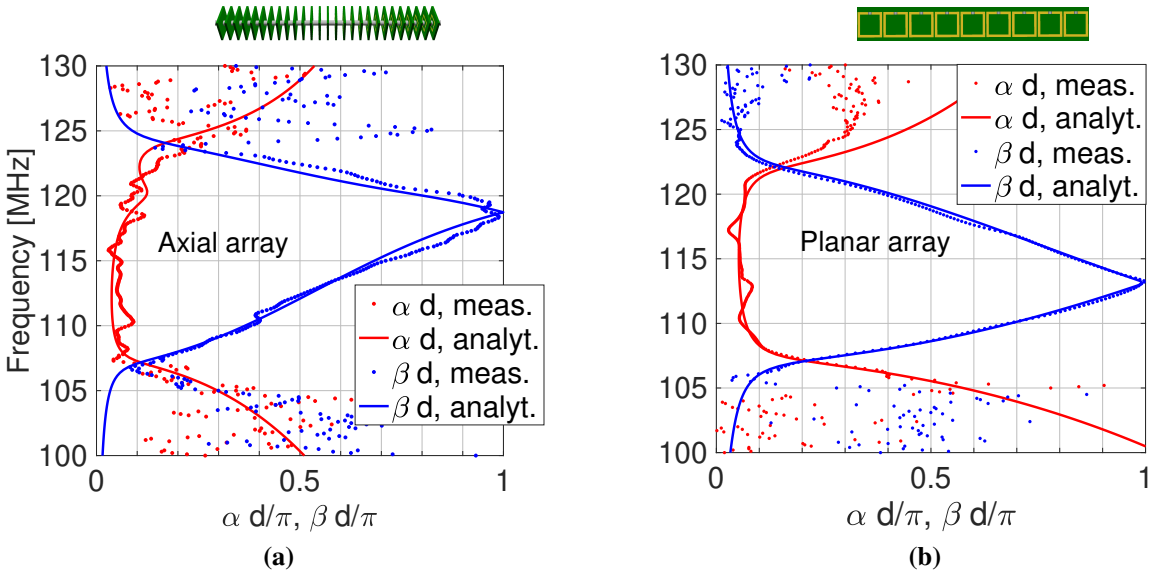


Figure 3.15: Dispersion relationships based on diatomic models. The solid curves are the analytical results, and the dotted ones are extracted from the measured data. The sets of 3 elements from which we obtained the measured dispersion relationships are the ones that gave optimum match between analytical and measured results - the set for axial array is element 21, 23 and 25; and for planar array is element 20, 22 and 24. The attenuation coefficient curves (αd) are red, and the propagation coefficient curves (βd) are blue. For both the axial and planar array, up to third-order interactions were taken into account to obtain the analytical results. (a) Axial structure, $\kappa_1 = 0.13,\ \kappa_2 = 0.034,\ \kappa_3 = 0.017$. (b) Planar structure, $\kappa_1 = -0.13,\ \kappa_2 = -0.0062,\ \kappa_3 = -4.35 \cdot 10^{-4}$.

is a discontinuous point in the βd values which divides the passband into two sub-bands - the nature of the waves supported by the structure switches between forward and backward waves at this frequency. This frequency is slightly higher than the resonant frequency 116.6 MHz of the array, and the two sub-bands do not share the overall passband equally, due to the strong second-order coupling κ_2.

Similar features are seen for the dispersion relationships of the planar array in Fig. 3.15 (b). The self resonance of the resonators in the planar array is 114 MHz, and the wave nature changes at around 113.2 MHz as shown by the turning point in βd. Above 113.2 MHz we have backward waves travelling in the structure, and forward waves are supported by the structures at frequencies below. The measured and analytical attenuation coefficients αd agree well.

THz arrays

For the THz arrays, the magnetic coupling is suppressed, and we assumed that the coupling between elements is purely electric. With up to the third-order interactions are K being the mutual capacitance between elements, we derived the dispersion relationships for a diatomic

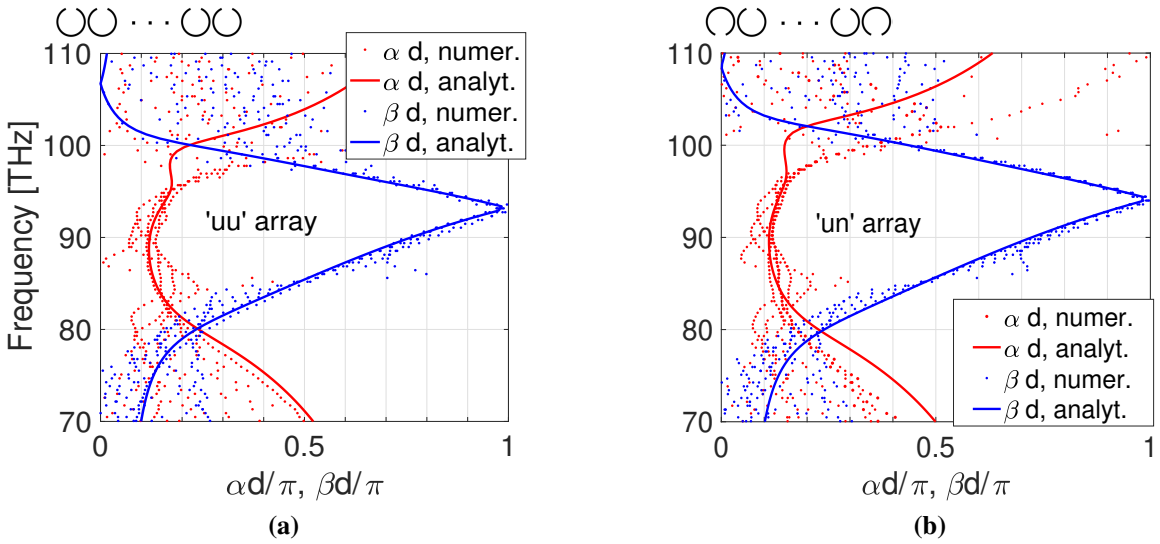


Figure 3.16: Dispersion relationships based on diatomic models for the THz structures. The attenuation coefficient αd is red and the propagation coefficient βd is blue. Numerical results are represented by dots, and the analytical values are plotted as solid curves. (a) 'uu' array, $\kappa_{\mathrm{E1}} = -0.2$, $\kappa_{\mathrm{E2}} = -0.025$, $\kappa_{\mathrm{E3}} = -0.015$, and $f_0 = 91.5\,\mathrm{THz}$ for analytical calculations, and (b) 'un' array, $\kappa_{\mathrm{E1}} = 0.22$, $\kappa_{\mathrm{E2}} = -0.025$, $\kappa_{\mathrm{E3}} = 0.016$, and $f_0 = 92\,\mathrm{THz}$.

array structures taking into account up to third-order coupling,

$$p\cos^3(k\,d) + q\cos^2(k\,d) + r\cos(k\,d) + s = 0\ , \tag{98}$$

where

$$\begin{cases} p = -2\,\kappa_{\mathrm{E3}}^2\,\dfrac{\omega_0^4}{\omega^4} \\ q = \kappa_{\mathrm{E2}}^2\,\dfrac{\omega_0^4}{\omega^4} - 2\,\kappa_{\mathrm{E1}}\kappa_{\mathrm{E3}}\,\dfrac{\omega_0^4}{\omega^4} \\ r = -2\,\kappa_{\mathrm{E2}}\dfrac{Z_0}{j\omega L}\dfrac{\omega_0^4}{\omega^4} - \dfrac{1}{2}\kappa_{\mathrm{E1}}^2\,\dfrac{\omega_0^4}{\omega^4} - \kappa_{\mathrm{E1}}\kappa_{\mathrm{E3}}\,\dfrac{\omega_0^4}{\omega^4} - \dfrac{3}{2}\kappa_{\mathrm{E3}}^2\,\dfrac{\omega_0^4}{\omega^4} \\ s = \dfrac{Z_0^2}{(j\omega L)^2} - \dfrac{1}{2}\,\kappa_{\mathrm{E1}}^2\,\dfrac{\omega_0^4}{\omega^4} - \dfrac{1}{2}\,\kappa_{\mathrm{E3}}^2\,\dfrac{\omega_0^4}{\omega^4} + \kappa_{\mathrm{E1}}\kappa_{\mathrm{E3}}\,\dfrac{\omega_0^4}{\omega^4} \end{cases} . \tag{99}$$

The κ_{E1}, κ_{E2}, κ_{E3} are the first, second, and third-order coupling coefficients of the 'uu' and 'un' arrays based on the monoatomic models. The parameters for analytical calculations are restated here, $\kappa_{\mathrm{E1}} = -0.2$, $\kappa_{\mathrm{E2}} = -0.025$, $\kappa_{\mathrm{E3}} = -0.015$, and $f_0 = 91.5\,\mathrm{THz}$ for the 'uu' array, and $\kappa_{\mathrm{E1}} = 0.22$, $\kappa_{\mathrm{E2}} = -0.025$, $\kappa_{\mathrm{E3}} = 0.016$, and $f_0 = 92\,\mathrm{THz}$ for the 'un' array.

The analytical dispersion relationships based on the diatomic models following Eqn (98) are plotted in Fig. 3.16, with the solid red curves being the attenuation coefficient and solid blue

curves as the propagation coefficient. The values for αd (red dots) and βd (blue dots) extracted from numerical current distributions are plotted as well, and five sets of numerical results were used for the extraction (I_{n-2}, I_n, and I_{n+2} with $n = 3, 5, 7, 9, 11$). The passband agree qualitatively for the numerical and analytical results, and the propagation coefficients show very good quantitative agreement for both configurations. We observe similar salient features to those seen for the MHz structures in Fig. 3.15 - the wave supported by the structures switch between forward and backward waves at frequencies near the resonant frequency, confirming again that changing the sign of the first-order coupling coefficient does not change the nature of the waves in each branch.

3.4 Summary

In this chapter we proposed a method to suppress the wave propagation in a controllable fashion, to one end of a MI waveguide but not to the other. Theoretical basis of the method have been provided.

We have investigated two different configurations of the MI waveguide - one with a positive coupling, the other with a negative coupling. Up to the third-order coupling coefficients were taken into account in the analytical models, and non-negligible higher-order coupling coefficients have led to a shift in the passband, as well as asymmetrical current distributions within the passband. It was demonstrated for the MHz arrays, with experimental results agreeing very well with analytical predictions, that by exciting two adjacent elements with a $\pi/2$ phase difference, selective signal propagation to only one end of the array could be achieved. The selective direction of signal propagation is determined by whether the supported MI waves are forward or backward waves.

The same phenomenon of controllable unidirectional signal-guiding was shown for THz structures. EI waves are supported in these nanostructured arrays, where electric coupling dominates and magnetic coupling is suppressed due to the increased kinetic inductance of the meta-atoms. We obtained qualitative agreements between analytical and numerical results, with the direction of the guided signals also shown to depend on the forward- or backward- wave nature of the supported waves.

Extending the analysis to diatomic arrays, simultaneous branches supporting waves of both

types, i.e. forward or backward, allowed us to realise frequency-controlled switching of unidirectional signal-guiding. This was achieved by exciting a pair of non-nearest neighbours in the arrays, with a phase difference of $\pi/2$. The analytical dispersion relationship for such diatomic structures, taking into account the third-order coupling was justified by the dispersion relationships extracted from experimental results for the MHz arrays and from numerical results for the THz arrays.

4 Near-Field Position Sensor

In Chapter 3, we discussed the properties of MI waves confined in metamaterial-based structures and developed a method of controlled unidirectional signal-guiding. The sensitivity of the composite magnetic meta-atoms to the variations in the local electromagnetic fields makes the MI waveguide very attractive as a basis for sensing systems. In this chapter, we focus on the near-field interactions between the MI waves supported by a MI waveguide and external conductive objects in close proximity that disturbs the local electromagnetic fields, and propose a novel contactless distributed near-field position sensor locating metallic objects placed along a MI waveguide.

Human-machine interactions has been a key driver to the development of many technologies over the last two decades, and in particular, the touch sensitive screens have become nearly ubiquitous thanks to their adoption for smart phone designs [159–162]. Most of these touch screens rely on the changes in the mutual capacitance between adjacent electrodes in a dense grid, which is made of transparent conductors and is above the display [163]. Polling the electrode grids in pairs, repeated measurements are required for the readout and the readout electronics are relatively complex [164]. With the rapid and advanced development for the touch screens, there are several drawbacks, one of which is the limited range and insensitivity of these screens – for instance no capacitive screens, so far, work well through gloves.

Reducing the readout complexity of touch screens, the ultimate goal is to achieve position sensing with a single-port measurement. To this end we have started investigating the use of MI waveguides to enable one-dimensional localisation via confined waves [165]. The meta-atoms, such as the SRRs forming the MI waveguide, are sensitive to the electromagnetic environments they are exposed to. This makes metamaterial-based structures suitable for development of sensors, as introduced in Section 2.3.3.

We propose in this chapter to realise position sensing of a metal object based on single-port measurements of the reflection spectrum from a MI waveguide [126]. The conductive object interacts with and causes noticeable changes to the self-impedance of the element below it, and thus creating a defect in the otherwise uniform array. The MI waves injected at one end of the array are reflected from the defect, resulting in a unique reflection spectrum for every defect location. The analytical reflectance spectrum is verified by experimental results. Based

on our knowledge of the MI wave dispersion characteristics and the supported eigenmodes, we develop an algorithm for localising the conductive object. The accuracy of the algorithm is presented, and the effects of matching terminations to the array ends are discussed.

4.1 Structure

4.1.1 MI Waveguide

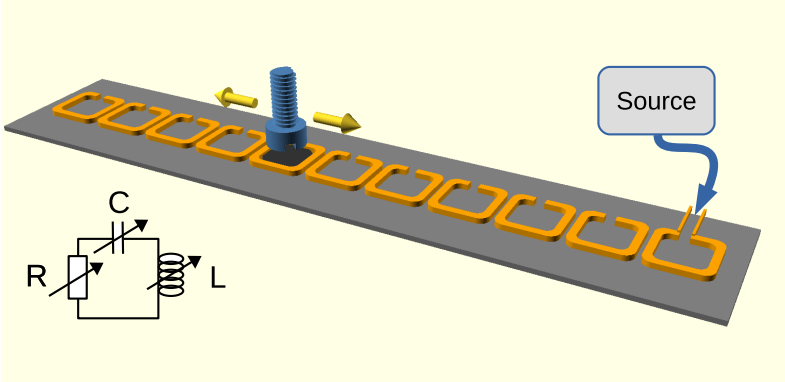


Figure 4.1: MI waveguide formed from magnetically coupled SRRs, with a metal object (the bolt) creating a defect at cell 7 from the source, where the wave signals are injected. The inset is an LCR circuit to model the SRRs.

A one-dimensional MI waveguide shown in Fig. 4.1, with a conductive object such as a metal bolt, is the basis for our sensing structure. The object interacts with the unit cells to create a defect in the array. The signals injected by a source at the first element propagate down the array, partially scattered from the defect along the way and partially from the array end, forming a standing wave pattern of circulating currents.

The MI waves supported in the 1D array are dispersive. Dispersion relationships derived in Eqn (80) of Section 2.3.2 can also be written in the following form assuming only first-order coupling,

$$\cos\left(kd\right) = -\frac{Z_0}{2\,j\omega M}\ , \tag{100}$$

and recalling that Z_0 is the self-impedance of the unperturbed meta-atoms. The mutual inductance M between adjacent cells is assumed to be unaffected by the presence of the metal object for simplification, as we aimed for a proof-of-principle work as basis for future development of sensing devices based on MI waves.

Another concept related to the MI wave properties is the eigenmode supported by an N-

element array – the MI waves travelling in the array from one end to the other will mostly reflect back and form standing waves which have integer numbers of half periods. The frequencies corresponding to the eigenmodes can be determined using the method based on the impedance matrix as introduced in Section 2.3.2. We treat the array as being equivalent to an array of $N+2$ elements, with the two end elements being virtual elements with currents of zero magnitude. The n^{th} order mode supported by the structure has the wavelength of $2(n+1)d$. The propagation coefficients k of the N standing wave modes are [63]

$$k_n = \frac{2\pi}{\lambda_n} = \frac{\pi}{(n+1)d},\ n = 1, 2, 3...N\ , \tag{101}$$

where λ_n is the wavelength of the n^{th} order mode and d is the lattice period. The eigenmode frequencies, ω_n, related to k_n by the dispersion equation in Eqn (100), correspond to the resonances exhibited by the N-element array, and the reflectance will reach local minima at these frequencies.

4.1.2 Defect Element

The impact of a foreign object, such as the metal bolt we used here, can be quantised by the variation in the self-impedance of the defect element. The sensing 1D array was fabricated as a PCB carrying square-shaped resonators (10 mm on a side, of 1 mm width). Each resonator was tuned by the addition of a 100 pF surface mount capacitor, which reduced the sensitivity of the resonator to the dielectric environment, as the majority of the electric field was enclosed by the mounted capacitor. The magnetic fields, on the other hand, permeate each cell's local space, making the resonators sensitive to foreign objects that could perturb the local magnetic fields. We modelled the resonators as LCR circuits composed of inductance L, capacitance C and resistance R as discussed previously and drawn in Fig. 4.1. All the losses present in the resonators, including the ohmic and radiation losses, were taken into account by the resistance R [166].

A calibration experiment was conducted with a single loaded split ring resonator to quantify the presence of a metal object. A highly conducting object (a steel M6 bolt, with a hexagonal head of 10 mm size) was placed above the resonator, with their centres aligned axially, and moved towards the resonator from 12 mm separation to close contact. The resonant frequency,

f_0, and the quality factor, Q, of the resonator were measured, shown in Fig. 4.2 (a) and (b). As the vertical height z of the bolt approached 12 mm, the resonant characteristics of the element tended to the unperturbed values of $f_0 = 113.4$ MHz and $Q = 90$. When the metal bolt was almost touching the element, we achieved the strongest interaction between the metal bolt and the resonator below, which resulted in $f_0 = 130$ MHz and $Q = 20$.

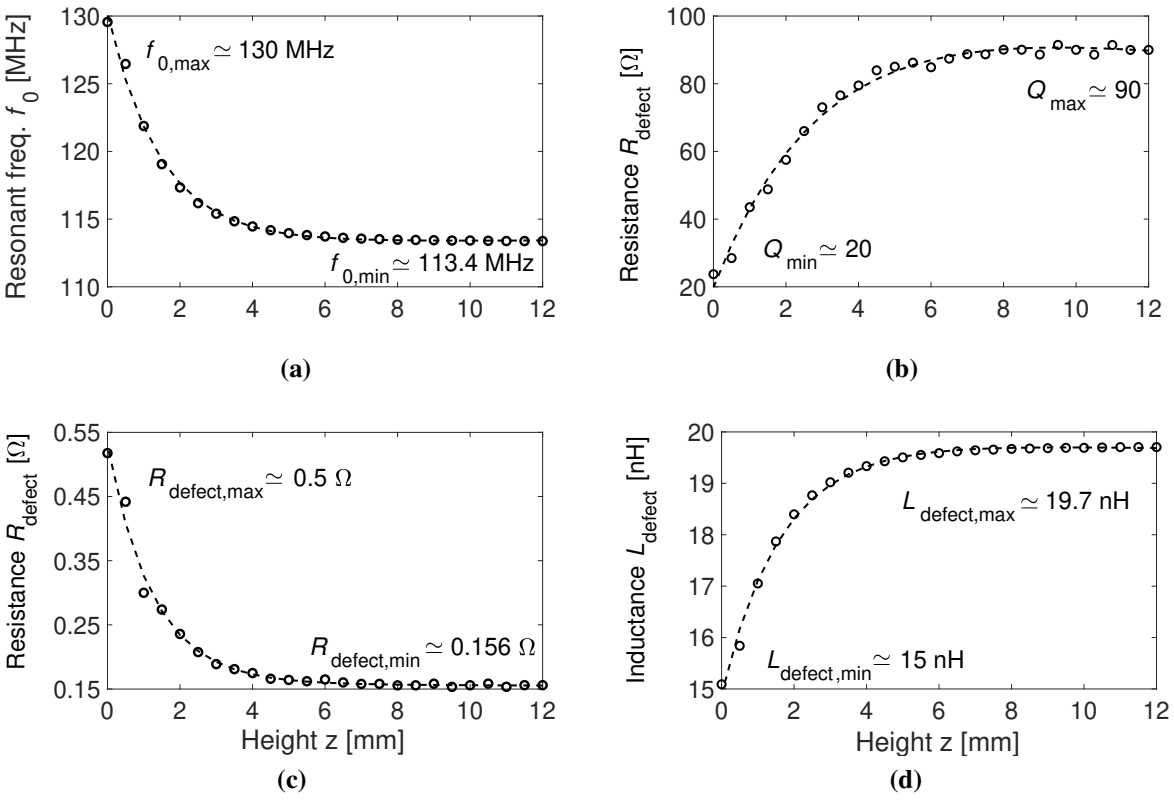


Figure 4.2: Quantisation of the impact of a metal object (M6, 10 mm bolt head size) as a function of its height z above a meta-atom, being a loaded PCB split resonator. The circles in the sub-plots are the measured data, and the dashed curves are the fitted values. (a) is the measured f_0 of the meta-atom. As z increases from 0 to 12 mm, f_0 drops from 130 MHz to 113.4 MHz with the latter one being the unperturbed value. (b) is the variation of the quality factor Q which increases from 20 to 90. The values in (c) and (d) are evaluated based on Eqn (102) from the measured data points in (a) and (b). (c) is the resistance of the defect element R_{defect} which varies from 0.5 to 0.16 Ω. (d) is the inductance of the element, L_{defect} changing from 15 to 19.7 nH. The end values at $z = 12$ mm for these parameters are very close to the unperturbed values for the element.

As the metal object approached the single element, the element's resonant frequency f_0 increased while Q reduced, representing a decrease in the product of L and C and an increase in R. The modulation of the resonator by the metal object was modelled following Eqn (102), assuming the capacitance C was unchanged (which is valid since the added capacitance was

much higher than the self-capacitance of the resonator),

$$\begin{cases} L = \dfrac{1}{C}\dfrac{1}{(2\pi\, f_0)^2} \\ \\ R = \dfrac{2\pi\, f_0\, L}{Q} \end{cases} . \tag{102}$$

The resultant R and L are shown in Fig. 4.2 (c) and (d). The unperturbed values are $L = 19.7\,\text{nH}$, $R = 0.156\,\Omega$, and when the bolt is closest to the resonator, these values become $L_{\text{defect}} = 15\,\text{nH}$ and $R_{\text{defect}} = 0.5\,\Omega$. It should be noted that the resonant characteristics of the element were measured by placing a metal object at changing heights z. Equivalently, placing metal bolts of varying sizes at a fixed z value could result in similar detuning effects on the resonator. Decreasing the size of the metal bolt would lead to weaker interactions between the object and the affected element, i.e. there would be smaller perturbations in its L and R. For instance, a steel bolt head of 7 mm size with $z = 0.4\,\text{mm}$, resulted in experimental values of $L_{\text{defect}} \approx 17.1\,\text{nH}$ and $R_{\text{defect}} \approx 0.29\,\Omega$ of the resonator below it, very close to the measured values when the bolt head with 10 mm size was placed at 1 mm above the element. The material and shape of the metal object will also affect the strength of perturbation given a fixed vertical height, and a detailed analysis could be performed in the future, but we will refer to a bolt head of 10 mm size as the metal object in this chapter.

In a MI array, when the defect element m experiences strong interactions with the metal object, its resonant characteristics (f_0, Q) change by such a large extent that they deviate enough from the other identical elements in the MI waveguide, resulting in a strong discontinuity in the line at the defect, causing MI wave reflections. The number of eigenmodes supported by the effective array, truncated by the defect, changes with the position of the defect in the waveguide, resulting in a unique reflection spectrum from the MI waveguide, which enables the localisation of the defect position (and hence the location of the metal object).

4.2 Reflections of MI Waves

4.2.1 Theoretical Model

We injected signals into a line of N unit cells by exciting the element at the start of the line (cell 1), and measure the input impedance of the MI waveguide when a metal object modifies the

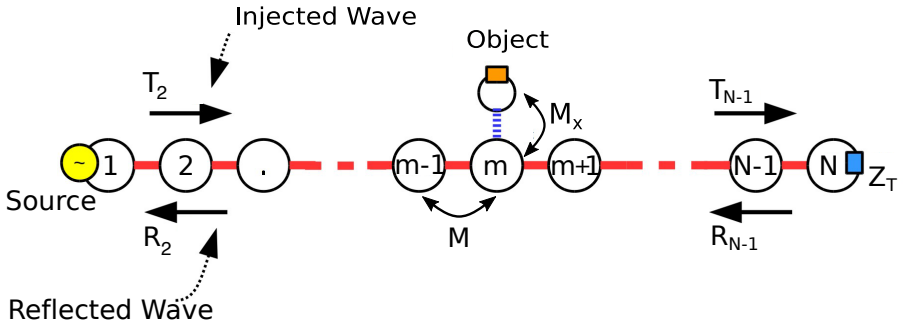


Figure 4.3: Schematic diagram describing the MI waveguide system with the source injecting waves at cell 1 and the metal object interacting with its nearest neighbour cell m. The mutual coupling between adjacent cells is M, and the mutual coupling between the object and cell m is M_x. The terminating impedance added to the cell N at the array end is Z_{T}.

impedance of one of the cells. The object is nearest to cell m, and we call this cell m the defect cell. Figure 4.3 is a depiction of the disturbed array, where cell m is coupled to the conductive object and their mutual inductance is denoted as M_x. The mutual inductance between adjacent cells in the line is M. The terminating impedance of the last cell N is Z_{T}.

First the terminal reflectance ρ_{T} was derived for an array of N elements. The injected signals arriving at element N would be reflected. We defined ρ_{T} as

$$\rho_{\mathrm{T}} = \rho_{N-1} = \frac{R_{N-1}}{T_{N-1}} \ , \tag{103}$$

where R_{N-1} and T_{N-1} are the reflected and incident MI wave amplitudes at cell $(N-1)$ as shown in Fig. 4.3. In cases where losses are sufficiently low, this overall reflectance of the system, ρ_{T} will be close to unity.

The value of current I_p in any resonator p of the line can be represented as the sum of the transmitted T_p and the reflected waves R_p that are annotated in Fig. 4.3

$$I_p = T_p + R_p \ . \tag{104}$$

Both T_p and R_p can be expressed based on the MI wave properties,

$$\begin{cases} T_p = T_{p-1}\, e^{-jkd} \\ \\ R_p = R_{p-1}\, e^{\,jkd} \end{cases} , \tag{105}$$

giving the reflection coefficient $\rho_p = R_p \,/\, T_p$ at cell p with respect to ρ_{T} as

$$\rho_p = \rho_{\mathrm{T}}\, e^{-2j(N-1-p)kd} \ . \tag{106}$$

Given the reflectance evaluated at a certain point p of the line, we are also able to evaluate the reflectance at another cell q based on ρ_p following Eqn (106), provided that there is no external interferences and the line between element p and q remains a uniform array. We call this process of finding the reflectance based on the reflectance at another cell as 'referring' from cell p to cell q.

Using the circuit theory, the currents near the end of the array can be written as

$$\begin{cases} Z_{\mathrm{M}} I_{N-1} + (Z_0 + Z_{\mathrm{T}})\, I_N = 0 \\ Z_{\mathrm{M}}\,(I_{N-2} + I_N) + Z_0 I_{N-1} = 0 \end{cases} , \tag{107}$$

where $Z_{\mathrm{M}} = j\omega M$ is the mutual impedance, and

$$\begin{cases} I_{N-1} &= T_{N-1}\,(1+\rho_{\mathrm{T}}) \\ I_{N-2} &= T_{N-1} e^{\,jkd} \left(1 + \rho_{\mathrm{T}}\, e^{-2jkd}\right) \end{cases} . \tag{108}$$

Solving the simultaneous equations in Eqn (107) by substituting the expressions for I_{N-1}, I_{N-2} in Eqn (108), the reflectance of the line termination can be written in the following form [106]

$$\rho_{\mathrm{T}}(Z_{\mathrm{T}}) = \frac{Z_{\mathrm{M}}^2 - (Z + X e^{\,jkd})(Z_0 + Z_{\mathrm{T}})}{(Z_0 + Z_{\mathrm{M}} e^{-jkd})(Z_0 + Z_{\mathrm{T}}) - Z_{\mathrm{M}}^2} \ , \tag{109}$$

For an array with an open end, $Z_{\mathrm{T}} = 0$. The expression in Eqn (109) could be rearranged to obtain the effective termination impedance on any element p due to the rest of the line as

$$Z_{\mathrm{T}}^{(p)} = \frac{Z_{\mathrm{M}}^2 (1+\rho_{p-1})}{Z_0(1+\rho_{p-1}) + Z_{\mathrm{M}}(\rho_{p-1} e^{-jkd} + e^{\,jkd})} - Z_0 \ . \tag{110}$$

The meaning of Eqn (110) is that, given the reflectance evaluated at cell $p-1$, the elements and any terminations after cell p can be represented by a termination $Z_{\mathrm{T}}^{(p)}$ effectively added to the element.

The next step is to incorporate the modulation in the defect element impedance as a result of its interactions with the conductive object. As we have evaluated the ρ_{T} at cell $N-1$, we could refer the reflectance back to cell m because the elements between cell m and the end of line are identical. The reflectance at element m is

$$\rho_m = \rho_{\mathrm{T}}\, e^{-2j(N-m-1)kd} \tag{111}$$

based on Eqn (106). The effective termination $Z_{\mathrm{T}}^{(m+1)}$ at element $m+1$, based on Eqn (110), was written as

$$Z_{\mathrm{T}}^{(m+1)} = \frac{Z_{\mathrm{M}}^2(1+\rho_m)}{Z_0(1+\rho_m) + Z_{\mathrm{M}}(\rho_m e^{-jkd} + e^{\,jkd})} - Z_0 \ . \tag{112}$$

The defect cell m, affected by the metal object, has its terminal impedance

$$Z_{\mathrm{T}}^{(m)} = Z_{\text{eff}} + Z_{\text{defect}} \ , \tag{113}$$

where Z_{defect} is the amount of change in the impedance due to the metal object, and Z_{eff} is the effective impedance presented by the terminal impedance of element $m+1$ to the defect element m [106],

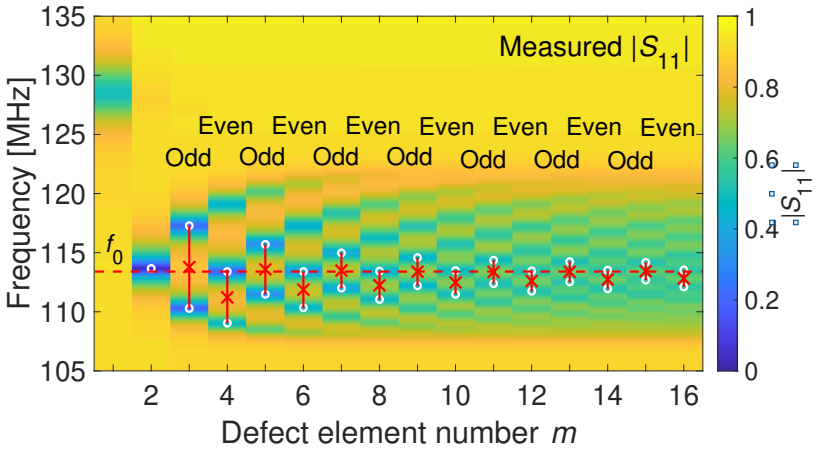
$$Z_{\text{eff}} = \frac{-Z_{\mathrm{M}}^2}{Z_{\mathrm{T}}^{(m+1)} + Z_0} \ . \tag{114}$$

We then evaluated the reflectance at element $m-1$, i.e. ρ_{m-1}, based on the corresponding effective terminal impedance $Z_{\mathrm{T}}^{(m)}$ evaluated at cell m.

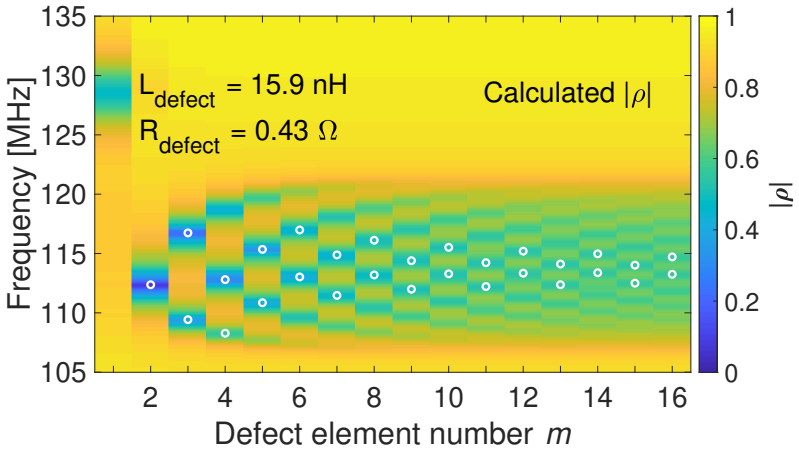
Similarly, we evaluated the effective terminating impedance at the first cell representing the line section from cell 2 to cell N. We referred ρ_{m-1} to the source, and calculated $Z_{\mathrm{T}}^{(1)}$, and $Z_{\text{in}} = Z_0 + Z_{\mathrm{T}}$. The reflectance seen by the input source is,

$$\rho = \frac{Z_{\text{in}} - Z_{\text{ref}}}{Z_{\text{in}} + Z_{\text{ref}}} \ , \tag{115}$$

where Z_{ref} is the effective impedance of the source taken as a reference.



(a)



(b)

Figure 4.4: Measured scattering parameter $|S_{11}|$ and analytical reflectance $|\rho|$ spectrum with varying defect locations m in the 16-element waveguide. (a) is the measured $|S_{11}|$, measured at one end of the MI waveguide, with a metal object moved horizontally along the array at 0.4 mm above. The $|S_{11}|$ spectra for object locations above element centres was recorded and shown. The loop antenna was placed below the centre of cell 1 to inject and receive signals. (b) is the analytically calculated reflectance $|\rho|$ at the injection point based on Eqn (115), with structure parameters for $z = 0.4$ mm from Fig. 4.2: $\kappa = -0.13$, $L_{\text{defect}} = 15.9$ nH, $f_0 = 113.4$ MHz. Reference impedance of $Z_{\text{ref}} = 4\,\Omega$ was used to match the absolute values between measured and calculated results, although we should focus on the pattern but not the absolute values of the reflectance. The white circles in both plots (a) and (b) highlight the local minima for each defect location in the spectrum to be used in our Odd-Even algorithm, which we will discuss in Section 4.3. The 'x' markers in (a) show that the mean value of the two local minima hovers around the resonant frequency f_0 shown by the dashed red line.

4.2.2 Experimental Verification

We conducted experiments to verify the analytical reflectance derived in Section 4.2.1. We used a MI waveguide array formed from 16 magnetically coupled resonators, and the details of the single unit cells were listed in Section 4.1.2, with a lattice period (centre-to-centre separation)

of 10.5 mm. We measured the first-order coupling coefficient as $\kappa \approx -0.13$, and higher-order coupling effects were neglected. The conductive object we used was the bolt head of 10 mm size described in Section 4.1.2. The object was attached to the scanning arm of the 2D scanner by plastic holders so that there were not large chunks of metal which could have significantly affected the results by introducing non-uniformity to the local electromagnetic fields.

A 4 mm-diameter magnetic loop antenna was positioned 1.6 mm below the first cell, centres aligned to excite the first cell and launch signals into the waveguide. The scattering parameter S_{11} was recorded by a VNA connected to the source loop. The metal object was scanned along the array axis, with 0.5 mm horizontal intervals, at a height $h = 0.4$ mm above the structure. This value of h resulted in a defect inductance of 15.9 nF and a defect resistance of 0.43 Ω when the centre of the bolt was axially aligned with that of a defect element. The measured S_{11} spectrum over frequency for different metal object locations is shown in Fig. 4.4 (a) as a contour plot, where the horizontal axis shows the defect location in the waveguide, and the vertical axis shows the frequency.

The measured S_{11} shown in Fig. 4.4 (a) is compared to the analytically calculated reflectance spectrum of Fig. 4.4 (b), obtained using the 'V = ZI' method. These two sets of results have a few salient features in common. First, the first element is significantly detuned when the bolt is located at position 1. In addition, a gradually increasing number of standing wave minima has been observed as the bolt is moved down the line away from the source.

A simple deduction from the results in Fig. 4.4 is that the number of local minima in the reflection spectrum may be a reliable indicator of the defect location. Although this might be straightforward if a high quality measurement of the S_{11} spectrum is available, should one seek to reduce equipment complexity and use only a narrow range of the spectrum, relying on the number of minima may not be a viable approach for localisation. Further complications arise when the interactions between the object and defect become weaker, permitting more waves to travel to the end of the line, resulting in interfering standing wave modes and thus reduced the resolvability of the minimum points.

4.2.3 Resolvability

The sensing performance of the device relies mostly on the development of the standing waves formed between the source and the defect. We may detect and determine the position of the

defect on the line if there is enough modulation of the reflectance measured at the first element. The effective maximum length of the sensing device can be determined. The standing wave patterns observed in the reflectance spectrum can not be discriminated for defect locations beyond this limit.

If we have an infinitely long sensor array, there will be no reflections from the elements beyond the defect as the MI waves keep travelling while experiencing attenuation. In such cases, the probed reflectance at the source only arises from the defect element. As the defect location becomes further away from the first element of the array, there are more supported eigenmodes within the fixed passband, leading to decreased frequency spacing between the neighbouring troughs in the reflectance spectrum. At a certain point, these local minima in the spectrum become unresolvable and we would not be able to discern the defect location based on the reflectance pattern. Additionally, as the interactions between the metal object and the defect

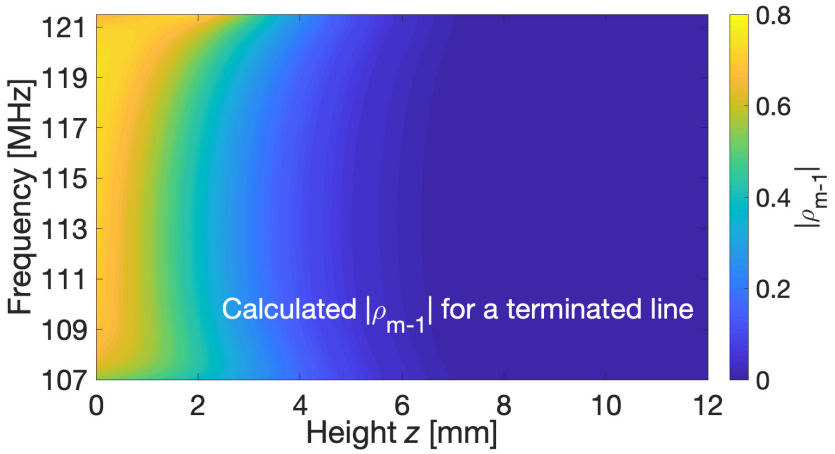


Figure 4.5: Analytically calculated variation of the reflectance from the defect, $|\rho_{m-1}|$ which is evaluated at cell $m-1$, with the height z of the metal object from the array. The resonant characteristics of the defect element follow those values shown in Fig. 4.2. A matching impedance $Z_{\mathrm{T}} = j\omega M\, e^{-jkd}$ [2] is added to terminate the end element of the 16-element array, so that the array is equivalent to an infinite line, and defect can be chosen as any cell of the line except for the two end elements.

element become weaker, for instance by increasing the height z of the object as in Fig. 4.5, the reflectance evaluated at the cell before the defect, the magnitude of ρ_{m-1} reduces and hence the depth of the troughs in the reflectance ρ evaluated at the point of excitation. The resultant resolvability of the troughs in the reflectance spectrum also reduces.

To simplify the derivations, we will begin with considering the current I hypothetically measured at the injection point, and the amount of change in the current ΔI due to the standing waves formed. The parameter that represents resolvability of the spectrum is $A = \Delta I/I$. We

will show at a later stage that this quantity A can be easily linked to the amount of change in reflectance $\Delta\rho$ (from trough to peak values) relative to the average reflectance ρ'. It was shown earlier that the standing waves result in troughs in the reflectance, and for the current spectrum on the other hand, we would observe peaks in the magnitude of the current at these frequencies that correspond to the eigenmodes.

The resolvability of the peaks is related to the width of the peak in the current spectrum, which is in turn determined by the quality factor Q of the individual resonators. Based on Eqn (106), a relationship between Q and the maximum effective size of a 1D sensing waveguide was established. As shown in Fig. 4.5, there is only a slow change, in terms of frequency, in the reflectance from the defect. Therefore, at a local maximum of the reflection spectrum and at the adjacent local minimum, the magnitudes of the reflectance are approximately the same, while there is a phase difference of π between the reflectance at these two points. We then obtained the following difference between the currents at a peak and the adjacent trough of the spectrum,

$$\Delta I = (I_0 + \rho_+ I_0) - (I_0 - \rho_- I_0) \approx 2\rho_{m-1}\, I_0\, e^{-2(m-1)\alpha d} \tag{116}$$

where I_0 represents the amplitude of the injected waves and $\rho_{+/-}\, I_0$ are based on the amplitudes of the reflected waves. $\rho_{+/-}$ are the reflectance values evaluated at frequencies corresponding to a peak and a neighbouring trough respectively. The approximation for the attenuation coefficient of MI waves in a low-loss waveguide is

$$\alpha d \approx \frac{1}{\kappa Q}\ . \tag{117}$$

The modulation depth can be defined as $\Delta I/I_0$, and a threshold value can be set for it to evaluate the ultimate usable size N_{max} of the sensing array, i.e. if defect location m is beyond N_{max}, the conductive object is not able to induce a modulation greater than the threshold value and we would not be able to localise the object. Equation (116) was rewritten, based on Eqn(117), in the following form,

$$N_{\text{max}} = 1 - \frac{\kappa Q}{2} \ln\left(\frac{\Delta I}{2\, I_0\, \rho_{m-1}}\right)\ , \tag{118}$$

As expected, objects that have weaker interactions with the defect, leading to lower values for ρ_{m-1} and thus a smaller ultimate length N_{max}.

4.3 Method for Location Identification

We devised an approach to locate the conductive object based on the dispersion characteristics of the MI waves supported by the array. For each defect position m (being any integer from 1 to 16 for our 16-element array), first we found the frequencies corresponding to the troughs in the reflectance $|\rho|$, which also corresponded to the supported eigenmodes. The local minima became unresolvable close to the edges of the passband because of the increase in attenuation of the MI waves, and we focused on the troughs near the resonant frequency close to the centre of the passband. If m is an even number, there was always a local minimum in the reflectance spectrum very close to f_0. Otherwise if m is an odd number and $m \neq 1$, we observed a relatively weak local maximum near f_0 and two troughs at frequencies approximately symmetrical about f_0. In general we used the two local minima in $|\rho|$ nearest to f_0 for localisation purposes, and these two corresponding frequencies were denoted as f_a and f_b.

4.3.1 Algorithm Based on Standing Waves

Our first attempt to localise the defect, induced by the metal object in close proximity, was to compare the difference between the two evaluated frequencies f_a and f_b,

$$\Delta f = |f_a - f_b| \ , \tag{119}$$

with the theoretically predicted values. Following Eqn (101), the analytical frequency difference between the two modes with frequencies nearest to the resonant frequency can be determined. If the object is above cell 1 or 2, the defect location could be obtained directly since no dips or only one dip (with the width and depth satisfying certain threshold conditions) would be identified within the passband. Applying such a simple localisation method on the experimental data shown in Fig. 4.4 (a), we were able to retrieve accurately the defect locations of 11 out of the 16 possible cases. The remaining 5 defect locations m were identified with errors of ± 1.

This probably was due to the fact that only first-order coupling was taken into account to obtain the analytical dispersion relationships and the eigenmodes. Higher-order coupling effects may have led to slight shifting in the dispersion relationships and the standing waves formed [63].

4.3.2 Odd-Even Algorithm

The errors in testing the standing-wave-based algorithm were within ± 1 for all the defect locations. What this meant is that some of the odd-numbered defects were identified as even-numbered defects, and vice versa. Therefore, in order to improve the results for these cases, we imposed an extra condition to categorise m as being even or odd.

This was done based on our observations of the standing wave frequencies relative to f_0 for odd or even number of elements in an array. The average of f_a and f_b was a helpful indicator - if

$$|(f_a + f_b)/2 - f_0| > \delta \ , \tag{120}$$

then m is an even number, otherwise m is an odd number. We chose $\delta = 0.53\,\text{MHz}$ as a threshold value that allowed accurate localisation up to $m = 16$. For arrays with more elements, as the MI waves propagate along the line and attenuates, the resolvability of the reflectance spectrum decreases, making it harder to identify the elements further away from the source. Structures may also exhibit significant higher-order couplings, leading to increased non-linearity in the dispersion relationships. In such cases, optimisation of the threshold value δ may be required. However, the selected threshold $\delta = 0.53\,\text{MHz}$ will be shown to suffice in our case.

Applying the additional condition prescribed by Eqn (120), the errors of localisation discussed in Section 4.3.1 were corrected, and all sixteen locations have been found accurately after testing the algorithm on both the analytical reflectance and the experimental data of S_{11} shown in Fig. 4.4. The methodology of the devised algorithm was summarised in Fig. 4.6. The limitation of this algorithm was that we only considered discrete locations of the conductive object, i.e. with the bolt centre aligned with the defect element centre for each position, and intermediate positions could be studied in the future, though requiring detailed characterisation of the system such as the effect of the defect on the mutual coupling between pairs of element that are non-identical.

When the interactions between the conductive object and the defect are strong, such as when the object is very close to the structure, the modulation in the reflectance can be clearly identified. However, when the strength of interaction reduces, the MI waves, while undergoing the attenuation, are partially reflected from the defect and partially from the end of the array. Superposition of these two reflection modes at the injection point results in more complex

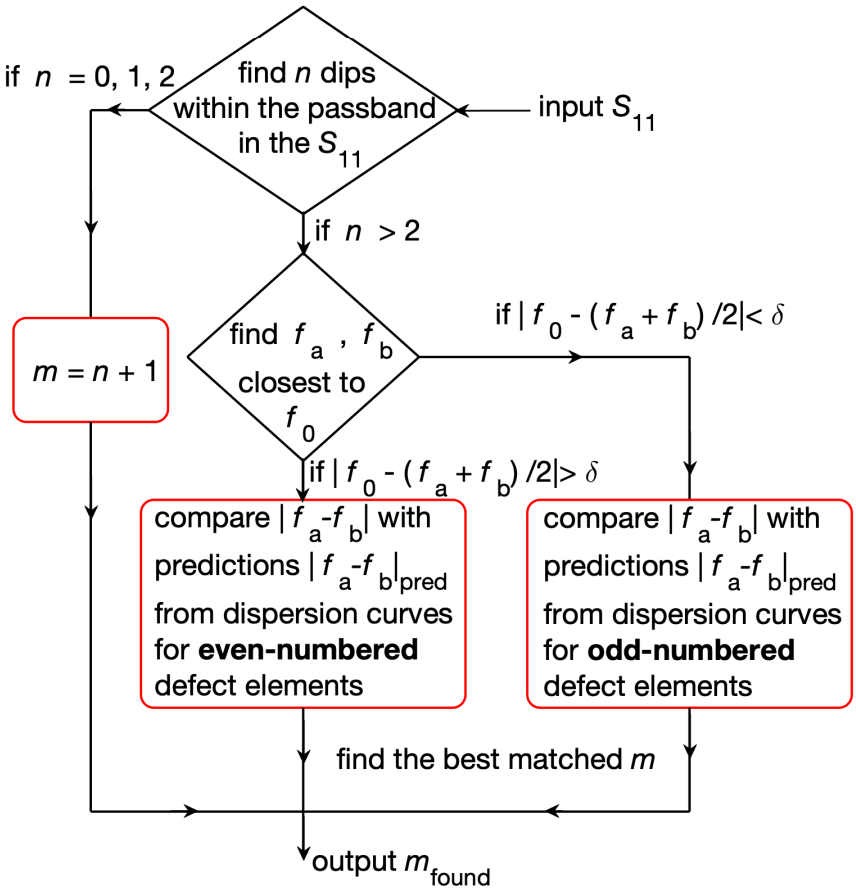
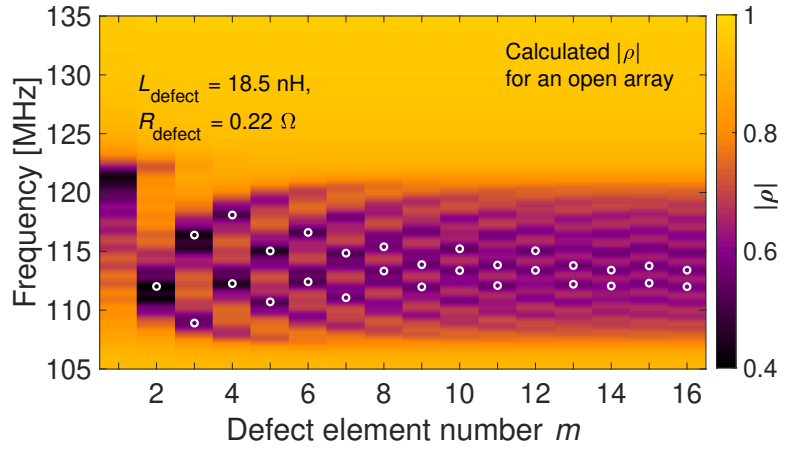


Figure 4.6: Block diagram to explain the mechanism of the Odd-Even algorithm for localising the defect element.

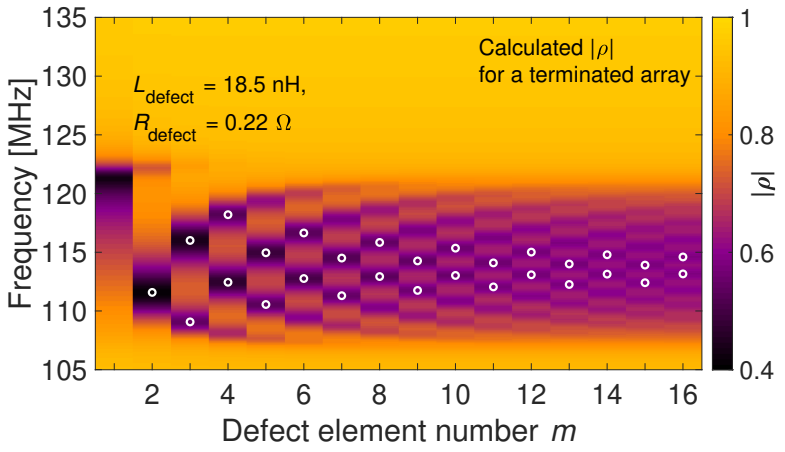
standing wave patters as shown by the analytically calculated pattern in Fig. 4.7 (a), where $L_{\text{defect}} = 18.5\,\text{nH}$ was taken. The respective resistance of the defect is $R_{\text{defect}} = 0.22\,\Omega$ (see Fig. 4.2), with this set of parameters obtained when the metal bolt was around 2 mm above the defect centre.

When $m = 2$, the minimum reflectance over frequency is 0.4 from Fig. 4.7 (a), around ten times higher than the minimum value of 0.04 at the same defect location with $z = 0.4\,\text{mm}$ from Fig. 4.4. There is now a strong background signature of the MI waves travelling beyond the defect and reflected from the far end of the line, resulting in more than 9 minima visible, interfering with the standing wave modes formed between the first element of the array and the defect element. The enhanced peaks and troughs results in shifted frequencies identified as the two local minima closest to f_0, which will increase the amount of error in applying our localisation algorithm.

One way to eliminate the interfering reflectance from the array end is to terminate the MI waveguide by an ideal matching impedance $Z_{\text{T}} = j\omega M\, e^{-jkd}$ as stated in Eqn (17) [54]. The



(a)

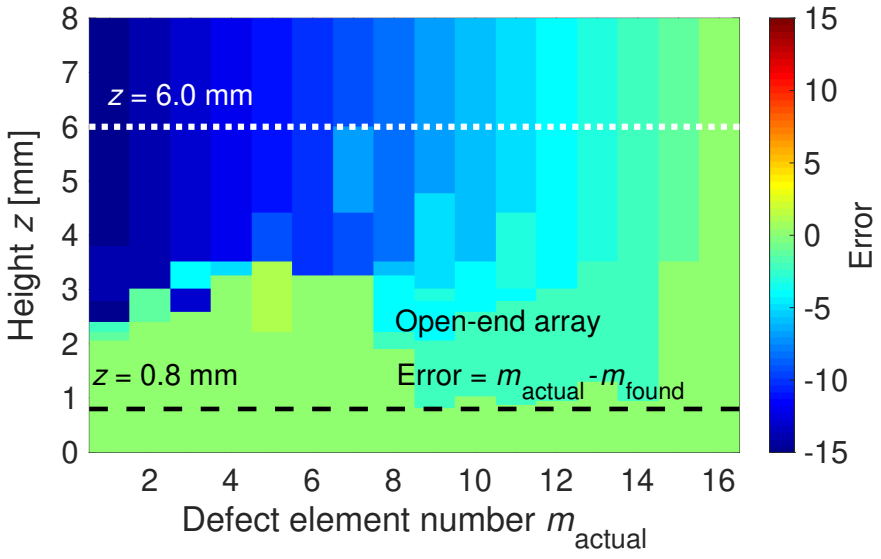


(b)

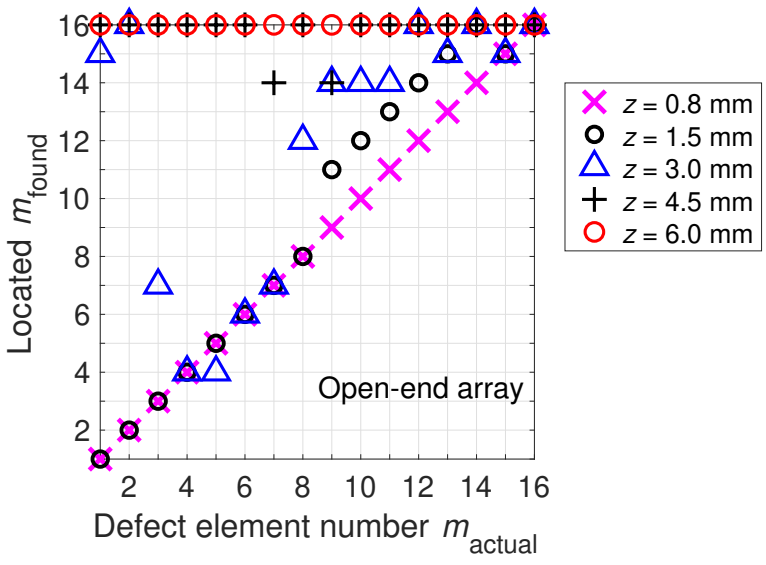
Figure 4.7: Analytically calculated reflectance $|\rho|$ over frequency for the defect being any of the 16 elements in the sensing waveguide, when the interaction between the defect and the metal object is weak. The inductance L_{defect} of the defect is chosen as 18.5 nH (recall that L_0 of an undisturbed cell is 19.7 nH). (a) is the result for a 16-element array with open ends. Superposition of the reflections from both the defect and the array end leads to unresolvable troughs in the reflectance spectrum, degrading the performance of the Odd-Even algorithm. (b) is for a line terminated with a matching impedance $Z_{\text{match}} = j\omega M\, e^{-jkd}$ to eliminate the reflected waves from the array end [54]. White circles in both plots mark the corresponding frequencies of local minima that are identified and used for the Odd-Even localisation algorithm.

resultant analytical reflectance pattern for the terminated array is shown in Fig. 4.7 (b).

The performance of the Odd-Even algorithm was tested on the analytical reflectance $|\rho|$ patterns generated using a range of defect inductance values (L_{defect} from 15 nH to the undisturbed value of 19.7 nH) to explore the impact of the partial reflectance of the defect. The resistance R_{defect} was varied from 0.5 Ω to 0.156 Ω according to Fig. 4.2 that was obtained by varying the height of the metal object above a single resonator. Localisation results from the Odd-Even algorithm are shown in Fig. 4.8 where the error $(m_{\text{actual}} - m_{\text{found}})$ between the actual

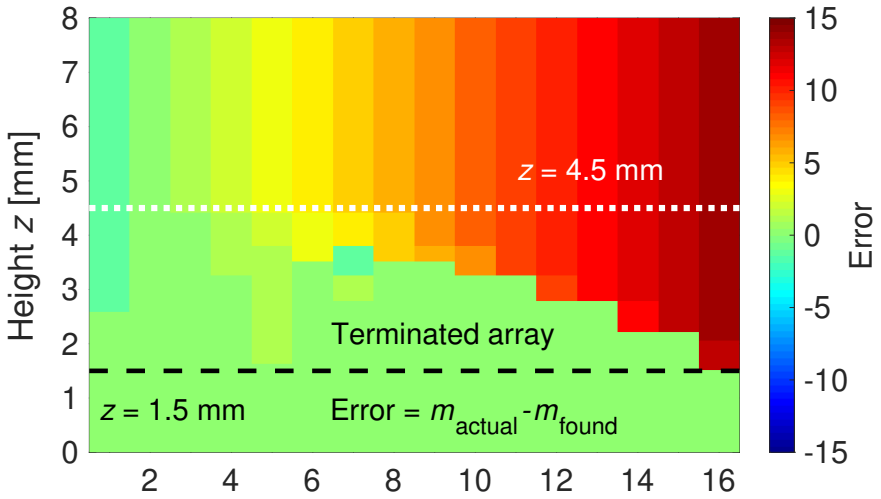


(a)

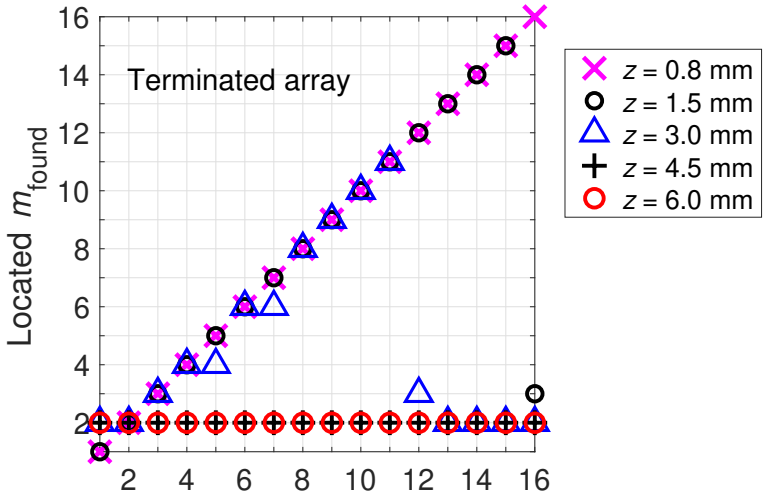


(b)

Figure 4.8: Accuracy in testing the ability of the Odd-Even algorithm to locate a metal object on a 16-element open-end array, using the analytical reflectance spectrum $|\rho|$. (a) is coloured by the error defined as $(m_{\text{actual}} - m_{\text{found}})$. When the object elevation z (as the y axis) changes from 0 to 8 mm, L_{defect} varies from 15 to nearly 19.7 nH which is the undisturbed self-inductance. Up to $z = 0.8$ mm (corresponding to $L_{\text{defect}} = 16.8$ nH, $R_{\text{defect}} = 0.36\,\Omega$), there is zero error in localisation, highlighted by the dashed black line. The dotted white line at $z = 6.0$ mm (corresponding to $L_{\text{defect}} = 19.6$ nH, $R_{\text{defect}} = 0.16\,\Omega$, very close to the unperturbed values) highlights that the algorithm completely fails and the identified object location is always $m_{\text{found}} = 16$ above this height. (b) is a parametric plot of m_{found} and m_{actual}. The case of accurate localisation is demonstrated by the magenta crosses for $z = 0.8$ mm, of which the markers fall on a straight line. If we increase z, more errors would occur, as shown by the black circle ($z = 1.5$ mm), blue triangle ($z = 3$ mm), black plus ($z = 4.5$ mm), and red circle ($z = 6.0$ mm) markers.



(a)



(b)

Figure 4.9: Accuracy in testing the ability of the Odd-Even algorithm to localise a metal object on a 16-element array with a matching termination, using analytically calculated reflectance spectrum $|\rho|$. (a) is coloured by the defined error $(m_{\text{actual}} - m_{\text{found}})$. When the object elevation z (the y axis) changes from 0 to 8 mm, L_{defect} varies from 15 to nearly 19.7 nH which is the undisturbed self-inductance. Up to $z = 1.5$ mm (corresponding to $L_{\text{defect}} = 17.8\,\text{nH}$, $R_{\text{defect}} = 0.27\,\Omega$), there is zero error in localisation, highlighted by the dashed black line. The dotted white line at $z = 4.5\,\text{mm}$ (corresponding to $L_{\text{defect}} = 19.4\,\text{nH}$, $R_{\text{defect}} = 0.17\,\Omega$, again close to the unperturbed values) highlights that the algorithm completely fails and returns $m_{\text{found}} = 2$ above this height of 4.5 mm. (b) is the relationship between m_{found} and m_{actual}. The two quantities form a straight line given accurate identification of defect locations, shown by the magenta markers. As z increases, the algorithm is less accurate, as shown by the black circle ($z = 1.5\,\text{mm}$), blue triangle ($z = 3\,\text{mm}$), black plus ($z = 4.5\,\text{mm}$), and red circle ($z = 6.0\,\text{mm}$) markers.

and derived locations is shown as a contour plot.

Figures 4.8 (a) and (b) are for the 1D structure with open ends (without terminations). Using analytical reflectance patterns calculated for a range of bolt height z, we obtained Fig. 4.8 (a) coloured by $(m_{\text{actual}} - m_{\text{found}})$ for different z and actual defect position m_{actual}. For the open array structure, we achieved accurate localisation up to $z \approx 0.8\,\text{mm}$ ($L_{\text{defect}} \approx 16.9\,\text{nH}$).

The relationship between m_{actual} and m_{found} at $z = 0.8\,\text{mm}$ is shown by the magenta crosses that fall on a straight line showing accurate identification of the defect locations in Fig. 4.8 (b) which shows the m_{found} over m_{actual} for a range of chosen z heights. The error in using the Odd-Even algorithm increases when z becomes larger, due to the weaker interactions as explained previously. The algorithm completely fails at the point of $z = 6\,\text{mm}$, giving $L_{\text{defect}} = 19.6\,\text{nH}$, rather close to the unperturbed value of 19.7 nH. In this limiting case, the array behaves as a uniform 16-element array, and there is no detectable reflection from the defect, with most of the waves travelling beyond and towards the end of the array before being reflected back. The defect location has therefore little impact on the reflectance, and the reflectance approaches that from a uniform MI waveguide, with 16 supported standing wave modes. Consequently, the defect is identified as $m_{\text{found}} = 16$ for all the actual defect locations.

Figures 4.9 (a) and (b) are for an array terminated with an ideal matching impedance $Z_{\text{T}} = j\omega M\, e^{-jkd}$. Figure 4.9 (a) shows the error $(m_{\text{actual}} - m_{\text{found}})$ as a contour plot for varying bolt height z and actual defect position m_{actual}. The defect location was identified accurately using the algorithm when the metal object was up to around 1.5 mm above the waveguide, corresponding to $L_{\text{defect}} \approx 17.8\,\text{nH}$. As the localisation error increases with increasing height z, the algorithm completely fails at the point $z = 4.5\,\text{mm}$ which gives $L_{\text{defect}} = 19.3\,\text{nH}$, too close to the unperturbed value of 19.7 nH. The reflectance is nearly smooth across the entire passband, giving only one minimum near the resonant frequency. Therefore, all defect locations were identified as position 2, as also demonstrated by the black '+' signs in Fig. 4.9 (b), which is the relationship between m_{actual} and m_{found} for several z values. When $z = 0.8\,\text{mm}$, the magenta markers fall on an oblique straight line, as there are no errors in localisation. As z increases gradually from 0.8 to 6 mm, the markers deviate from an oblique line, indicating reduced accuracy of the algorithm.

Comparing the open array with the terminated array, as the interference from the metal object becomes weaker, by increasing the z height for instance, the defect location found,

m_{found}, is generally larger than the actual position m_{actual} for the open-end array, while the opposite, $m_{\text{found}} < m_{\text{actual}}$, is true for the terminated array – shown as negative errors (blue colors) in Fig. 4.8 and positive errors (red colors) in Fig. 4.9. The explanation for this is that, the open-end array gradually approaches a uniform finite 1D array, and more MI waves are leaked beyond the defect as the impact of the metal object decreases, introducing more standing wave mode signatures to the reflectance spectrum. On the other hand, the terminated array gradually approaches an infinite array and the reflectance over frequency becomes smoother as the interactions becomes weaker, so that the algorithm identifies the defect as elements that are closer to the source.

Accurate localisation for a 16-element open array up to $z = 0.8\,\text{mm}$ ($L_{\text{defect}} = 16.9\,\text{nH}$) shows that the Odd-Even algorithm is reliable for strongly interacting objects, based on analytical reflectance patterns. Correctly terminating the line with a matching terminating improves the performance of the algorithm. The standing waves derived from the defect object dominates the reflected signals at the injection point, and accurate localisation has been achieved up to around $z = 1.5\,\text{mm}$ ($L_{\text{defect}} = 17.8\,\text{nH}$).

We could think of various applications for this position sensor based on MI waves, for instance a novel fluid level detector, by fixating a MI waveguide of similar composite cells but with the gaps of the SRRs open. The open SRRs without tuning capacitors are sensitive to dielectric objects in close proximity. A distributed metal detector embedded in a conveyor belt can be useful in production lines. Moving to larger physical scales, position detection for electric cars in charging pads can be realised as well, through wrapping the 1D structure around the wheels for monitoring the changes in the formed standing wave modes.

4.4 Summary

In this chapter we exploited the sensitivity of meta-atoms to the electromagnetic environment, and devised a method for localising a conductive object close to one of the elements in a MI waveguide. We quantised the impact of external conducting objects by modelling the change in self-inductance and resistance of the meta-atom affected. Only one input port, serving as the receiving port as well, was required for the sensing waveguide to function. We developed an Odd-Even algorithm and tested its robustness for localisation of a metal object.

Discrete locations of the metal object (above cell centres) were identified accurately based on the standing wave patterns that we observed with a single injection point, given that the interactions between the object and the defect were reasonably strong. For a 16-element waveguide with open ends, the algorithm tested on analytical reflectance spectrum gave zero error when the M6 bolt was up to $z = 0.8$ mm above a defect, which corresponded to around 15% in the self-inductance compared to the unperturbed value. The accuracy was improved further when a matching termination was added to the far end of the line, and accurate localisation was demonstrated, based on analytical reflectance spectrum, for object height up to 1.5 mm, corresponding only to around 9.6% change in the self-inductance relative to the unperturbed value.

5 Far-Field Superdirective Dimer Antenna

In this chapter we propose a rapid way of optimising the directivity of metamaterial-based endfire antenna structures with strong inter-element coupling. Dimers of magnetically coupled SRRs are studied, with only one element driven by a source. As introduced in Section 2.3.4, to realise superdirectivity using such a dimer structure, the currents in the two elements should be out of phase, and the separation between the resonators should be kept small compared to the operational wavelength. Rapid spatial variation of the currents is essential to realise superdirectivity. This is realised by imposing MI waves on the structure [63] due to the fact that MI waves have wavelength much shorter than the free-space electromagnetic waves of the same frequencies. In practical realisations, however, an accurate tuning to the optimum frequency is required, which requires lengthy measurements.

Therefore, we introduce planar equivalents to the traditional 3D directivity, defining them as the ratio of the radiated power intensity in the desired endfire direction to the average power intensity evaluated in the horizontal or the vertical (azimuthal or the elevation) plane. Analytical conditions for superdirective current distributions are derived, for both the 3D and the planar directivities. These conditions relate the quality factor of the resonators and their coupling coefficient to the array size and the operating frequency. It is demonstrated that a rapid measurement in the azimuthal plane is a reliable indicator for whether the predicted superdirective conditions for the 3D directivity have been satisfied. Numerical calculations are carried out in the microwave regime for split pipes of circular and square shapes, verifying the analytical predictions. Experimental results obtained for structures working in the GHz frequency range are, where we have obtained 2D measurements of the field distribution to demonstrate superdirectivity for the first time on a PCB structure, are summarised in Appendix (Section 7.4).

5.1 Optimisation of Superdirectivity via Planar Directivity Evaluation

A schematic diagram for two coupled capacitively-loaded SRRs modelled as two vertically oriented magnetic dipole radiators is shown in Fig. 5.1, with the two elements arranged at a separation d in the x direction. We denote the horizontal (azimuthal) plane, xy plane, as the H-plane, and the vertical (elevation) plane, xz plane, as the V-plane.

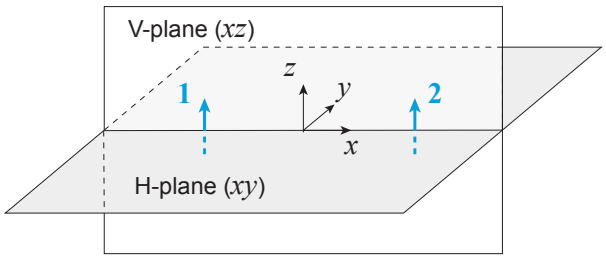


Figure 5.1: Schematic representation of a dimer of meta-atoms modelled as magnetic dipoles. Planar directivity D_{H} is evaluated in the azimuthal H-plane, and D_{V} is determined in the elevation V-plane.

The classical three-dimensional directivity is defined as

$$D_{\mathrm{3D}} = \frac{P_{\mathrm{max}}}{\langle P \rangle_{\text{solid angle}}} , \tag{121}$$

which is the ratio of the radiation power intensity in the desired direction to the power intensity averaged over the solid angle 4π. In analogy to this, we introduce planar directivity values D_{H} and D_{V} as the ratio between the power intensity in the optimum direction and the average intensity in the defined 2D planes, i.e.

$$D_{\mathrm{H}} = \frac{P_{\mathrm{max}}}{\langle P \rangle_{\text{H-plane}}} \quad \text{and} \quad D_{\mathrm{V}} = \frac{P_{\mathrm{max}}}{\langle P \rangle_{\text{V-plane}}} . \tag{122}$$

5.1.1 Optimisation of Directivity

Based on the definitions in Eqn (122), the method developed in [156] was expanded to optimise the directivity values (D, D_{V} and D_{H}) in the endfire direction corresponding to the maximum radiation intensity, and the resultant current distributions in the two coupled dipoles were derived. This compact neat approach of operating with matrices was introduced in Section 2.3.4, with a key expression of the directivity value in Eqn (66) emphasized here

$$D = \frac{\mathbf{I} B \mathbf{I}}{\mathbf{I} A \mathbf{I}} , \tag{123}$$

where $\mathbf{I} = [I_1,\ I_2]$ represented the vector of the current distribution in the two coupled dipoles, the matrix B was evaluated in the endfire direction, and the matrix A was an averaged quantity of B. The maximum radiated power intensity by the antenna structure is proportional to $\mathbf{I}B\,\mathbf{I}$, and the average power intensity to $\mathbf{I}A\,\mathbf{I}$. The averaging operation to obtain A is either performed over the solid angle 4π or over an angle 2π within the H- or V-plane, based on the type of the

directivity quantity, i.e. D, D_{V} or D_{H} :

$$A = \begin{cases} \dfrac{1}{4\pi} \displaystyle\int_0^{2\pi} \int_0^{\pi} B \sin\theta \, d\theta \, d\varphi & \text{(3D)} \\ \dfrac{1}{2\pi} \displaystyle\int_0^{2\pi} B \, d\alpha|_{\text{H-plane}} & \text{(H-plane)} \\ \dfrac{1}{2\pi} \displaystyle\int_0^{2\pi} B \, d\alpha|_{\text{V-plane}} & \text{(V-plane)} \end{cases} . \tag{124}$$

For an antenna array containing two elements, A is a 2×2 matrix, where $A_{11} = A_{22} = a$ and $A_{12} = A_{21} = b$ are its elements. After the same algebraic operations discussed in Section 2.3.4, we arrive at the following:

$$\begin{cases} a = \dfrac{2}{3}, \quad b = \dfrac{\sin u}{u} + \dfrac{\cos u}{u} - \dfrac{\sin u}{u^3} & \text{(3D)} \\ a = 1, \quad b = J_0(u) & \text{(H-plane)} \\ a = \dfrac{1}{2}, \quad b = J_0(u) - \dfrac{J_1(u)}{u} & \text{(V-plane)} \end{cases} , \tag{125}$$

where $u = kd$, $J_0(u)$ and $J_1(u)$ are the 0^{th} and 1^{st} order Bessel functions of the 1^{st} kind.

It is important to note that the current ratio between the passive and the excited element that gives us the optimum directivity values still obeys the general formula Eqn (68) derived in Section 2.3.4,

$$\left(\frac{I_2}{I_1}\right)_{\text{opt}} = \frac{a\, e^{\,ju} - b}{a - b\, e^{\,ju}} . \tag{126}$$

and the general formula for the maximum achievable directivity, under these optimum conditions, given by Eqn (70),

$$D_{\text{opt}} = 2\, \frac{a - b\cos u}{a^2 - b^2} , \tag{127}$$

Based on the respective $a,\ b$ for the different types of the directivity in Eqn (125), we are now in the position to derive analytical expressions for maximum achievable $D_{3\text{D}}$, D_{H} or D_{V} . The case that we are interested in for metamaterial-based structures has $d \ll \lambda$, i.e. $u \ll 1$. Evaluating the Taylor expansions of Eqns (126) and (127) (with respect to u), we can write the optimum

current ratio as

$$\left(\frac{I_2}{I_1}\right)_{\text{opt}} = \begin{cases} -1 - j\frac{2}{5}u + \frac{2}{25}u^2 + j\frac{323}{10500}u^3 - \frac{239}{26250}u^4 + \dots & \text{(3D)} \\ -1 - j\frac{1}{2}u + \frac{1}{8}u^2 + j\frac{1}{24}u^3 - \frac{5}{384}u^4 + \dots & \text{(H-plane)} \\ -1 - j\frac{3}{4}u + \frac{9}{32}u^2 + j\frac{61}{768}u^3 - \frac{41}{2048}u^4 + \dots & \text{(V-plane)} \end{cases}, \tag{128}$$

and the optimum directivity as

$$D_{\text{opt}} = \begin{cases} \frac{21}{4} - \frac{377}{1120}u^2 + \frac{541}{2822400}u^4 + \dots & \text{(3D)} \\ 3 - \frac{1}{6}u^2 - \frac{1}{320}u^4 + \dots & \text{(H-plane)} \\ \frac{14}{3} - \frac{35}{216}u^2 - \frac{1303}{155520}u^4 + \dots & \text{(V-plane)} \end{cases}. \tag{129}$$

It is noteworthy that, when $u \ll 1$, the optimum current distribution in all three cases shows that the currents in the two elements are almost equal in magnitude while being nearly out of phase, as expected from Eqn (126).

The variations of the optimum 3D (black), H-plane (blue) and V-plane(red) directivity values with u are illustrated in Fig. 5.2 (a). The solid curves are the exact solutions of Eqn (127), and the dashed lines are the Taylor series approximations given by Eqn (129). Figure 5.2 (b) is the phase difference between I_2 and I_1, with the value of u subtracted, so that the overall value tends to a constant for large u, with the solid curves being the exact solutions from Eqn (126) and the dashed lines based on the Taylor series expansions as shown in Eqn (128). It can be clearly seen that the Taylor series expansion offers a reasonable approximation up to $u \simeq \pi/2$, or equivalently, up to $d \simeq \lambda/4$.

The analytical optimum current distribution for a superdirective dimer is close to that of a phased array if u is large, with the phase difference between the two currents being approximately equal to u, and $D_{3\text{D}}$ hovering about the value of 3, as seen in Fig. 2.11 (b) of the current distribution for two dipoles. It is only when u becomes sufficiently small that the structure begin to exhibit superdirectivity, with all the directivity values increasing monotonically as u tends to zero as seen in Fig. 5.2 (a). The phase difference between the currents in the two coupled

elements does not equate to u when the array becomes superdirective as seen in Fig. 5.2 (b), and as u decreases it approaches π for all three types of directivity. What this means is that the currents are nearly in anti-phase, leading to destructive interference of the fields radiated by each element, which then results in superdirectivity. Figure 5.2 (c) is a parametric plot of D_{H} and D_{V} versus D_{3D}. In both the H-plane and V-plane cases, the highest D_{3D} were achieved at

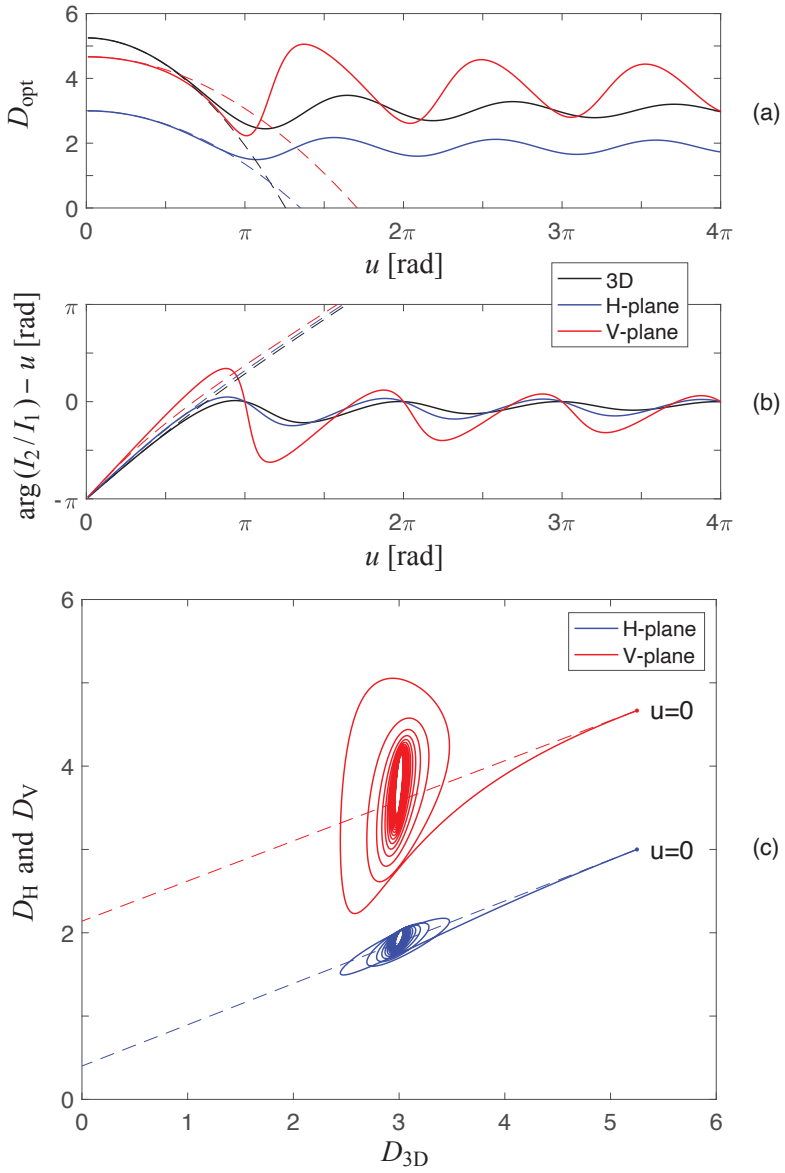


Figure 5.2: (a) Maximum achievable directivity values and (b) the phase difference between the currents in the two elements that were used to generate the directivities in (a), subtracting the value of u. The horizontal axis is u for (a) and (b). (c) Parametric plot of planar directivity values D_{V} and D_{H} (vertical axis) and the 3D directivity (horizontal axis). In all the plots, black curves refer to the 3D directivity, blue curves are for D_{H}, and red curves for D_{V}. The solid curves are the exact values, while dashed curves are from Taylor series expansion with up to the 2$^{\mathrm{nd}}$ terms.

the point where $u = 0$.

Recall that the aim of the study is to investigate whether the planar directivity quantities can be used as an indicator for the 3D directivity. The results in Fig. 5.2 are encouraging, especially as the horizontal directivity D_{H} in the H-plane can be seen to be optimised at very similar values of the currents as the 3D quantity $D_{3\mathrm{D}}$ [cf. black and blue curves in Fig. 5.2 (a)]. Therefore we conclude that in optimising the H-plane directivity, we are able to simultaneously optimise the 3D directivity.

5.1.2 Superdirectivity Conditions for Coupled Meta-Atoms

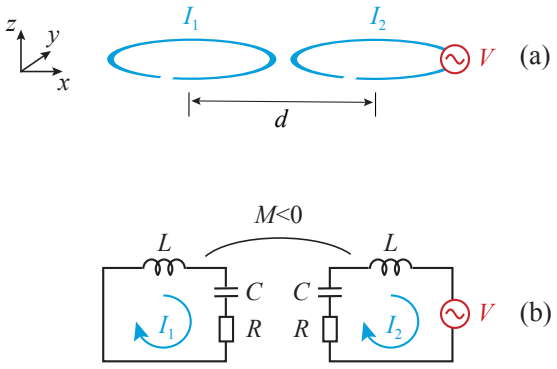


Figure 5.3: (a) A dimer structure of two coupled SRRs, where only one of the elements, element 2, is driven. (b) is an equivalent circuit model for the configuration in (a), consisting of two coupled LCR circuits.

We now adopt the technique developed in [152] of realising the desired superdirective current distribution by exciting one of the two meta-atoms, and by assigning appropriate values to the coupling coefficient κ and to the quality factor Q of the individual elements. The dipole approximation discussed at the beginning of Section 5.1 is sufficient to describe the radiative properties of the SRRs, which is shown schematically in Fig. 5.3 (a). The circuit properties of the resonators are found by modelling them as two coupled LCR circuits, with mutual inductance M. Element 2 is driven by an external voltage source of V as shown in Fig. 5.3 (b). The mutual inductance (and thus the coupling coefficient) is negative for the planar arrangements of elements.

Based on the generalised Ohm's law for the dimer structure [152], the ratio of the currents

was expressed in Eqn (13) as a function of the circuit parameters f_0, Q and κ. In order to realise superdirectivity for the dimer structure, this current ratio should be equal to the optimum current ratio as defined in Eqn (129), up to the second-order Taylor series expansion is valid for small u. We now equate the terms and look at how the superdirective optimum conditions for different directivity values compare

$$-\frac{2}{\kappa}\left(1-\nu^2-j\frac{\nu}{Q}\right)=\begin{cases}-1-j\dfrac{2}{5}u & \text{(3D)}\\[2ex] -1-j\dfrac{1}{2}u & \text{(H-plane)}\\[2ex] -1-j\dfrac{3}{4}u & \text{(V-plane)}\end{cases} \tag{130}$$

with $\nu = \omega_0/\omega$. Equating the real parts on either side of the simultaneous equations, we get the superdirective condition 1 (SD_1) showing the optimum frequency for a superdirective dimer antenna, which turns out to be identical for all three cases of interest (3D, H-plane and V-plane):

$$\frac{\kappa}{2}=1-\nu^2 \quad\Longrightarrow\quad \frac{\omega}{\omega_0}=\frac{1}{\sqrt{1-\kappa/2}} \qquad (\text{SD}_1 \text{ condition})\ . \tag{131}$$

In order to achieve the optimum directivity for all the cases, the operating frequency needs to be tuned to the frequency corresponding to the antisymmetric mode for two coupled meta-atoms at which the currents are almost out of phase [2], just as required for the destructive interference mechanism of superdirectivity.

it is an important result that the SD_1 condition is the same for all three types of directivity, verifying that by choosing the optimum frequency optimising the planar directivity, we are simultaneously optimising the 3D directivity as well. We note that the SD_1 condition is necessary but not sufficient for achieving superdirectivity with a dimer of coupled meta-atoms.

The other necessary condition is established, by equating the imaginary parts on either side of Eqn (130) and substituting the expression in Eqn (131), as

$$\frac{|\kappa|Q}{\sqrt{1-\kappa/2}} = \begin{cases} \dfrac{5}{kd} & \text{(3D)} \\ \dfrac{4}{kd} & \text{(H-plane)} \\ \dfrac{8}{3kd} & \text{(V-plane)} \end{cases} \qquad \text{(SD}_2\text{ condition)}\ , \tag{132}$$

where the fact that $\kappa < 0$ for the SRRs placed side by side in the xy plane has been taken into account. The SD_2 condition is different for the three cases, and it prescribes the required product of the κ and Q for a dimer to exhibit superdirectivity.

We have also repeated the same derivations for two coupled isotropic radiators. D_{V} and D_{H} are equal for isotropic radiators, and we found that they are optimised under the same condition $|\kappa|Q = 4/kd$ as that for the H-plane directivity of two dipoles. As shown in [152] for an isotropic dimer structure, the RHS of Eqn (132) (the 3D case) is $6/kd$, which differs from the value of $5/kd$ for dipoles. Therefore, if we were to optimise the planar directivity based on the SD_2 condition, the 3D directivity will not necessarily be optimised, and the error in determining its optimum conditions will depend on the nature of the composite elements and on their individual radiation pattern, of which the detailed discrepancies will be analysed in Section 5.1.3.

These two optimum conditions were tested based on analytical calculations, and it is shown in Fig. 5.4 that satisfying simultaneously SD_1 and SD_2 conditions does lead to superdirectivity. One set of parameters was chosen, $f_0 = 110$ MHz, $Q = 880$, $d = 24$ mm and $\kappa = -0.1$, satisfying the SD_2 condition for the 3D directivity. We plot in Fig. 5.4 the currents, including both their absolute values (a) and the phases (b), and the resulting $D_{3\mathrm{D}}$, D_{H} and D_{V} (c) as functions of frequency. It can be clearly seen that $D_{3\mathrm{D}}$ D_{H} and D_{V} reach their maximum at the same frequency very close to the lower resonance, as predicted by the SD_1 condition. The resulting optimum radiation patterns for the 3D case and the planar cases are included as insets. $D_{3\mathrm{D}}$ reaches a value of 5.24, matching the theoretical maximum achievable value for the given set of parameters. The corresponding planar directivities reach $D_{\mathrm{H}} = 2.98$ and $D_{\mathrm{V}} = 4.35$, which are also close to the theoretical maximum values.

Our findings so far support our predictions that it may be feasible to resort to simplified procedures of measuring planar directivities in optimising the superdirective structures, without

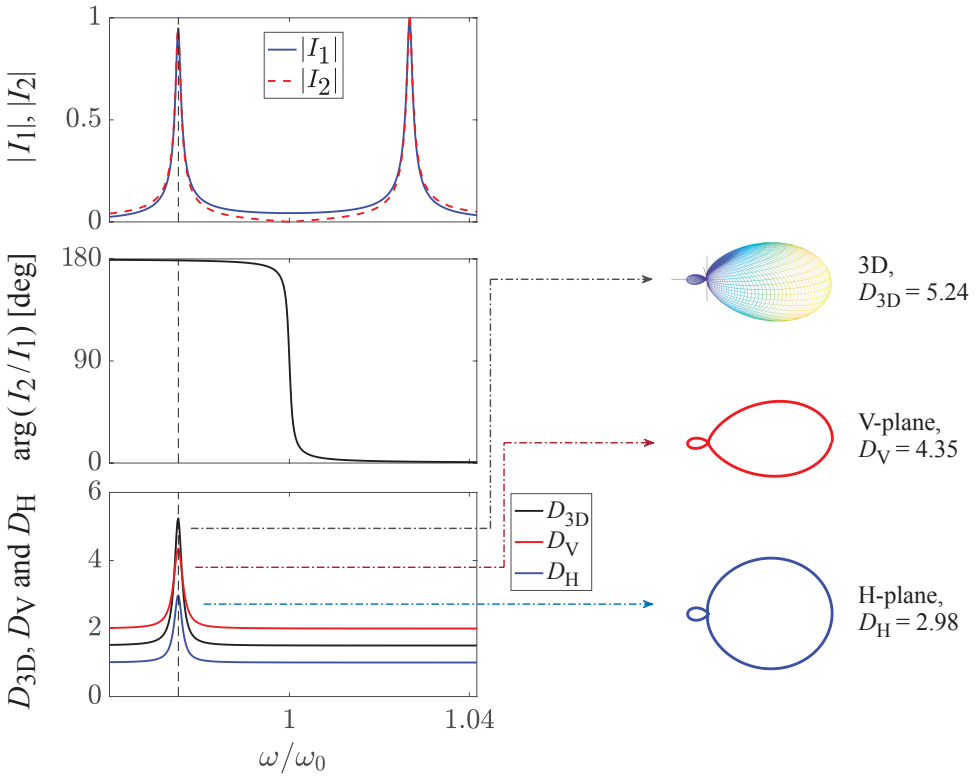


Figure 5.4: Analytically calculated variation, with frequency, of the ratio between the current magnitudes, and the phase difference between the two currents (two upper panes on the left), and the resultant directivity values (bottom left). On the right hand side, the 3D radiation pattern and cross-sections of the radiation pattern evaluated in the V- and H-plane at the optimum frequency are shown. The parameters used for the analytical calculation are $Q = 880$, $f_0 = 110$ MHz, $d = 24$ mm, $\kappa = -0.1$.

the need of evaluating the 3D radiation pattern in the lab environment.

5.1.3 Numerical Calculations

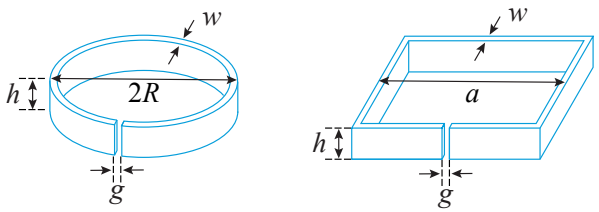


Figure 5.5: Split pipe resonators of circular and square shapes that are modelled in numerical calculations.

In order to verify the above hypothesis that, by optimisation of planar directivity we are able to optimise the 3D directivity, we performed numerical calculations for meta-atoms in CST Microwave Studio using the time-domain solver with the simulation settings described briefly

in the Appendix (Section 7.3). We modelled circular and square copper split pipe resonators shown schematically in Fig. 5.5. The sizes of these two types of resonators are equal, with $2R = a = 23$ mm, the same wall thickness$w = 1$ mm, height $h = 5$ mm and gap $g = 2$ mm. A capacitor (in the pico-Farad range, of varying values as we will investigate resonators of changing resonant frequencies f_0) is inserted into the gap of each element to tune the f_0.

The dimer antenna structure is made of two identical resonators, i.e either two circular split pipes or two square split pipes. A discrete port (current source of 1 A, while the magnitude of the current is unimportant here) was inserted into the gap of one meta-atom, exciting only one element. There is a compromise between the accuracy of the numerical calculation and its computational time, so we adjusted the local and global mesh sizes to ensure that both are reasonable. As discussed previously in [152], magnetic dipoles are only a simplified approximation to the split-pipe structures we studied, and the optimum D_{3D} values were achieved at

$$\frac{|\kappa|Q}{\sqrt{1-\kappa/2}} = \frac{4}{kd} \tag{133}$$

for both the circular and square resonators, shifted away from the analytical SD_2 condition. Due to the rotational symmetry of the electromagnetic fields radiated by magnetic dipoles in the H-plane (the plane that the resonators are placed), we expect our analytical prediction of optimum conditions in Eqn (132) for the D_H to be valid, which is identical to Eqn (133). To justify this prediction, two situations were investigated – in the first one, the element separation d was kept unchanged while f_0 of the individual elements was varied, and in the second case we have changed d while keeping f_0 constant.

To start with, the centre-to-centre separation between the two coupled resonator (either both circular shaped or both square shaped), was kept constant at $d = 24$ mm. The resultant coupling constant, calculated following the procedure detailed in [58], is $\kappa = -0.1$ for the circular dimers and $\kappa = -0.19$ for the square dimers. By choosing different values of the tuning capacitance between the split gaps, f_0 of the individual elements was varied from 50 to 150 MHz. The post-processed numerical results shown in the upper row of Fig. 5.6 are for the circular structures, and those in the lower row are for the square structures, as also indicated by the insets to the right plots.

With the variation in f_0, the dependence of the quantities $|\kappa|Q$ (black) and $4/(kd)$ (red),

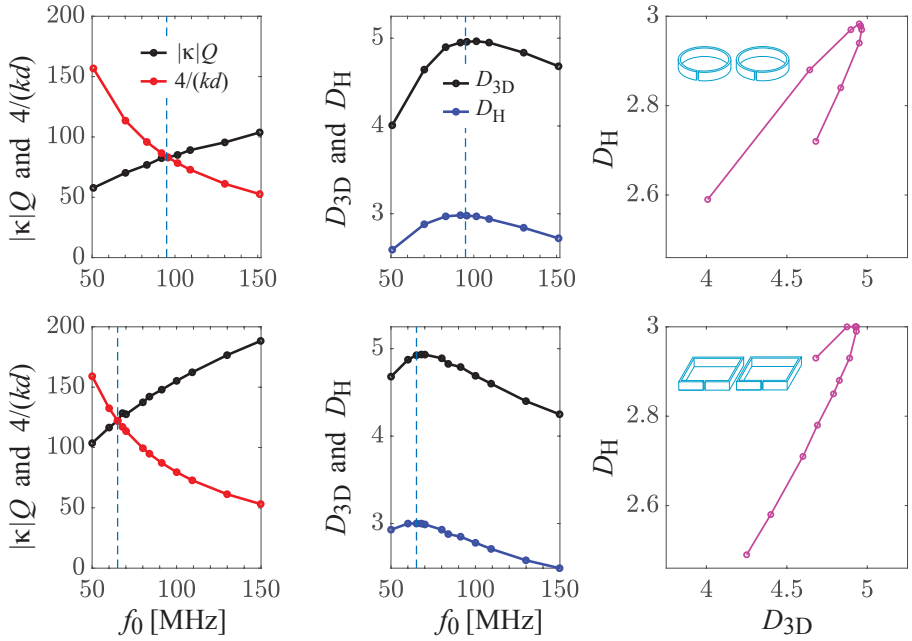


Figure 5.6: The numerical results for optimising the directivity for a dimer structure by varying the resonant frequency of the composite spit pipes. Upper row: circular resonators with size $2R = 23\,\text{mm}$, separation $d = 24\,\text{mm}$, coupling coefficient $\kappa = -0.1$. Lower row: square resonators with size $a = 23\,\text{mm}$, $d = 24\,\text{mm}$, and $\kappa = -0.19$. Left column: the variation in the LHS ($|\kappa|Q$, black) and RHS ($4/kd$, red) of the optimum condition SD_2 from Eqn (133) with f_0. The intersection between the red and black curves indicates the optimum f_0 that should give the maximum directivity. Middle column: $D_{3\text{D}}$ and D_{H} versus f_0, confirming that when SD_2 is satisfied, the maximum 3D directivity is achieved at the expected frequency. Right column: a parametric plot of D_{H} versus $D_{3\text{D}}$, showing that the maximum values are reached for both cases nearly simultaneously.

the LHS and RHS of the SD_2 condition for the H-plane case, are shown in the left column of Fig. 5.6. The dashed vertical line in each plot marks the frequency at which the curves intersect, corresponding to the optimum f_0 of the individual elements that should yield optimised superdirectivity both for the 3D and the H-plane case. The respective optimum f_0 value of the elements is 95 MHz for the circular resonators and 65 MHz for the square resonators.

The central column of Fig. 5.6 is the variation of the optimum 3D and H-plane directivity with the individual element's resonant frequency. The f_0 corresponding to the maximum point of directivity, for both $D_{3\text{D}}$ and D_{H} cases, agrees well with the predictions above based on the $|\kappa|Q$ evaluations. For the circular structure, the optimum f_0 is 92 MHz to achieve the highest D_{H} and 101 MHz for the $D_{3\text{D}}$, amounting to a 9% of difference between these two optimum frequencies. For the square elements, the optimum frequency is 60 MHz and 68 MHz for the H-plane and 3D directivity, with a 12% difference between the two.

We introduced a term ΔD as the error in an attempt to obtain the highest 3D directivity at

the H-plane optimum frequency rather than at the correct optimum frequency:

$$\Delta D = \left| \frac{D(f|_{D_{\mathrm{H,\,max}}}) - D_{\mathrm{max}}}{D_{\mathrm{max}}} \right| . \tag{134}$$

ΔD represents the actual error in the directivity itself if we were to select an optimum frequency for the composite resonators relying on planar measurements. From the data shown in the central column of Fig. 5.6, $\Delta D = 0.4\,\%$ and $0.6\,\%$ for the circular and square elements respectively - the percentage errors are very low. This robustness against variation in the resonant frequencies is desirable and is due to a flat maximum in the frequency dependence of both directivities, D_{H} and D_{3D}. In the right column of Fig. 5.6, the values of D_{3D} and D_{H} are plotted against each other as the parametric plots, emphasising that these two directivity values reach their maximum under practically the same conditions.

The conclusion from this numerical investigation is that, by optimising the H-plane directivity and tuning the resonant frequency of the composite meta-atoms until an optimum is found, we have also optimised the 3D directivity. What this procedure means in a practical environment is that lengthy 3D measurements of the radiation patterns can be avoided and only planar measurements in the azimuthal xy plane would be required. Achieving the maximum value of 3D directivity with discrepancies of less than 0.6% validates the robustness of our proposed approach.

In the second series of numerical calculations, we kept the resonant frequency f_0 unchanged and varied the separation d between the elements in the dimer antenna. Figure 5.7 is organised in the same way as Fig. 5.6, with the variable parameter being d rather than f_0. Following the plots in the left column, the LHS ($|\kappa|Q$, black) and the RHS ($4/kd$) of the SD_2 condition intersect at the optimum values of $d = 29\,\mathrm{mm}$ for the circular structure and $d = 35\,\mathrm{mm}$ for the square structure.

The variations of D_{2D} and D_{H} with d are shown in the central column of Fig. 5.7. For the circular dimers, the H-plane directivity reaches its maximum value at $d = 30\,\mathrm{mm}$, and 3D directivity reaches maximum at $d = 29\,\mathrm{mm}$, confirming the optimum value of separation as predicted by the condition displayed in the left column of Fig. 5.7. For the square elements, the optimum d is 36 mm and 35 mm for the H-plane and 3D directivity, respectively. In both the circular and square configurations, there is roughly a 3% error in the optimum d found for the

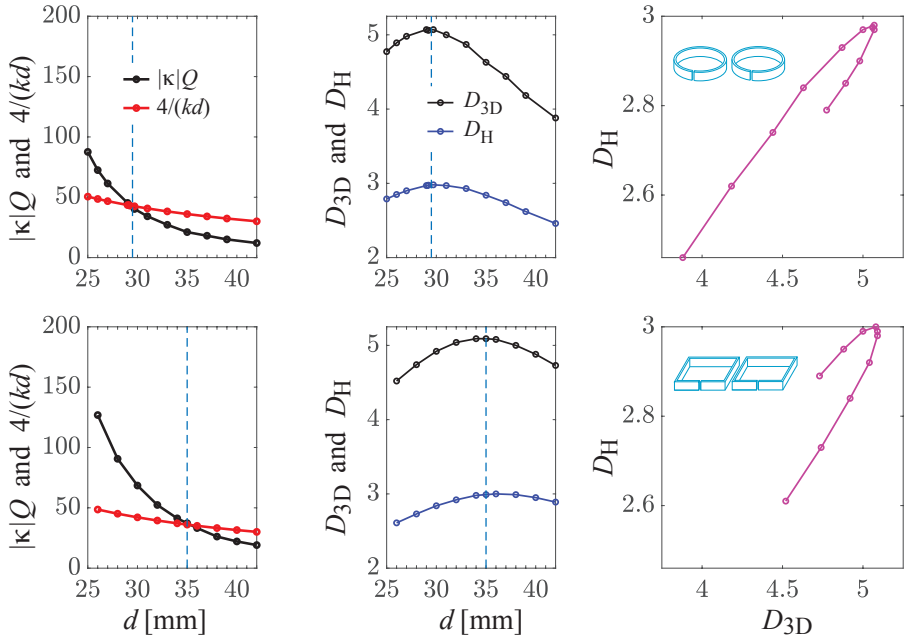


Figure 5.7: The numerical results for optimising the directivity of dimer structures through changing the separation between the two coupled resonators. Upper row: circular resonators with size $2R = 23\,\text{mm}$, resonant frequency $f_0 = 150\,\text{MHz}$, and quality factor of individual elements $Q = 1000$. Lower row: square resonators with size $a = 23\,\text{mm}$, $f_0 = 150\,\text{MHz}$, and $Q = 750$. Left column: the variation in the LHS ($|\kappa|Q$, black) and RHS ($4/kd$, red) of the optimum condition SD_2 from Eqn (133) with d. The intersection between the red and black curves indicates the predicted optimum separation of the two elements. Middle column: $D_{3\text{D}}$ and D_{H} versus d, confirming that when SD_2 is satisfied, the maximum 3D directivity is achieved at the predicted separation from the left column. Right column: a parametric plot of D_{H} versus $D_{3\text{D}}$, showing that the maximum values are reached for both cases nearly simultaneously.

planar and 3D directivity. Based on the error definition in Eqn (134), the resulting percentage error in searching for the optimum $D_{3\text{D}}$ is estimated to be very low, less than 0.2% for both configurations.

We conclude that the optimisation of the H-plane directivity would have enabled us to identify the best configuration (with optimised 3D directivity) with respect to the distance between the coupled elements of the dimer, and that this conclusion is not affected by the shape of the meta-atoms.

Relying on the in-plane measurements of the radiated field distribution, we demonstrated superdirectivity for the first time using a PCB dimer structure in [167], and the paper is attached in the Appendix (Section 7.4).

5.2 Summary

In this chapter we explored a superdirective dimer structure of two strongly coupled split ring resonators. The fast spatial variation in the currents in each element, due to the supported MI waves, led to the superdirective behaviour. With the aim to characterise and optimise the superdirective dimer antennas, while avoiding lengthy 3D measurements, we introduced planar directivities in both the azimuthal and the elevation plane as equivalents of the 3D directivity. We developed analytical conditions for optimising the directivities, and predicted that by optimising the azimuthal directivity we would have optimised 3D directivity as well. This was verified by numerical calculations for split pipes operating in the MHz frequency range. Experimental demonstration of superdirective PCB dimer antennas was carried out for the first time, and the results were presented in the Appendix (Section 7.4).

We expect that our approach would be suitable for meta-atoms of different shape. In particular, with the advent of additive manufacturing, 3D-printed meta-atoms gain in importance and our method would enable rapid evaluation of the superdirective performance of 3D-printed arrays and would aid rapid prototyping of 3D-printed arrays with radiative properties on demand.

6 Conclusions and Future Work

This DPhil thesis studies the properties of MI waves and proposes novel applications relying on the manipulation of MI waves in metamaterial-based structures. The key results and potential future research directions are identified in this chapter.

In **Chapter 3** we proposed to control the direction of guided signals in MI arrays using two coherent excitation sources with a $\pi/2$ phase difference. Analytical predictions and experimental validation were performed in the MHz frequency range, where point source approximations are easier to realize in practice. Moving to higher frequencies, we demonstrated the same principle by analytical calculations and finite element simulations on structures operating in the THz frequency range, where electric coupling dominates and EI waves are supported. It was shown that the selective direction of the signal propagation depended on whether the supported waves were forward or backward waves. When the sources were separated by two cells, two branches were created within the passband, with the upper branch supporting backward waves and the lower one supporting forward waves. Opposite directions of selective signal-guiding were achieved for these two branches. Such a system can be interpreted as a special case of the diatomic structure, with two identical elements in each cell. Analytical models for diatomic structures were justified by the experimental results.

Future research as an extension of this work include

- to demonstrate the controllable direction of wave suppression or propagation using general diatomic structures, such as one made from two shifted identical lines coupled to each other, or coupled planar-axial structures described in [57]. Methods to excite two diatomic cells need to be devised so that only one element in each of the diatomic cell is excited - for example by selecting a source location for it to couple with one of the elements, while the coupling between the source loop and the other element in the cell is close to zero. Based on the dispersion relationships of diatomic structures, analytical predictions can be compared with experimental results.

- to extend the 1D MI waveguide to a 2D metasurface supporting MI waves, and explore the possibility of guiding the signals to realise near-field directionality on a surface, which would be useful in wireless power or data transfer applications. Applying one excitation source to the centre of a 2D metasurface would result in symmetric propaga-

tion of signals. There will be more freedom in choosing the location for a second source, and the possibility of applying excitation, with a phase difference, to another element of the surface with the aim to break the symmetry of the guided MI waves on the surface can be explored.

- to demonstrate experimentally the signal suppression effects for waveguides operating in the THz frequency range. The experiments discussed in Chapter 3 were based on structures with passband in the microwave frequency range, where point source approximations are valid. To validate the proposed method of wave suppression in higher frequency ranges, potential options that can approximate point sources are fluorescent molecules or nanoparticles. However, one should also devise methods to have two coherent sources with controllable phases.

In **Chapter 4** we presented a novel metamaterial sensing MI waveguide for localisation of a metal object in close proximity. Based on the propagation of supported MI waves, reflectance of the injected waves due to the defect created by the presence of the metal object was analytically calculated and verified by experimental results. A low-complexity algorithm for discrete localisation of the object was developed based on the standing wave modes formed, and unambiguous localisation was shown for a range of interaction strengths between the defect and the object. Improved accuracy of the algorithm due to a matching termination added to the array end was discussed. This investigation of a 1D MI waveguide serves as a starting point for developing sensors based on MI waves.

The 1D analysis can be extended to devise 2D sensing surfaces, and there are a few other directions for future research

- to localise a conductive object with its size larger than that of the unit cells. The variations in the resonant characteristics of multiple defect elements affected by the object need to be quantised. The mutual coupling between the defects also should be characterised. While it may be possible to exploit superposition to deal with objects larger than one unit cell, this is likely to be quite limited by the strength of interaction between the object and the cells. The sensor can also be designed to detect foreign objects of various materials. A dielectric object, for example, can be detected and located by measuring S_{11} from a 1D structure consisting of open split ring resonators. The capacitance of unloaded resonators

changes with the proximity of a dielectric object.

- to explore the possibility of multi-object localisation. This may only work if the interactions between the objects and the defects are reasonably weak, and signals can propagate beyond one defect before being partially reflected at the next defect. Superposition of the standing wave modes formed due to the different defects would increase the difficulty for localisation, and one possible approach is to take into account the phase, rather than only the magnitude, of the reflectance spectrum in the algorithm. Machine learning techniques and non-uniform structure designs may also be useful in such cases. Localisation based on time-domain analysis has recently been explored by our group [168], and we were able to locate multiple defects on the structure. Group velocity were evaluated based on the dispersion relationships of the MI waves. The time taken for the reflected echoes from both the defects and from the end of the array can be used to accurately locate multiple defects, and the reflection coefficient allow evaluation of the proximity of the conductive object based on a library of analytical reflection coefficients with varying defect positions.

- to address the tolerance of the sensing structure in practice. We were able to conclude based on our first investigations that the Odd-Even algorithm works well on our measured data sets. In [63], the tolerances of transmission in a MI waveguide has been discussed. The elements in the waveguide were non-identical by varying the additional capacitance C in a random fashion. The resultant frequency shifts in the supported standing wave modes (or eigen-modes), as well as the reduction in the achieved power transfer caused by a 5% random variation in C were not drastic. As the Odd-Even algorithm we developed and discussed here mostly rely on the analytical prediction of the standing wave modes, we expect that our structure also bears a tolerance of at least 5% change in the capacitances without affecting its sensing performance. The impact of waveguide bending on the supported MI waves was discussed in [169]. Bending our 1D waveguide uniformly should not have much impact on its sensing performance, as the mutual coupling between adjacent cells is expected to change by the same amount for every adjacent pair, leaving us with a uniform array. The change in higher-order coupling effects, though probably inevitable, could be kept low with careful designs of the structure. One could

explore potential designs of the sensing array as a flexible structure like that in [170], so that the flexible hinges between the cells ensure that the nearest-neighbour coupling coefficient is unchanged while the shape of the bent array changes. Under such conditions, the properties of the waveguide will be almost unaffected by bending. However, as pointed out in [63], other wave properties of the MI waveguide could be more sensitive to manufacturing imperfections and tolerances, which should be addressed with careful analysis for practical uses.

In **Chapter 5**, a rapid way in optimisation of metamaterial-based superdirective dimer antenna with strong coupling was proposed. Superdirectivity can be realised by exciting one of the two elements, imposing MI waves on the dimer structure, We introduced new planar equivalences defined in similar ways to the traditional 3D directivity. Optimum conditions to realise superdirectivity were derived for magnetically coupled SRR dimers that can be modelled as two dipoles, for both the planar and 3D directivity values. These theoretical superdirective conditions provided a recipe for optimising the directivities. As predicted by analytical derivations and verified by numerical simulations in the MHz frequency range that, a rapid measurement of the planar directivity in the azimuthal plane is shown to be a reliable characterisation of the directive system, and thus useful in optimising its superdirective performance. We also demonstrated for the first time of a PCB rapid prototyping for such superdirective structures.

Future work include

- to verify the proposed method experimentally, a fully functioning 3D antenna characterisation system with rotational holders of a receiving antenna is needed for measurements of the far-field radiation pattern produced by the superdirective structures. Both the measurement time and the resolution of the 3D measurement should be reasonable. The physical limitations of the anechoic chambers should be taken into consideration for far-field measurements, otherwise transformations between near-field and far-field radiation patterns can be considered, so that the field distribution can be measured in the near-field range.

- to consider complex modes of coupling, including the electric interactions, between the resonators in the dimer antenna. For simplification, the MHz dimer structure was modelled as two coupled magnetic dipoles, which is reasonable since the tuning capacitors

added to the resonators' gaps predominantly contain the electric fields. However, the long wavelengths of the MHz antennas may cause issues if the space in experimental environment is limited, and also the fact that the radiation resistance of electrically-small structures is very low would mean that far-field measurements are difficult. Moving to higher frequency ranges, such as for the GHz structures, retardation effects come into play and both magnetic and electric interactions should be taken into account.

- to expand the analysis of a dimer structure to antenna arrays of larger sizes, and for composite meta-atoms of various shapes – rigorous derivations of superdirective conditions should be followed by careful tuning of the resonators in order to realise superdirective current distributions. This could potentially enable rapid characterisation and prototyping of 3D-printed resonators designed to have specific radiation properties.

In summary, we demonstrated various applications using metamaterial-based structures thanks to the tailorability of the MI waves.

7 Appendices

7.1 Higher-Order Coupling Effects

The dispersion equation taken into account up to N^{th} order interactions is [63]

$$\sum_{n=1}^{N} \kappa_n \cos(nkd) = -\left(1 - \frac{j}{Q}\frac{\omega_0}{\omega} - \frac{\omega_0^2}{\omega^2}\right) , \tag{135}$$

as discussed in Section 2.3.2. The expansion of $\cos(nkd) = \cos(nu)$, with $u = k\,d$, is an n^{th}-order Chebyshev polynomial of u. Therefore the LHS of Eqn (135) can be written as a polynomial for u of order N, with real coefficients if κ_n are assumed to be real. If $N = 2$, Eqn (135) becomes

$$2\kappa_2 \cos^2(u) + \kappa_1 \cos(u) - \kappa_2 + 1 = \frac{\omega_0^2}{\omega^2} + \frac{j\,\omega_0}{Q\,\omega} . \tag{136}$$

To obtain the dispersion characteristics, we solve Eqn (136) for the relationship between u and ω (and thus between k and u). The second-order polynomials on the LHS indicates that there are two solutions to the equation, being a pair of complex conjugate. Recall that $k = \beta - j\,\alpha$, the complex solutions with large imaginary values (α) are waves that decay fast and do not propagate along the structures, also termed as the evanescent waves.

Taking into account odd number of interaction modes in the coupling effect resolves the issue, and an example with third-order coupling is shown below in Fig. 7.1. Based on Eqn (135), third-order coupling effects gives a third-order polynomial on the LHS of the equation, giving, within the passband, one almost real solution (it will be purely real under lossless conditions meaning that the RHS of Eqn (135) is purely real) and two other solutions forming a complex conjugate pair. The three supported modes by the hypothetical structure with $\kappa_1 = -0.13$, $\kappa_2 = -0.01$, $\kappa_3 = -4.2 \times 10^{-3}$ is shown in Fig. 7.1, demonstrating that the first mode (blue) is the dominant mode, with the lowest attenuation, accompanied by two complex modes (shown in red and black) featuring a significantly higher attenuation across the entire passband.

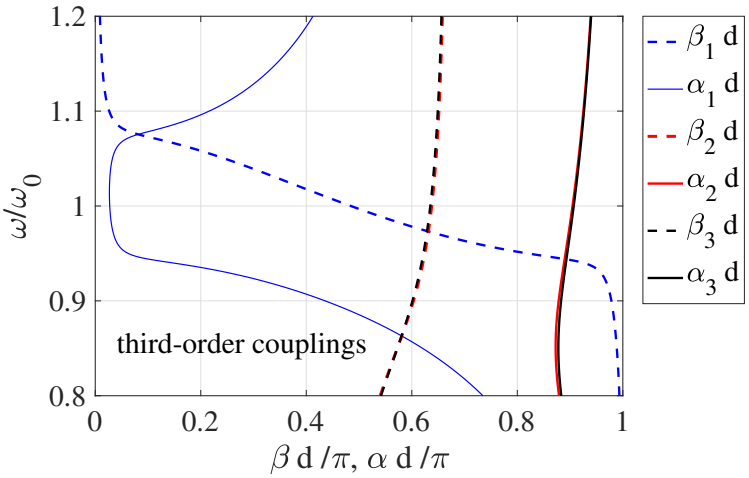


Figure 7.1: Dispersion characteristics for a MI waveguide with up to the third-order coupling, $\kappa_1 = -0.13$, $\kappa_2 = -0.01$, $\kappa_3 = -4.2 \times 10^{-3}$. The dashed curves are the propagation coefficient β, and the solid curves are the attenuation α. The first mode (blue) is the dominant mode, with the higher-order modes (black, red) being evanescent and decaying rapidly.

7.2 Visualisation of Magnetic Fields

Given the current flowing in a conductor, the resultant magnetic field **B** at any point in space can be determined based on the Biot-Savart law, which for a homogeneous current I along path c is

$$\mathbf{B}(\mathbf{r}') = \frac{\mu_0 I}{4\pi} \int_c \frac{d\mathbf{l} \times \mathbf{r}'}{r'^3} , \tag{137}$$

where $d\mathbf{l}$ is the infinitesimal length element on the current path, $\mu_0 = 4\pi \cdot 10^{-7}$ is the vacuum permeability, and $\mathbf{r}' = \mathbf{r} - d\mathbf{l}$ is the vector from the current element to the point of field evaluation. In this thesis, we restrict the filament current models to be planar, i.e. their composite filaments all lie in one plane and do not extend into space.

We can rewrite Eqn (137) as

$$\mathbf{B}(\mathbf{r}') = \frac{\mu_0 I}{4\pi} \int_c \frac{r' \sin\theta dl}{r'^3} , \tag{138}$$

and based on (as in Fig. 7.2)

$$r' = \frac{r_x}{\sin\theta} , \tag{139}$$

and with $\varphi = \pi/2 - \theta$

$$dl = r_x \sec^2\varphi d\varphi , \tag{140}$$

substituting the above expressions into Eqn (138), we then get

$$\mathbf{B}(\mathbf{r}') = \frac{\mu_0 I}{4\pi r_x} \int_{\alpha}^{-\beta} \cos\varphi \, d\varphi \ . \tag{141}$$

For a filament positioned in the xy plane along the x direction, carrying current and its ends

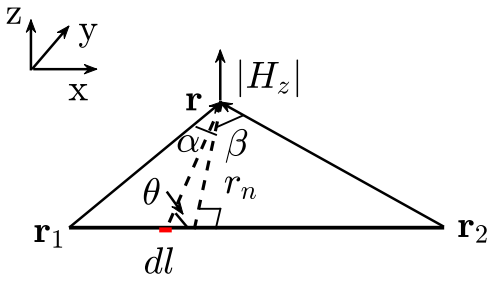


Figure 7.2: Illustration of a filament in the x direction, defined by $\mathbf{r}_1$ and $\mathbf{r}_2$, and the point of field evaluation is $\mathbf{r}$. The normal distance from $\mathbf{r}$ to the filament is termed as r_n.

defined by vectors $\mathbf{r}_1$ and $\mathbf{r}_2$ with coordinates $(x_1,\, y_1,\, z_1)$ and $(x_2,\, y_2,\, z_2)$ the magnetic field $|H_z|$ at a point $\mathbf{r}$, of coordinates $(x,\, y,\, z)$ in space, as illustrated in Fig. 7.2, is given by

$$|H_z| = \frac{I}{4\pi r_n} \left(\sin\alpha + \sin\beta\right) \cos(\gamma) \ , \tag{142}$$

where γ is the angle between the magnetic field at the evaluation point $\mathbf{r}$ and the z axis, α is the angle between $\mathbf{r} - \mathbf{r}_1$ and $\mathbf{r}_2 - \mathbf{r}_1$, and β is the angle between $\mathbf{r} - \mathbf{r}_2$ and $\mathbf{r}_1 - \mathbf{r}_2$ as shown in Fig. 7.2. For a current filament not parallel to the x direction, a transformation of both the filament and the $\mathbf{r}$ for the evaluation point is required, and is done by multiplying all three vector $\mathbf{r},\ \mathbf{r}_1,\ \mathbf{r}_2$ by a rotational matrix

$$A = \begin{pmatrix} \cos(\theta) & \sin(\theta) & 0 \\ -\sin(\theta) & \cos(\theta) & 0 \\ 0 & 0 & 1 \end{pmatrix} \ , \tag{143}$$

where θ is the angle between the filament and the x axis.

We start with a filament current of finite length (10 mm) and show the produced magnetic field in a selected plane parallel to the filament. It's assumed that the filament carrying a current $I = 1\,\mathrm{A}$ is in the xy plane, and only the magnitude of the normal z component of the field, $|H_z|$ in an xy plane 1 mm above the filament is shown for illustration. The normalised field

pattern is shown in Fig. 7.3. There is zero (dark blue) field component right above the filament which is marked by the white dotted line. The field component reaches its maximum next to the centre of the filament (at $x = 5$ mm) since the strength of the magnetic field is the sum of the field from infinitesimal current elements on the filament.

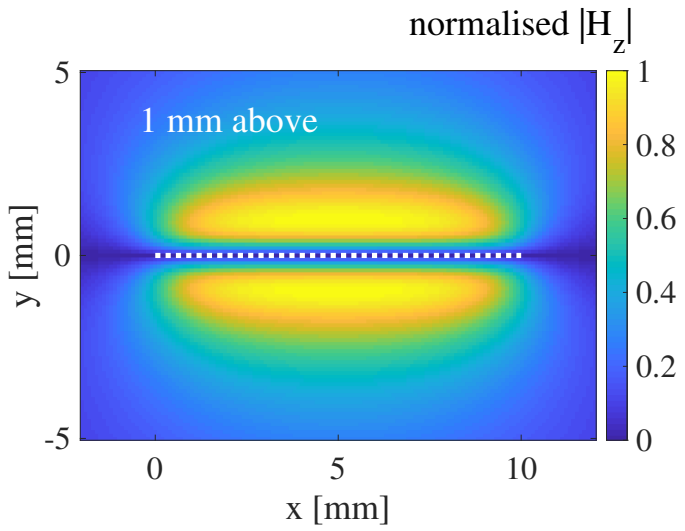


Figure 7.3: Normal component of a magnetic field $|H_z|$ produced by a filament of 10 mm length (white dotted line), assuming uniform current distribution. The field is evaluated in a $x - y$ plane 1 mm above the filament, and the field is normalised to its maximum value.

The field produced by a square loop filament structure, of size 10×10 mm and with a uniform current distribution, is our next example, and the evaluation plane is 1 mm above the filament loop in Fig. 7.4 (a), and 10 mm above the filament loop in Fig. 7.4 (b). It is seen that when the evaluation plane is close to the structure, the maximum magnetic field is inside and close to the corners of the loop (white dotted lines), as the summation of the contributions from the uniform current elements is dependent on the geometry. When the evaluation plane is 10 mm above, with the lifted height comparable to the structure size, the shape of the loop is 'blurred' out and the maximum $|H_z|$ is above the centre of the loop. The field produced by a circular structure such as that discussed in Chapter 3 can be obtained by first approximating the circular SRR as a filament current circular loop. This is a reasonable approximation as presented in [61]. The circular loop filament is then discretised into short filament sections of finite length. Increased number of sections leads to increased accuracy of the results. We chose to consider 31 sections along the circumference of the circular loop and reasonable results were obtained that matched with numerical calculations.

An additional step was to take into account inhomogeneous current distributions. The non-

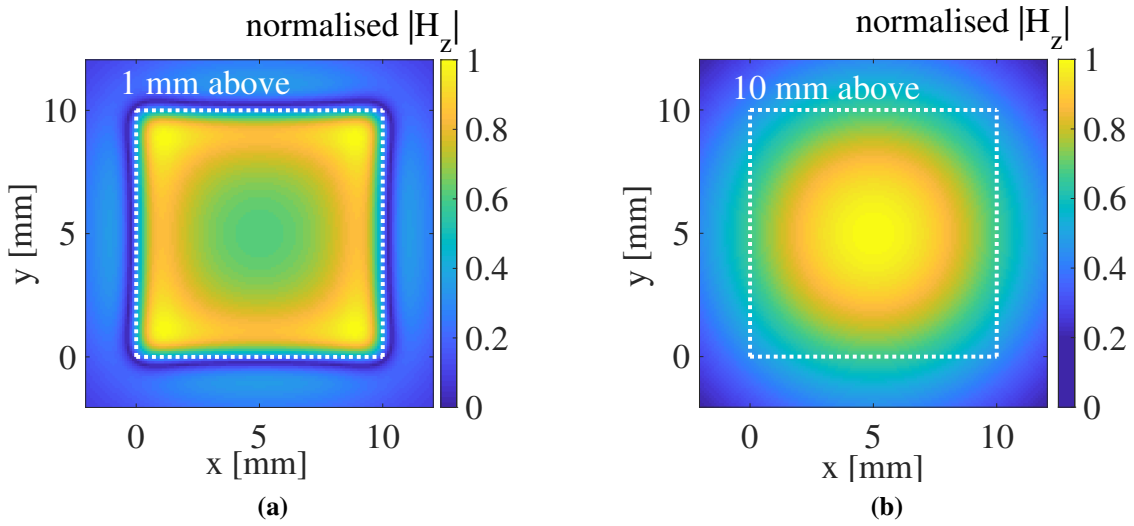


Figure 7.4: Normal component of a magnetic field $|H_z|$ produced by a filament square loop of 10 mm on a side (white doted lines), with uniform current distribution. The evaluation plane for field calculation is xy planes being (a) 1 mm above the filament loop, and (b) 10 mm above the filament loop.

uniform current has spatial dependence shown in Eqn (87) and the modification is to make Eqn (142)

$$\delta |H_z| = \frac{I(\theta)}{4\pi r_x} (\sin\alpha + \sin\beta) \quad , \tag{144}$$

where $I(\theta)$ is the current density in the filament section, and the angles α and β are still defined relative to the filament section.

The resultant field distribution by the a circular loop filament with a split gap, modelling the SRR discussed in Chapter 3 is shown in Fig. 7.5, with the local minimum shown at the position of the SRR gap, and maximum near the middle of the circumference.

7.3 Numerical Calculation Setup in CST

Numerical simulations were carried out in the CST Microwave Studio which uses finite integration technique (FIT, related to the FDTD) for its transient (time-domain) solver and finite element method (FEM) for its frequency domain solver.

To simulate structures in the MHz frequency range, the time-domain solver was used (CST 2017). Open boundary conditions was set for far-field simulations, the mesh properties were set to be those shown in Fig. 7.6 for reliable results. In setting up the MHz simulation, the number of time pulses for maximum solver duration was set to be 200 pulses for reaching a steady state. This number may be redundant and can be reduced but gave reliable results in our

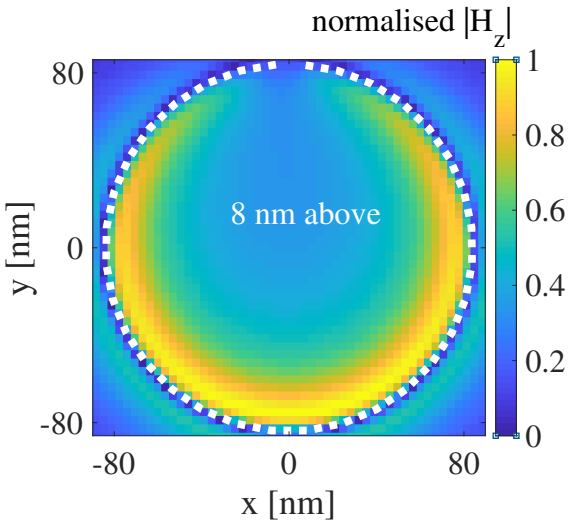


Figure 7.5: Normal component of a magnetic field $|H_z|$ produced by a circular filament to approximate an SRR (80 nm radius and 12 nm gap, marked by the white dotted curve), with the plane of evaluation being 8 nm above the structure.

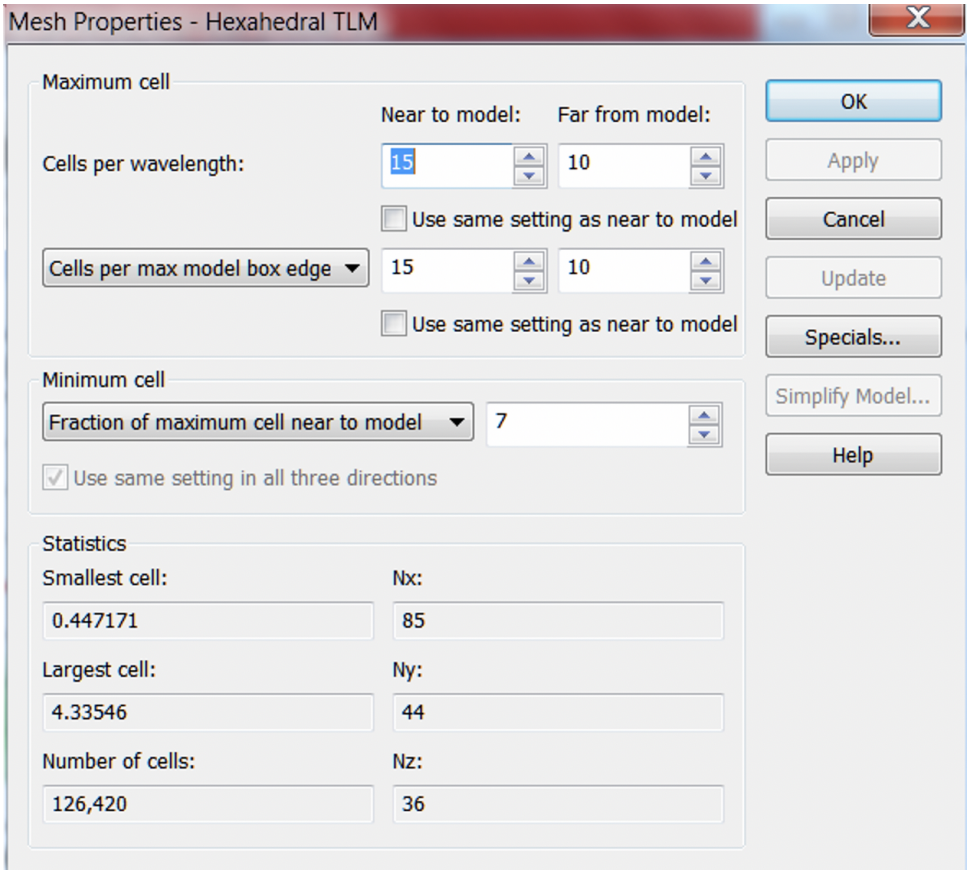


Figure 7.6: Caption of CST (2017) for global mesh property settings in the numerical calculation of a dimer of two SRRs tuned to have resonance in the MHz frequency range.

work.

The numerical calculations for the THz arrays presented in Chapter 3 had two sources

applied simultaneously to the waveguide array. This was done by enabling the simultaneous excitation option in the solver set-up window, where the phase difference of 90 degrees and the relative magnitudes of the two applied sources were input as controllable parameters. Due to the large array size (27 elements compared to the size of two elements for the MHz structure), local mesh properties were tailored to obtain reliable results while keeping the computational time acceptable.

7.4 Demonstration of Superdirectivity

Please refer to the next page for the attached paper.

Demonstration of Superdirectivity for PCB Split Ring Dimers

J. Yan[1], A. Radkovskaya[2], A. Vallecchi[1], C. J. Stevens[1] , E. Shamonina[1]
[1] Department of Engineering Science, University of Oxford, Oxford, OX1 3PJ, UK
[2] M.V. Lomonosov Moscow State University, Faculty of Physics, Magnetism Department, Leninskie Gory, Moscow 119992, Russia
jiaruo.yan@wadham.ox.ac.uk

***Abstract*— We have designed and tested a Metamaterial Superdirective Antenna (MSA). The MSA was fabricated using PCB technique and comprised a pair of split ring resonators (SRRs). It achieved high directivity with a compact design which is easy to manufacture. Superdirectivity was predicted by simulations and verified by experimental results. The coupling between the SRR's was varied to maximize directivity. The potential for designing the MSA to any operating frequency was explored.**

Index Terms*— Linear arrays, superdirective arrays, electrically small antennas, split ring resonators, printed circuit board (PCB).*

I. Introduction

Uzkov has shown in 1946 [1] that the directivity of a linear array of isotropic elements can approach a maximum value of N^2 in the end-fire direction, if the elements are properly excited and as the elements spacing approaches zero. Superdirectivity is defined here as any directivity value above that achievable by a phased array of the same size (around 3 for a two-element array) and which would require a an inter-element separation of $\lambda/2$. Superdirectivity relies instead on fast spatially varying current distributions along a closely spaced antenna array.

Coupling between the unit cells in metamaterials made of resonant coils gives rise to magnetoinductive waves [2]. Such slow waves make it possible to realize the current distribution required for superdirectivity [3]. It was predicted theoretically in [3] and [4] that far-field superdirective behavior is realizable for arrays of two and three identical split ring resonators (SRRs). A relationship between the coupling constant κ, the quality factor Q, the free-space wavelength λ and the separation d between the SRRs is derived analytically in [3]. Reference [5] reports both simulation and experimental results that rigorously demonstrate superdirectivity for an array of two split pipes. Split pipe refers to a section of copper pipe with a radial cut to form a parallel gap. The split pipes are oriented such that their gaps are aligned with the array axis, facing the same direction. Exploiting a similar concept, the feasibility of superdirective meta-arrays of nanoscale SRRs at optical telecommunication wavelengths has been recently demonstrated in [6].

The analytic relationship for κ, Q , λ and d explained in [3], although necessary, is not sufficient for realizing superdirectivity. Indeed, the orientation of the split rings is important in achieving high directivity [7]. The relationship between far-field radiated power and the orientation of the two identical split rings has been derived analytically in [7]. A comprehensive series of simulations has been carried out to generate maps of maximum achievable directivity for all possible orientations of SRRs. The conclusion of [7] is that, the "CC" configuration (as in the orientation of split rings adopted in this paper and illustrated in the next section) is the only one for the PCB SRR dimer structure that leads to superdirectivity. In this paper, the superdirective performance of an MSA is studied, both numerically and experimentally. The effect of coupling strength is addressed.

II. Simulations

We investigated the MSA by simulations using CST Microwave Studio. The structure is shown in Figure 1.

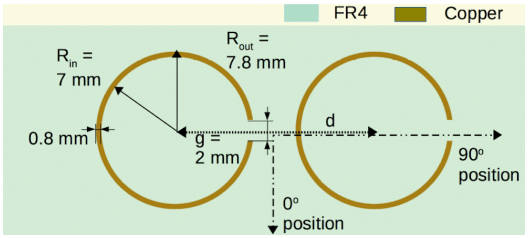


Figure 1. MSA structure, with the parameters defined. The 90° and 0° rotational positions are labeled on the graph.

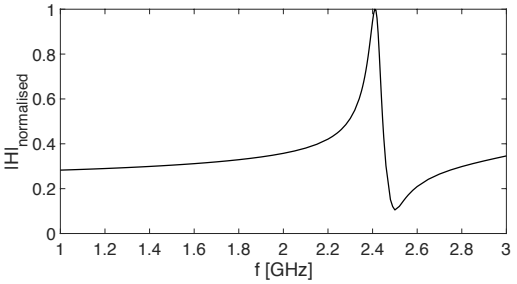


Figure 2. Field strength simulated over frequency to identify resonance of a single SRR with parameters: R_o = 7.8 mm, R_{in} = 7 mm.

The outer radius R_o is 7.8 mm, the inner radius R_{in} is 7 mm, the gap is 2 mm in both rings, and the separation is d (in section II - C, the effect of d on the performance of the structure is investigated). FR4 substrate of 0.8 mm thickness and copper track of 35 µm thickness was chosen both in numerical calculation and in experiments. The feeding source was modelled as a small magnetic loop placed behind element 1 in Figure 3.

The simulated resonant frequency f_0 of the single split ring structure is 2.41 GHz, as shown in Figure 2, and the relative quality factor Q is approximately 35. The resonance was determined by probing the magnetic field at the centre of a single excited SRR. The resonant frequency is the frequency corresponding to the strongest magnetic field strength simulated. The directivity for a single split ring is around 1.6, which is close to that of a dipole.

A. *Superdirectivity*

The radiation pattern for the MSA of antenna parameters: R_o = 7.8 mm, R_{in} = 7 mm, d = 19 mm is shown in Figure 3.

Element 1 in Figure 3 is excited while element 2 acts as a parasitic element, as well as a reflector. The radiation pattern for the MSA is shaped like a balloon with the highest radiation intensity pointing in the same direction of at which the excited element is facing: the 90° position in Figure 1. There is no side lobe. The directivity of the antenna is 4.507, very close to the optimum value of 5.1 for two split rings at the given separation.

The electric field pattern is plotted based on the simulation result. The direction of highest $|E|$ is at approximately 90°, shown by the dark red region in Figure 4. Nevertheless, maximum directivity is reached at a slightly lower frequency than that of maximum $|E|$ and corresponds instead to the two dark blue regions, in the field map.

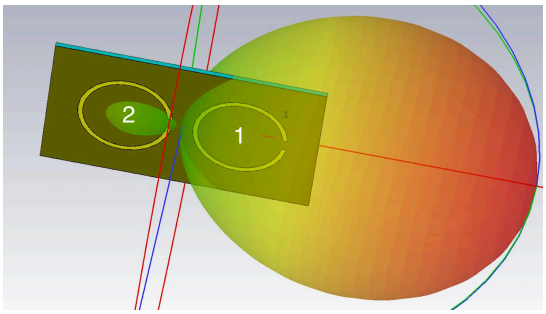


Figure 3. Radiation pattern at the frequency of the highest directivity, f = 2.363 GHz, D = 4.507. Antenna parameters: Ro = 7.8 mm, Rin = 7 mm, d = 19 mm.

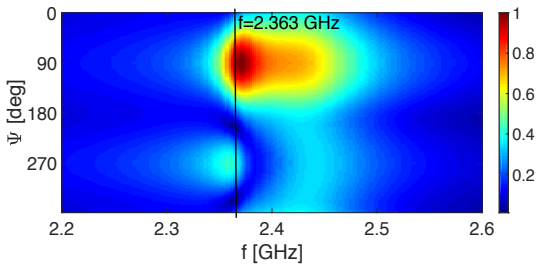


Figure 4. Simulated normalized $|E|$ pattern in the plane of the MSA over frequency. The highest directivity is at 2.363 GHz, marked by the solid black line. Antenna parameters: Ro = 7.8 mm, Rin = 7 mm, d = 19 mm.

For omnidirectional antennas, similar plots of field pattern as in Figure 4 would be uniform strips along the y-axis while the strength of the field (the color of the strips) changes along the x-axis.

B. *Current Distribution*

For superdirectivity to exist, the currents in the split rings are required to be approximately out of phase and of comparable magnitude. These conditions are met for the structures simulated, and the current distribution against frequency in the MSA of d = 19 mm is displayed in Figure 5.

C. *Variation in separation*

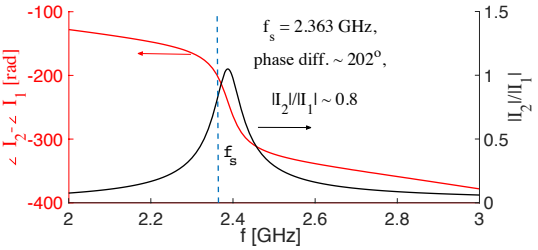


Figure 5. The current ratio and phase difference over frequency for the MSA of antenna parameters: Ro = 7.8 mm, Rin = 7 mm, d = 19 mm.

We investigated the influence of separation d in the antenna performance. The separation d was varied from 17 mm to 23 mm while the geometry and dimensions of the SRR's were kept unchanged.

For a set of dimers with the same unit-cell geometry, the separation d between the split rings affects both the f_s and the highest D, where f_s is the frequency corresponding to the highest D for an antenna. There are three noteworthy features in Figure 6:

1) As d increases, D decreases. For greater d, the coupling between the two SRRs becomes weaker. The current distributions deviate more from the optimum condition than

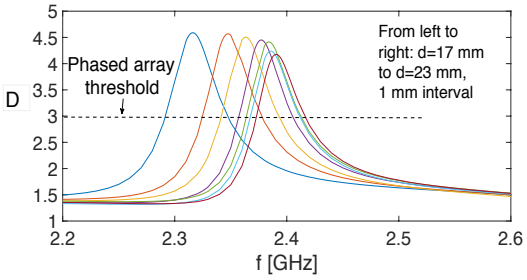


Figure 6. Directivity (linear) over frequency for a range of separations, antenna parameters: R_o = 7.8 mm, R_{in} = 7 mm, d=17,18,19…23 mm for the curves from left to right.

those for the smaller separation. The conditions for superdirectivity [2] were satisfied to a higher degree of accuracy by the structure with smaller d. This led to a lower D for larger d. The maximum achievable D is about 4.6.

2) As d increases, f_s increases and becomes closer to the resonant frequency f_0 of a single SRR. For two SRRs next to each other, the resonance splits into two resonant modes: an anti-symmetric mode and a symmetric mode. Maximum D is achieved at a frequency very close to the lower resonance which corresponds to the anti-symmetric mode. As d increases, the coupling strength between the elements decreases, which results in less splitting of the resonant peaks. Therefore, this lower resonance becomes closer to the f_0 (2.41 GHz).

3) Even though the maximum directivity of the dimer structure decreases as d increases, the MSA remains superdirective. Especially from d = 17 mm to d = 21 mm for which the frequency corresponding to highest D is increasing, there is no significant decrease in maximum D. This observation opens the possibility of a tunable superdirective dimer structure with a comparatively flat directivity performance over a certain frequency range. By controlling the coupling strength between unit cells, the operating frequency of the split ring antenna can be tuned while remaining highly directive.

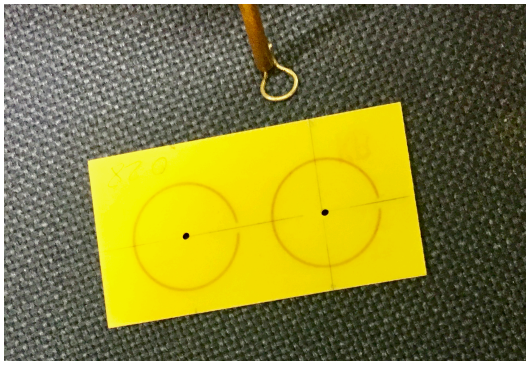


Figure 7. Photo of the manufactured MSA. The tracks are the printed split rings. Also shown is the 6 mm loop probe used to excite the MSA.

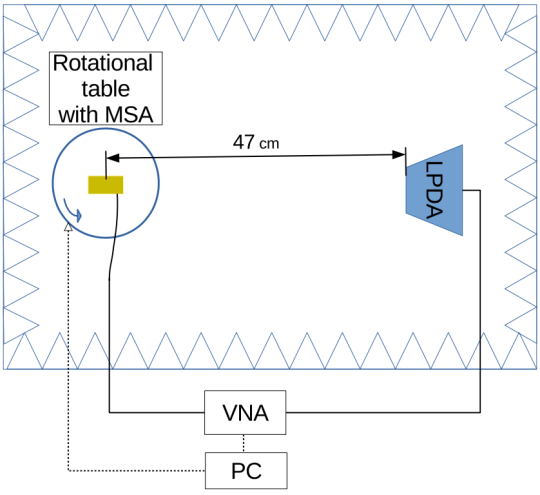


Figure 8. Schematic diagram of the experimental setup in the anechoic chamber. The yellow solid rectangle represents the MSA placed on a nonmetallic stand at the center of the rotational table. Figure 8 is a zoom-in diagram showing the relative orientation of the excitation probe and the MSA.

III. EXPERIMENTS

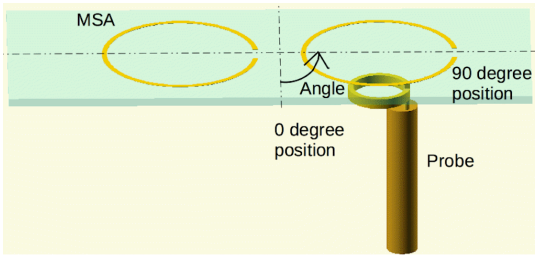


Figure 9. Exciting one of the two SRR in the MSA by placing a loop probe below the center of the SRR. Also shown is the rotational angle position: 90° position is when the gaps of the SRR's are facing the LPDA which is placed in the anechoic chamber as in Figure 7.

The MSA was commercially fabricated (PCBway Ltd.) using the standard procedure. One of the fabricated model is shown in Figure 7.

Measurements of the field pattern were made in an anechoic chamber. The system of the experiment is shown in Figure 8.

The MSA is mounted onto a motored rotational table controlled by a computer. The stand holding the MSA is made of a nonmetallic material. Figure 9 depicts how the excitation loop probe is placed under the centre of one of the SRRs. The excitation source (probe) is placed approximately 2 mm below the first element and connected to one channel of the vector network analyzer (VNA). The rotational axis is in between the two split rings, which is 47 cm away from the front-end of a log-periodic dipole antenna (LPDA) receiving the signal. This corresponds to 3-5 wavelengths. The LPDA is connected to the other channel of the VNA. The LPDA only detects in-plane signal components and is placed approximately at the same height with the PCB antenna.

In-plane S_{21} is proportional to $|E|$ and this was measured by the VNA. Measurements were made with 1601 frequency points and for orientations from 0° to 360° in steps of 5°. Background signals (with no PCB split ring dimers put in the anechoic chamber) corresponding to all rotational angles were obtained at the beginning of the experiments and repeatedly measured throughout the measurements when configurations were changed. The background signals were subtracted from the corresponding measurements with the split ring antenna on the stand.

A. Field Pattern and Superdirectivity

The measured resonant frequency f_0 of a single split ring is 2.31 GHz, lower than the numerically calculated value. This value is obtained by measuring the S_{21} against the frequency with the method described in [8] and marking the resonance.

The quality factor Q is estimated to be 29. The split ring can be modelled as an LC circuit, the resonant frequency of which is $1/\sqrt{(LC)}$.

The measured in-plane field pattern is shown in Figure 10. In comparing Figure 10 and Figure 4, all significant features are preserved:

1) There are the dark blue (minimum) and the dark red area (maximum) at very close frequencies. One difference is a shift of the frequency at which dark blue and red patterns appear. The measured frequency of highest D is expected to be lower than the simulated f_s, resulting from the shift in self-resonance.

2) The maxima occurs at 90° position. The maximum radiation direction is aligned with the gaps of the SRR's, which is the same as in the simulations. There is another local maxima at approximately 270° position, both in the simlated and measured patterns. This corresponds to the backward radiation.

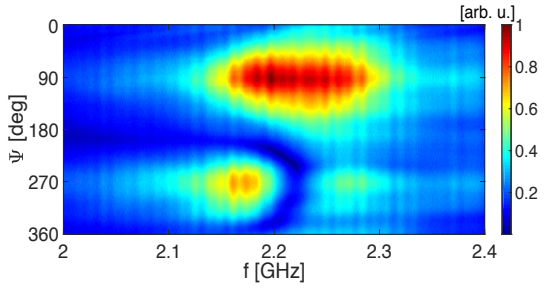


Figure 10. Normalized $|E|$ (linear) pattern over frequency, Ro = 7.8 mm, Rin = 7 mm, d = 19 mm.

3) The frequencies of the dark red (maximum) and dark blue (minimum) regions are lower than the measured resonance (2.31 GHz). And this lower resonant mode is the antisymmetric mode as explained in section II-C. The same conclusion can be drawn from the simulated 2D pattern.

Based on the above observations and comparisons to the simulation results, it can be concluded that the MSA can achieve superdirectivity at the lower resonant mode.

IV. Conclusion

We have successfully demonstrated that the MSA exhibits robust superdirective behavior. This has been studied in simulations and the result has been verified by experiments. The use of PCB fabrication technique makes the manufacturing process much simpler and more precise compared to that of the split pipe dimer antenna previously demonstrated to be superdirective.

The effect on the achievable directivity (maximum D = 4.6) of varying the distance and thus the coupling strength between the split rings for this PCB structure has been investigated numerically. In particular, it has been shown that by adjusting the coupling strength, it is possible to maintain high directivity while tuning the operating frequency by 4% (100 MHz). Future studies will explore ways of adjusting the coupling strength to design a tuneable superdirective antenna, for example by using flexible dielectric substrate to control the separation between the array elements.

Acknowledgment

Support from SYMETA project (EPSRC grant EP/N010493/1) and OXIMETA as well as fruitful discussions with the group members are gratefully acknowledged.

References

[1] A. I. Uzkov, "An approach to the problem of optimum directive antenna design," C.R. Dokl. Acad. Sci. USSR, 53, 1, pp. 35–38, 1946.

[2] L. Solymar and E. Shamonina, *Waves in Metamaterials*. Oxford University Press, Oxford, 2009.

[3] E. Shamonina, L. Solymar, "Superdirectivity by virtue of coupling between meta-atoms," 7th International Congress on Advanced Electromagnetic Materials in Microwaves and Optics – Metamaterials 2013, Bordeaux, France.

[4] E. Shamonina and L. Solymar, "Superdirective 'meta-molecules'," in Proc. 8th Int. Cong. On Advanced Electromagnetic Metamaterials in Microwaves and Optics, Aug. 25-30, Copenhagen, Denmark, 2014.

[5] A. Radkovskaya, A. Vallecchi, L. Li, G. Faulkner, C.J. Stevens, E. Shamonina, "Experimental demonstration of superdirectivity for coupled dimers of meta-atoms," 10 th International Congress on Advanced Electromagnetic Materials in Mocrowaves and Optics – Metamaterials 2016, Crete, Greece. [Conference paper and conference presentation]

[6] A. Vallecchi, C. J. Stevens, E. Shamonina, "Superdirective meta-arrays at telecommunication wavelengths," Loughborough Antenna and Propogation Conference (LAPC) 2017, Loughborough, UK, 13-14 Nov. 2017.

[7] A. Vallecchi, L Li, C. J. Stevens, E. Shamonina, "Mapping directivity of coupled dimers of Meta-stoms," 11 th International Congress on Engineered Material Platforms for Novel Wave Phenomena - Metamaterials, Marseille, France, 2017.

[8] T.Hao, C.J. Stevens and D.J. Edwards, "Optimisation of metamaterials by Q factor," Electronics Letters, 26th May 2005, 41. 653 - 654. 10.1049/el:20051428.

References

[1] R. Marques, F. Martín, and M. Sorolla, *Metamaterials with Negative Parameters: Theory, Design and Microwave Applications*, Wiley, Hoboken, 2008.

[2] L. Solymar and E. Shamonina, *Waves in Metamaterials*, Oxford University Press, Oxford, 2009, 2014.

[3] R. A. Shelby, D. R. Smith, and S. Schultz, Experimental verification of a negative index of refraction, *Science* **292**, 77 (2001).

[4] E. Yablonovitch, Photonic band-gap structures, *J. Opt. Soc. Am. B* **10**, 283 (1993).

[5] K. Busch and S. John, Liquid-crystal photonic-band-gap materials: The tunable electromagnetic vacuum, *Phys. Rev. Lett.* **83**, 967 (1999).

[6] S. Wood, J. Fells, S. Elston, and S. Morris, Wavelength tuning of the photonic band gap of an achiral nematic liquid crystal filled into a chiral polymer scaffold, *Macromolecules* **49**, 8643 (2016).

[7] Z. Liu, X. Zhang, Y. Mao, Y. Y. Zhu, Z. Yang, C. T. Chan, and P. Sheng, Locally resonant sonic materials, *Science* **289**, 1734 (2000).

[8] H. Chen and C. T. Chan, Acoustic cloaking in three dimensions using acoustic metamaterials, *Appl Phys Lett* **91**, 183518 (2007).

[9] X. Ao and C. T. Chan, Far-field image magnification for acoustic waves using anisotropic acoustic metamaterials, *Phys. Rev. E* **77**, 025601 (2008).

[10] J. Li, L. Fok, X. Yin, G. Bartal, and X. Zhang, Experimental demonstration of an acoustic magnifying hyperlens, *Nat. Mater.* **8**, 931 (2009).

[11] J. U. Surjadi, L. Gao, H. Du, X. Li, X. Xiong, N. X. Fang, and Y. Lu, Mechanical metamaterials and their engineering applications, *Adv. Eng. Mater.* **21**(3), 1800864 (2019).

[12] B. Florijn, C. Coulais, and M. van Hecke, Programmable mechanical metamaterials, *Phys. Rev. Lett.* **113**, 175503 (2014).

[13] G. N. Greaves, A. L. Greer, R. S. Lakes, and T. Rouxel, Poisson's ratio and modern materials, *Nat. Mater.* **10**, 823 (2011).

[14] S. Babaee, J. Shim, J. C. Weaver, E. R. Chen, N. Patel, and K. Bertoldi, 3D soft metamaterials with negative Poisson's ratio, *Adv. Mater.* **25**, 5044 (2013).

[15] V. M. Shalaev, W. Cai, U. K. Chettiar, H.-K. Yuan, A. K. Sarychev, V. P. Drachev, and A. V. Kildishev, Negative index of refraction in optical metamaterials, *Opt. Lett.* **30**, 3356 (2005).

[16] W. Cai and V. M. Shalaev, *Optical Metamaterials*, Springer, 2010.

[17] L. Tonks and I. Langmuir, Oscillations in ionised gases, *Phys. Rev.* **33**, 195 (1929).

[18] W. Rotman, Plasma simulation by artificial dielectrics and parallel-plate media, *IRE Trans. Antennas Propag.* **10**, 82 (1962).

[19] G. H. B. Thompson, Unusual waveguide characteristics associated with the apparent negative permeability obtainable in ferrites, *Nature* **175**, 1135 (1955).

[20] J. B. Pendry, A. J. Holden, D. J. Robbins, and W. J. Stewart, Magnetism from conductors and enhanced nonlinear phenomena, *IEEE Trans. Microw. Theor. Technol.* **47**, 2075 (1999).

[21] A. Schuster, *An Introduction to the Theory of Optics*, Edward Arnold, London, 1904.

[22] L. I. Mandelshtam, Group velocity in crystalline arrays, *Zh. Eksp. Teor. Fiz.* **15**, 475 (1945).

[23] V. G. Veselago, The electrodynamics of substances with simultaneously negative values of ε and μ, *Sov. Phys. Usp.* **10**, 509 (1968).

[24] D. R. Smith, W. J. Padilla, D. Vier, S. C. Nemat-Nasser, and S. Schultz, Composite medium with simultaneously negative permeability and permittivity, *Phys. Rev. Lett.* **84**, 4184 (2000).

[25] K. Li, S. McLean, R. Greegor, C. Parazzoli, and M. Tanielian, Free-space focused-beam characterization of left-handed materials, *Appl. Phys. Lett.* **82**, 2535 (2003).

[26] J. B. Pendry, Negative refraction makes a perfect lens, *Phys. Rev. Lett.* **85**, 3966 (2000).

[27] S. A. Ramakrishna and J. B. Pendry, The asymmetric lossy near-perfect lens, *J. Mod. Opt.* **49**, 1747 (2002).

[28] G. Gomez-Santos, Universal features of the time evolution of evanescent modes in a left-handed perfect lens, *Phys. Rev. Lett.* **70**, 077401–1 (2003).

[29] W. Cai, D. A. Genov, and V. M. Shalaev, Superlens based on metal-dielectric composites, *Phys. Rev. B* **72**, 193101–1 (2005).

[30] P. Alitalo, C. Simovski, A. Viitanen, and S. Tretyakov, Near-field enhancement and subwavelength imaging in the optical region using a pair of two-dimensional arrays of metal nanospheres, *Phys. Rev. B* **74**, 235425–1 (2006).

[31] G. Dolling, C. Enkrich, M. Wegener, J. F. Zhou, C. M. Soukoulis, and S. Linden, Cut-wire pairs and plate pairs as magnetic atoms for optical metamaterials, *Opt. Lett.* **30**, 3198 (2005).

[32] K. Aydin, I. Bulu, and E. Ozbay, Subwavelength resolution with a negative-index metamaterial superlens, *Appl. Phys. Lett.* **90**, 254102 (2007).

[33] M. G. Silveirinha, P. A. Belov, and C. R. Simovski, Subwavelength imaging at infrared frequencies using an array of metallic nanorods, *Phys. Rev. B* **75**, 035108–1 (2007).

[34] V. M. Shalaev, W. Cai, U. K. Chettiar, H.-K. Yuan, A. K. Sarychev, V. P. Drachev, and A. V. Kildishev, Negative index of refraction in optical metamaterials, *Opt. Lett.* **30**, 3356 (2005).

[35] S. A. Cummer, B.-I. Popa, D. Schurig, D. R. Smith, and J. Pendry, Full wave simulations of electromagnetic cloaking structures, *Phys. Rev. E* **74**, 036621–1 (2006).

[36] D. Schurig, J. J. Mock, B. J. Justice, S. A. Cummer, J. B. Pendry, A. F. Starr, and D. R. Smith, Metamaterial electromagnetic cloak at microwave frequencies, *Science* **314**, 977 (2006).

[37] W. Cai, U. K. Chettiar, A. V. Kildishev, and V. M. Shalaev, Optical cloaking with Metamaterials, *Nat. Photonics* **1**, 224 (2007).

[38] I. Gil, J. Bonache, J. Garcia-Garcia, and F. Martín, Tunable metamaterial transmission lines based on varactor-loaded split-ring-resonators, *IEEE Trans. Microw. Theory Technol.* **54**, 2665 (2006).

[39] F. Martín, F. Falcone, J. Bonache, R. Marques, and M. Sorolla, Miniature coplanar waveguide stop band filters based on multiple tuned split ring resonators, *IEEE Microw. Wirel. Comp. Lett.* **13**, 511 (2003).

[40] I. Gil, J. Garcia-Garcia, J. Bonache, F. Martín, M. Sorolla, and R. Marques, Varactor-loaded split ring resonators for tunable notch filters at microwave frequencies, *Electron. Lett.* **40**, 1347 (2004).

[41] J. B. Khurgin, How to deal with the loss in plasmonics and metamaterials, *Nat. Nanotechnol.* **10**, 2 (2015).

[42] Y. Wu, C. Zhang, N. M. Estakhri, Y. Zhao, J. Kim, M. Zhang, X.-X. Liu, G. K. Pribil, A. Alù, C.-K. Shih, and L. Xiaoqin, Intrinsic optical properties and enhanced plasmonic response of epitaxial silver, *Adv. Mater.* **26**, 6106 (2014).

[43] S. Jahani and Z. Jacob, All-dielectric metamaterials, *Nat. Nanotechnol.* **11**, 23 (2016).

[44] A. J. Hoffman, L. Alekseyev, S. S. Howard, K. J. Franz, D. Wasserman, V. A. Podolskiy, E. E. Narimanov, D. L. Sivco, and C. Gmachl, Negative refraction in semiconductor metamaterials, *Nat. Mater.* **6**, 946 (2007).

[45] A. D. Boardman, V. V. Grimalsky, Y. S. Kivshar, S. V. Koshevaya, M. Lapine, N. M. Litchinitser, V. N. Malnev, M. Noginov, Y. G. Rapoport, and V. M. Shalaev, Active and tunable metamaterials, *Laser Photonics Rev.* **5**, 287 (2011).

[46] W. H. Hardy and L. A. Whitehead, Split-ring resonator for use in magnetic resonance from 20-2000 MHz, *Rev. Sci. Instrum.* **52**, 213 (1981).

[47] B. Sauviac, C. R. Simovski, and S. A. Tretyakov, Double split-ring resonators: Analytical modeling and numerical simulations, *Electromagn.* **24**, 317 (2004).

[48] K. Aydin, I. Bulu, K. Guven, M. Kafesaki, C. M. Soukoulis, and E. Ozbay, Investigation of magnetic resonances for different split-ring resonator parameters and designs, *New J. Phys.* **7**, 168–1 (2005).

[49] F. Falcone, T. Lopetegi, J. D. Baena, F. Martín, R. Marques, and M. Sorolla, Effective negative stopband microstrip lines based on complementary split ring resonators, *IEEE Microw. Wirel. Comp. Lett.* **14**, 280 (2004).

[50] J. D. Baena, J. Bonache, F. Martín, R. Marques, F. Falcone, T. Lopetegi, M. A. G. Laso, J. Garcia-Garcia, M. F. Portillo, and M. Sorolla, Equivalent-circuit models for split-ring resonators and complementary split-ring resonators coupled to planar transmission lines, *IEEE Trans. MTT* **53**, 1451 (2005).

[51] J. Martel, R. Marques, F. Falcone, J. D. Baena, F. Medina, F. Martín, and M. Sorolla, A new LC series element for compact bandpass filter design, *IEEE Microw. Wirel. Comp. Lett.* **14**, 210 (2004).

[52] J. D. Baena, R. Marques, F. Medina, and J. Martel, Artificial magnetic metamaterial design by using spiral resonators, *Phys. Rev. B* **69**, 014402–1 (2004).

[53] J. K. Gansel, M. Thiel, M. S. Rill, M. Decker, K. Bade, V. Saile, G. von Freymann, S. Linden, and M. Wegener, Gold helix photonic metamaterial as broadband circular polarizer, *Science* **325**, 1513 (2009).

[54] E. Shamonina, V. A. Kalinin, K. H. Ringhofer, and L. Solymar, Magneto-inductive waveguide, *Electron. Lett.* **38**, 371 (2002).

[55] O. Sydoruk, E. Tatartschuk, E. Shamonina, and L. Solymar, Analytical formulation for the resonant frequency of split rings, *J. Appl. Phys.* **105**, 014903–1 (2009).

[56] F. Hesmer, E. Tatartschuk, O. Zhuromskyy, A. Radkovskaya, M. Shamonin, T. Hao, C. Stevens, G. Faulkner, D. Edwards, and E. Shamonina, Coupling mechanisms for split ring resonators: Theory and experiment, *Phys. Stat. Sol. B* **244**, 1170 (2007).

[57] O. Sydoruk, A. Radkovskaya, O. Zhuromskyy, E. Shamonina, M. Shamonin, C. J. Stevens, D. J. Edwards, G. Faulkner, and L. Solymar, Tailoring the near-field guid-

ing properties of magnetic metamaterials with two resonant elements per unit cell, *Phys. Rev. B* **73**, 224406–1 (2006).

[58] E. Tatartschuk, N. Gneiding, F. Hesmer, A. Radkovskaya, and E. Shamonina, Mapping inter-element coupling in metamaterials: Scaling down to infrared, *J. Appl. Phys.* **111**, 094904–1–9 (2012).

[59] O. Zhuromskyy, E. Shamonina, and L. Solymar, Effect of radiation on dispersion of magneto-inductive waves in a metamaterial, *Proc. SPIE* **5955**, 595506–1 (2005).

[60] A. Radkovskaya, M. Shamonin, C. J. Stevens, G. Faulkner, D. J. Edwards, E. Shamonina, and L. Solymar, An experimental study of the properties of magnetoinductive waves in the presence of retardation, *J. Magn. Magn. Mat.* **300**, 29 (2006).

[61] N. Gneiding, O. Zhuromskyy, E. Shamonina, and U. Peschel, Circuit model optimization of a nano split ring resonator dimer antenna operating in infrared spectral range, *J. Appl. Phys.* **116**, 164311 (2014).

[62] S. Tretyakov, On geometrical scaling of split-ring and double-bar resonators at optical frequencies, *Metamaterials* **1**, 40 (2007).

[63] E. Shamonina, V. A. Kalinin, K. H. Ringhofer, and L. Solymar, Magnetoinductive waves in one, two, and three dimensions, *J. Appl. Phys.* **92**, 6252 (2002).

[64] M. C. K. Wiltshire, E. Shamonina, I. R. Young, and L. Solymar, Dispersion characteristics of magneto-inductive waves: comparison between theory and experiment, *Electron. Lett.* **39**, 215 (2003).

[65] M. C. K. Wiltshire, E. Shamonina, I. R. Young, and L. Solymar, Experimental and theoretical study of magneto-inductive waves supported by one-dimensional arrays of 'swiss rolls', *J. Appl. Phys.* **95**, 4488 (2004).

[66] H. Liu, D. A. Genov, D. M. Wu, Y. M. Liu, J. M. Steele, C. Sun, S. N. Zhu, and X. Zhang, Magnetic plasmon propagation along a chain of connected subwavelength resonators at infrared frequencies, *Phys. Rev. Lett.* **97**, 243902–1 (2006).

[67] G. Dolling, C. Enkrich, M. Wegener, C. M. Soukoulis, and S. Linden, Low-loss negative-index metamaterial at telecommunication wavelengths, *Opt. Lett.* **31**(12), 1800 (2006).

[68] E. Shamonina and L. Solymar, Magneto-inductive waves supported by metamaterial elements: components for a one-dimensional waveguide, *J. Phys. D: Appl. Phys.* **37**, 362 (2004).

[69] R. R. A. Syms, E. Shamonina, and L. Solymar, Magneto-inductive waveguide devices, *IEE Proc. Microw. Antennas Propag.* **153**, 111 (2006).

[70] R. R. A. Syms, E. Shamonina, and L. Solymar, Positive and negative refraction of magnetoinductive waves in two dimensions, *Eur. Phys. J. B* **46**, 301 (2005).

[71] R. R. A. Syms, E. Shamonina, V. Kalinin, and L. Solymar, A theory of metamaterials based on periodically loaded transmission lines: Interaction between magnetoinductive and electromagnetic waves, *J. Appl. Phys.* **97**, 064909–1 (2005).

[72] R. R. A. Syms, I. R. Young, and L. Solymar, Low-loss magnetoinductive waveguides, *J. Phys. D: Appl. Phys.* **39**, 1945 (2006).

[73] R. R. A. Syms, O. Sydoruk, E. Shamonina, and L. Solymar, Higher order interactions in Magnetoinductive waveguides, *Metamaterials* **1**, 44 (2007).

[74] R. R. A. Syms, L. Solymar, and E. Shamonina, Absorbing terminations for magneto-inductive waveguides, *IEE Proc. Microw. Antennas Propag.* **152**, 77 (2005).

[75] M. L. Brongersma, J. W. Hartman, and H. A. Atwater, Electromagnetic energy transfer and switching in nanoparticle chain arrays below the diffraction limit, *Phys. Rev. B* **62**, R16356 (2000).

[76] W. L. Barnes, A. Dereux, and T. W. Ebbesen, Surface plasmon subwavelength optics, *Nature* **424**, 824 (2003).

[77] L. Brillouin, *Wave Propagation in Periodic Structures*, Dover, New York, 1953.

[78] O. Sydoruk, O. Zhuromskyy, E. Shamonina, and L. Solymar, Phonon-like dispersion curves for magnetoinductive waves, *Appl. Phys. Lett.* **87**, 072501–1 (2005).

[79] A. Radkovskaya, O. Sydoruk, M. Shamonin, C. J. Stevens, G. Faulkner, D. J. Edwards, E. Shamonina, and L. Solymar, Experimental study of a bi-periodic magnetoinductive waveguide: Comparison with theory, *IET Microw. Antennas Propag.* **1**, 80 (2007).

[80] O. Sydoruk, M. Shamonin, A. Radkovskaya, O. Zhuromskyy, E. Shamonina, R. Trautner, C. J. Stevens, G. Faulkner, D. J. Edwards, and L. Solymar, Mechanism of subwavelength imaging with bilayered magnetic metamaterials: Theory and experiment, *J. Appl. Phys.* **101**, 073903–1 (2007).

[81] A. Radkovskaya, O. Sydoruk, E. Tatartschuk, N. Gneiding, C. Stevens, D. Edwards, and E. Shamonina, Dimer and polymer metamaterials with alternating electric and magnetic coupling, *Phys. Rev. B* **84**, 125121–1 (2011).

[82] J. E. Harvey, Fourier treatment of near-field scalar diffraction theory, *Am. J. Phys.* **47**, 974 (1979).

[83] G. B. J. de Boer, C. de Weerd, D. Thoenes, and H. W. J. Goossens, Laser diffraction spectrometry: Fraunhofer diffraction versus Mie scattering, *Part. Part. Syst. Charact.* **4**, 14 (1987).

[84] C. A. Balanis, *Antenna Theory: Analysis and Design*, Wiley, New York, 4th edition, 2016.

[85] W. R. Nitz, A. Oppelt, W. Renz, C. Manke, M. Lenhart, and J. Link, On the heating of linear conductive structures as guide wires and catheters in interventional MRI, *J. Magn. Reson. Imaging* **13**, 105 (2001).

[86] M. C. K. Wiltshire, J. B. Pendry, I. R. Young, J. Larkman, D. J. Gilderdale, and J. V. Hajnal, Microstructured magnetic materials for radio frequency operation in magnetic resonance imaging (MRI), *Science* **291**, 849 (2001).

[87] L. Solymar, O. Zhuromskyy, O. Sydoruk, E. Shamonina, I. R. Young, and R. R. A. Syms, Rotational resonance of magnetoinductive waves: Basic concept and application to nuclear magnetic resonance, *J. Appl. Phys.* **99**, 123908–1 (2006).

[88] M. J. Freire, R. Marques, and L. Jelinek, Experimental demonstration of a $\mu = -1$ metamaterial lens for magnetic resonance imaging, *Appl. Phys. Lett.* **93**, 231108 (2008).

[89] M. A. Lopez, M. J. Freire, J. M. Algarin, V. C. Behr, P. M. Jakob, and R. Marqués, Nonlinear split-ring metamaterial slabs for magnetic resonance imaging, *Appl. Phys. Lett.* **98**, 133508 (2011).

[90] R. Syms, L. Solymar, I. Young, and T. Floume, Thin-film magneto-inductive cables, *J. Phys. D: Appl. Phys.* **43**, 055102 (2010).

[91] R. R. A. Syms, T. Floume, I. R. Young, L. Solymar, and M. Rea, Flexible magnetoinductive ring MRI detector: Design for invariant nearest-neighbour coupling, *Metamaterials* **4**, 1 (2010).

[92] R. R. A. Syms, I. R. Young, M. M. Ahmad, S. D. Taylor-Robinson, and M. Rea, Magneto-inductive catheter receiver for magnetic resonance imaging, *IEEE. Trans. Biomed. Eng.* **60**, 2421 (2013).

[93] K. Segkhoonthod, R. R. A. Syms, and I. R. Young, Design of magneto-inductive magnetic resonance imaging catheters, *IEEE Sens. J.* **14**, 1505 (2014).

[94] R. Syms, I. Young, and M. Rea, Frequency scaling of catheter-based magneto-inductive MR imaging detectors, in *2013 Transducers & Eurosensors XXVII: The 17th International Conference on Solid-State Sensors, Actuators and Microsystems*, p. 594, IEEE, 2013.

[95] R. R. Syms, E. Kardoulaki, M. Rea, K. Choonee, S. Taylor-Robinson, C. Wadsworth, and I. R. Young, Magneto-inductive magnetic resonance imaging duodenoscope, *Prog. Electromagn. Res.* **159**, 125 (2017).

[96] J.-S. Bouillard, S. Vilain, W. Dickson, G. Wurtz, and A. Zayats, Broadband and broad-angle SPP antennas based on plasmonic crystals with linear chirp, *Sci. Rep.* **2**, 1 (2012).

[97] Y. Liu, S. Palomba, Y. Park, T. Zentgraf, X. Yin, and X. Zhang, Compact magnetic antennas for directional excitation of surface plasmons, *Nano Lett.* **12**, 4853 (2012).

[98] J. Lin, J. P. B. Mueller, Q. Wang, G. Yuan, N. Antoniou, X.-C. Yuan, and F. Capasso, Polarization-controlled tunable directional coupling of surface plasmon polaritons, *Science* **340**, 331 (2013).

[99] F. J. Rodríguez-Fortuño, G. Marino, P. Ginzburg, D. O'Connor, A. Martínez, G. A. Wurtz, and A. V. Zayats, Near-field interference for the unidirectional excitation of electromagnetic guided modes, *Science* **340**, 328 (2013).

[100] D. O'Connor, P. Ginzburg, F. J. Rodríguez-Fortuño, G. A. Wurtz, and A. V. Zayats, Spin-orbit coupling in surface plasmon scattering by nanostructures, *Nat. Commun.* **5**, 5327 (2014).

[101] M. F. Picardi, A. V. Zayats, and F. J. Rodríguez-Fortuño, Amplitude and phase control of guided modes excitation from a single dipole source: Engineering far- and near-field directionality, *Laser Photonics Rev.* **13**, 1900250 (2019).

[102] D. J. Bisharat and D. F. Sievenpiper, Guiding waves along an infinitesimal line between impedance surfaces, *Phys. Rev. Lett.* **119**, 106802 (2017).

[103] D. J. Bisharat and D. F. Sievenpiper, Electromagnetic-dual metasurfaces for topological states along a 1D interface, *Laser Photonics Rev.* **13**, 1900126 (2019).

[104] C. J. Stevens, C. W. T. Chan, K. Stamatis, and D. J. Edwards, Magnetic metamaterials as 1-D data transfer channels: An application for magneto-inductive waves, *IEEE Trans. Microw. Theory Tech.* **58**, 1248 (2010).

[105] C. W. T. Chan and C. J. Stevensy, Two-dimensional magneto-inductive wave data structures, in *Proceedings of the 5th European Conference on Antennas and Propagation (EuCAP)*, p. 1071, Rome, Italy, 2011.

[106] C. Stevens, Magnetoinductive waves and wireless power transfer, *IEEE Trans. Power Electron.* **30**, 6182 (2014).

[107] M. J. Freire, R. Marques, F. Medina, M. A. G. Laso, and F. Martín, Planar magnetoinductive wave transducers: Theory and applications, *Appl. Phys. Lett.* **85**, 4439 (2004).

[108] F. J. Herraiz-Martinez, F. Paredes, G. Zamora Gonzalez, F. Martin, and J. Bonache, Printed magnetoinductive-wave (MIW) delay lines for chipless RFID applications, *IEEE Trans. Antennas Propag.* **60**, 5075 (2012).

[109] J. Naqui, M. Durán-Sindreu, and F. Martín, Novel sensors based on the symmetry properties of split ring resonators (SRRs), *Sensors* **11**, 7545 (2011).

[110] J. Naqui, M. Durán-Sindreu, and F. Martín, Alignment and position sensors based on split ring resonators, *Sensors (Basel)* **12**, 11790–7 (2012).

[111] A. K. Horestani, J. Naqui, Z. Shaterian, D. Abbott, C. Fumeaux, and F. Martín, Two-dimensional alignment and displacement sensor based on movable broadside-coupled split ring resonators, *Sens. Actuators, A* **210**, 18 (2014).

[112] J. Naqui and F. Martín, Angular displacement and velocity sensors based on electric-LC (ELC) loaded microstrip lines, *IEEE Sens. J.l* **14**, 939 (2014).

[113] J. Naqui, J. Coromina, A. Karami-Horestani, C. Fumeaux, and F. Martín, Angular displacement and velocity sensors based on coplanar waveguides (CPWs) loaded with s-shaped split ring resonators (S-SRR), *Sensors* **15**, 9628 (2015).

[114] R. Melik, E. Unal, N. K. Perkgoz, C. Puttlitz, and H. V. Demir, Metamaterial-based wireless strain sensors, *Appl. Phys. Lett.* **95**, 011106 (2009).

[115] R. Melik, E. Unal, N. K. Perkgoz, C. Puttlitz, and H. V. Demir, Metamaterial based telemetric strain sensing in different materials, *Opt. Express* **18**, 5000 (2010).

[116] R. Melik, E. Unal, N. K. Perkgoz, B. Santoni, D. Kamstock, C. Puttlitz, and H. V. Demir, Nested metamaterials for wireless strain sensing, *IEEE J. Sel. Top. Quantum Electron.* **16**, 450 (2010).

[117] R. Melik, E. Unal, N. Kosku Perkgoz, C. Puttlitz, and H. V. Demir, Flexible metamaterials for wireless strain sensing, *Appl. Phys. Lett.* **95**, 181105 (2009).

[118] X. Huo and M. Ghovanloo, A wireless pharmaceutical compliance monitoring system based on magneto-inductive sensors, *IEEE Sens. J.* **7**, 1711 (2007).

[119] X. Huo, J. Wang, and M. Ghovanloo, A magneto-inductive sensor based wireless tongue-computer interface, *IIEEE Trans. Neural Syst. Rehabilitation Eng.* **16**, 497 (2008).

[120] W. Withayachumnankul, K. Jaruwongrungsee, A. Tuantranont, C. Fumeaux, and D. Abbott, Metamaterial-based microfluidic sensor for dielectric characterization, *Sens. Actuators A Phys.* **189**, 233 (2013).

[121] A. Ebrahimi, W. Withayachumnankul, S. Al-Sarawi, and D. Abbott, High-sensitivity metamaterial-inspired sensor for microfluidic dielectric characterization, *IEEE Sens. J.* **14**, 1345 (2014).

[122] P. Vélez, L. Su, K. Grenier, J. Mata-Contreras, D. Dubuc, and F. Martín, Microwave microfluidic sensor based on a microstrip splitter / combiner configuration and split ring resonators (SRRs) for dielectric characterization of liquids, *IEEE Sensors Journal* **17**, 6589 (2017).

[123] K. Shih, P. Pitchappa, M. Manjappa, C. P. Ho, R. Singh, and C. Lee, Microfluidic metamaterial sensor: Selective trapping and remote sensing of microparticles, *J. Appl. Phys.* **121**, 023102 (2017).

[124] T. Floume, Magneto-inductive conductivity sensor, *Metamaterials* **5**, 206 (2011).

[125] V. S. Ramalingam, M. Kanagasabai, and E. F. Sundarsingh, Detection of voids in fiber reinforced plastics using magnetoinductive coupled microstrip sensor, *IEEE Sensors Journal* **15**, 4182 (2015).

[126] J. Yan, C. J. Stevens, and E. Shamonina, A metamaterial position sensor based on magnetoinductive waves, *IEEE Open J. Antennas Propag.* **2**, 259 (2021).

[127] C. W. Oseen, Die Einsteinsche Nadelstichstrahlung und die Maxwellschen Gleichungen, *Ann. d. Phys.* **69**, 202 (1922).

[128] A. I. Uzkov, An approach to the problem of optimum directive antenna design, *Compt. Rend. Dokl. Acad. Sci. USSR* **53**, 35 (1946).

[129] A. Bloch, R. G. Medhurst, and S. D. Pool, A new approach to the design of superdirective aerial arrays, *Proc. IEE* **100**, 303 (1953).

[130] M. Uzsoky and L. Solymar, Theory of superdirective linear arrays, *Acta Physica, Acad. Hung. Sci.* **6**, 185 (1956).

[131] L. J. Chu, Physical limitations of omni-directional antennas, *J. Appl. Phys.* **19**(12), 1163 (1948).

[132] R. F. Harrington, Effect of antenna size on gain, bandwidth, and efficiency, *J. Res. Nat. Bur. Stand* **64**, 1 (1960).

[133] D. M. Pozar, New results for minimum Q, maximum gain, and polarization properties of electrically small arbitrary antennas, in *Proc. 3rd European Conf. Antennas and Propagation (EuCAP)*, p. 1993, Berlin, Germany, 2009.

[134] L. Solymar, Maximum gain of a line source antenna if the distribution function is a finite Fourier series, *IRE Trans. Antennas Propag.* **6**, 215 (1958).

[135] C. T. Tai, The optimum directivity of uniformly spaced broadside array of dipoles, *IEEE Trans. Antennas Propag.* **12**, 447 (1964).

[136] Y. T. Lo, S. W. Lee, and Q. H. Lee, Optimization of directivity and signal-to-noise ratio of an arbitrary antenna array, *Proc. IEEE* **54**, 1033 (1966).

[137] D. K. Cheng, Optimization techniques for antenna arrays, *Proc. IEEE* **59**, 1664 (1971).

[138] S. M. Sanzgiri and J. K. Butler, Constrained optimization of the performance indices of arbitrary array antennas, *IEEE Trans. Antennas Propag.* **19**, 493 (1971).

[139] D. R. Rhodes, On an optimum line source for maximum directivity, *IEEE Trans. Antennas Propag.* **19**, 485 (1971).

[140] J. M. Bacon and R. G. Medhurst, Superdirective aerial array containing only one fed element, *Proc. IEE* **116**, 365 (1969).

[141] E. H. Newman and M. R. Schrote, A wide-band electrically small superdirective array, *IEEE Trans. Antennas Propag.* **30**, 1172 (1982).

[142] E. E. Altshuler, T. H. O'Donnell, A. D. Yaghjian, and S. R. Best, A monopole superdirective array, *IEEE Trans. Antennas Propag.* **53**, 2653 (2005).

[143] A. D. Yaghjian, T. H. O'Donnell, E. E. Altshuler, and S. R. Best, Electrically small supergain end-fire arrays, *Radio Sci.* **43**, RS3002–1 (2008).

[144] S. Lim and H. Ling, Design of a closely spaced, folded Yagi antenna, *IEEE Antennas Wirel. Propag. Lett.* **5**, 302 (2006).

[145] A. Ludwig, C. D. Sarris, and G. V. Eleftheriades, Metascreen-based superdirective antenna in the optical frequency regime, *Phys. Rev. Lett.* **109**, 223901–1 (2012).

[146] K. Buell, H. Mosallaei, and K. Sarabandi, Metamaterial insulator enabled superdirective array, *IEEE Trans. Antennas Propag.* **55**, 1074 (2007).

[147] B. A. Panchenko, Metamaterials and superdirectivity of antennas, *J. Commun. Technol. Electron.* **54**, 286 (2009).

[148] T. Kokkinos and A. P. Feresidis, Electrically small superdirective endfire arrays of metamaterial-inspired low-profile monopoles, *IEEE Antennas Wirel. Propag. Lett.* **11**, 568 (2012).

[149] E. Shamonina and L. Solymar, Superdirectivity by virtue of coupling between meta-atoms, in *IEEE Proc. 7th Int. Congress on Advanced Electromagnetic Materials in Microwaves and Optics (Metamaterials 2013)*, p. 97, Bordeaux, France, 2013.

[150] E. Shamonina and L. Solymar, Superdirective 'meta-molecules', in *IEEE Proc. 8th Int. Congress on Advanced Electromagnetic Materials in Microwaves and Optics (Metamaterials 2014)*, p. 268, Copenhagen, Denmark, 2014.

[151] A. Radkovskaya, A. Vallecchi, L. Li, G. Faulkner, C. Stevens, and E. Shamonina, Experimental demonstration of superdirectivity for coupled dimers of meta-atoms, in *IEEE Proc. 10th Int. Congress Advanced Electromagnetic Materials in Microwaves and Optics (Metamaterials 2016)*, p. 328, Crete, Greece, 2016.

[152] A. Radkovskaya, S. Kiriushechkina, A. Vakulenko, P. Petrov, L. Solymar, L. Li, A. Vallecchi, C. J. Stevens, and E. Shamonina, Superdirectivity from arrays of strongly coupled meta-atoms, *J. Appl. Phys.* **124**, 104901–1 (2018).

[153] R. J. Mailloux, *Phased Array Antenna Handbook*, Artech House Publishers, Norwood, MA, 3rd edition, 2017.

[154] D. Margetis, G. Fikioris, J. M. Myers, and T. T. Wu, Highly directive current distributions: General theory, *Phys. Rev. E* **58**, 2531 (1998).

[155] R. C. Hansen, *Electrically Small Superdirective and Superconducting Antennas*, Wiley, New York, 2006.

[156] E. Shamonina and L. Solymar, Maximum directivity of arbitrary dipole arrays, *IET Microw. Antennas Propag.* **9**, 101 (2014).

[157] J. Yan, A. Radkovskaya, L. Solymar, C. J. Stevens, and E. Shamonina, Switchable unidirectional magnetoinductive waveguide, *IEEE Open J. Antennas Propag.* (Submitted, 2022).

[158] R. R. A. Syms, L. Solymar, and I. R. Young, Broadband coupling transducers for magneto-inductive cables, *J. Phys. D: Appl. Phys.* **43**, 285003 (2010).

[159] D. V. Redmayne, *Capacitive touch sensor*, US5650597A, U. S. Patent, July 1997.

[160] S. Kim, W. Choi, W. Rim, Y. Chun, H. Shim, H. Kwon, J. Kim, I. Kee, S. Kim, S. Lee, and J. Park, A highly sensitive capacitive touch sensor integrated on a thin-film-encapsulated active-matrix OLED for ultrathin displays, *IEEE Trans. Electron Devices* **58**, 3609 (2011).

[161] M. Schueler, C. Mandel, M. Puentes, and R. Jakoby, Metamaterial inspired microwave sensors, *IEEE Microw. Mag.* **13**, 57 (2012).

[162] M. Kang, J. Kim, B. Jang, Y. Chae, J.-H. Kim, and J.-H. Ahn, Graphene-based three-dimensional capacitive touch sensor for wearable electronics, *ACS Nano* **11**, 7950 (2017).

[163] H.-K. Kim, S. Lee, and K.-S. Yun, Capacitive tactile sensor array for touch screen application, *Sens. Actuator A Phys.* **165**, 2 (2011).

[164] G. Barrett and R. Omote, Projected-capacitive touch technology, *J. Soc. Inf. Disp.* **26**, 16 (2010).

[165] C. Stevens, J. Yan, and E. Shamonina, A metamaterial position sensor based on magneto-inductive waves, in *IEEE Proc. 13th Int. Congr. Artif. Mater. Nov. Wave Phenom. (Metamaterials 2019)*, pp. X–402, Rome, Italy, 2019.

[166] T. Hao, C. J. Stevens, and D. J.Edwards, Optimisation of metamaterials by Q factor, *Electron. Lett.* **41**, 653–654 (2005).

[167] J. Yan, A. Radkovskaya, A. Vallecchi, C. J. Stevens, and E. Shamonina, Demonstration of superdirectivity for PCB split ring dimers, in *12th European Conference on Antennas and Propagation (EuCAP 2018)*, London, UK, 2018.

[168] D. Dhayaa, A. Radkovskaya, J. Yan, G. Dima, E. O'Hara, L. Solymar, and E. Shamonina, Metamaterials for sensing conductive objects using time-domain reflectometry of magnetoinductive waves, in *IEEE Proc. 16th Int. Congr. Artif. Mater. Nov. Wave Phenom. (Metamaterials 2022)*, (Submitted) Siena, Italy, 2022.

[169] R. Syms and L. Solymar, Bends in magneto-inductive waveguides, *Metamaterials* **4**, 161 (2010).

[170] R. Syms, T. Floume, I. Young, L. Solymar, and M. Rea, Flexible magnetoinductive ring MRI detector: Design for invariant nearest-neighbour coupling, *Metamaterials* **4**, 1 (2010).